KAUNAS UNIVERSITY OF TECHNOLOGY

AUDRIUS JANKAUSKAS

ULTRASONIC METHOD FOR MEASURING DEFECT PARAMETERS IN A STORAGE TANK FLOOR

Doctoral Dissertation
Technological Sciences, Measurement Engineering (10T)

2017, Kaunas

The dissertation was completed during the period of 2011–2017 at Kaunas University of Technology, Prof. K. Baršauskas' Ultrasound Research Institute.

Scientific supervisor:

Prof. Dr. Liudas MAŽEIKA (Kaunas University of Technology, Technological Sciences, Measurement Engineering, 10T)

The doctoral dissertation has been published in:
http://ktu.edu

Editor:
Dovilė Dumbrauskaitė (Publishing House "Technologija")

ISBN 978-609-02-1365-0

The bibliographic information about the publication is available in the National Bibliographic Data Bank (NBDB) of the Martynas Mažvydas National Library of Lithuania

KAUNO TECHNOLOGIJOS UNIVERSITETAS

AUDRIUS JANKAUSKAS

ULTRAGARSINIS METODAS TALPYKLOS DUGNO DEFEKTŲ PARAMETRAMS MATUOTI

Daktaro disertacija
Technologijos mokslai, Matavimų inžinerija (10T)

2017, Kaunas

Disertacija rengta 2011–2017 metais Kauno technologijos universiteto Prof. K. Baršausko ultragarso mokslo institute.

Mokslinis vadovas:

Prof. dr. Liudas MAŽEIKA (Kauno technologijos universitetas, Technologijos mokslai, Matavimų inžinerija, 10T)

Interneto svetaines kurioje skelbiama disertacija, adresas:
http://ktu.edu

Redagavo:

Dovilė Dumbrauskaitė (leidykla „Technologija“)

ISBN 978-609-02-1365-0

Leidinio bibliografinė informacija pateikiama Lietuvos nacionalinės Martyno Mažvydo bibliotekos Nacionalinės bibliografijos duomenų banke (NBDB)

CONTENTS

LIST OF ABBREVIATIONS

AET	acoustic emission testing
ART	algebraic reconstruction technique
AST	aboveground storage tank
ECT	eddy current testing
FBP	filtered back-projection
FE	finite element
FT	Fourier transform
GW	guided waves
ICA	independent component analysis
MIC	microbiologically influenced corrosion
MFL	magnetic flux leakage
NDT	non-destructive testing
NDT&E	non-destructive testing and evaluation
PCA	principal component analysis
PECT	pulsed eddy current testing
PIGs	pipeline inspection gauges
PRA	probabilistic reconstruction algorithm
RAPID	reconstruction algorithm for the probabilistic inspection of damage
RFECT	remote field eddy current testing
SDC	signal difference coefficient
SAFE	semi-analytical finite element
SHM	structural health monitoring
SIRT	simultaneous iterative reconstruction technique
TDOA	time difference of arrival
UGW	ultrasonic guided waves
UT	ultrasonic testing
UTC	U-type component

INTRODUCTION

Relevance of research and scientific problem

Detecting and quantifying corrosion-type damage is vital for the petrochemical industry. To ensure a high level of safety and reliability, the storage tank and its floor should be periodically maintained in order to avoid corrosion-related accidents when hazardous chemical materials might get into the environment and groundwater. Various non-destructive testing and evaluation (NDT&E) methods are available for the inspection of the construction elements in the petrochemical industry, such as penetrant testing [1], magnetic [1–4], eddy current [1, 5, 6], thermography [7, 8], radiographic testing [9], acoustic emission [10–12] and ultrasonic techniques [1, 13, 14] which help to avoid chemical spill accidents. The main problem related to the inspection of the construction elements in the petrochemical industry, namely, storage tanks and their floors, using conventional NDT methods is that, in most cases, the storage tank has to be emptied, cleaned and made safe for human entry before any inspection could be performed. Moreover, such operations are costly and time-consuming. To overcome these disadvantages, an acoustic emission testing of flat-bottomed storage tanks is used as a beneficial method for tank operators to obtain information about possible corrosion, or even leakage of stored products, and about the floor without emptying the tank. However, the acoustic emission method used for storage tank inspection suffers from background noise and sometimes is impractical [10–12, 15,16]. Therefore, a new and more efficient NDT method for the inspection of storage tank floor, defect localisation and parameter measurement without emptying the tank needs to be developed.

The most promising technique which enables inspection at relatively long distances (up to 100 m) is the ultrasonic inspection method, based on the use of guided waves (GW). Differently from conventional ultrasonic NDT methods, there is no need to scan the whole object locally while applying ultrasonic guided waves (UGW) unlike using traditional thickness gauging methods, which only measure directly beneath the probe and are laborious when large areas need to be scanned. By using GW, it is enough to attach the ultrasonic transducers in an easily accessible place for an object segment to be monitored, as it was successfully demonstrated in the long-range applications for rapid screening of pipes [17–20], rails [21, 22], transmission lines and steel strands [23, 24] for the detection of corrosion and other structural defects. These objects are typically tested in the pulse-echo mode; the transducer transmitting the GW along the structure and returning echoes indicating the presence of defects or other structural features in the 1D plane. In this regard, the defects in the tank floor need to be observed and evaluated in the 2D plane. An application of UGW for the inspection of storage tank floor in the 2D plane and an investigation of interaction between these waves with their construction features was demonstrated [25–29]. However, the results of pilot investigations demonstrated only spatial distribution of attenuation in the tank floor without giving absolute values of the attenuation which could be related to the level of corrosion. Based on the results, it can be said that by applying the UGW inspection method, the object can be continuously monitored and defects can be detected, observing their size and location

in the object, whereupon the information can be given about the construction stability and further exploitation.

By using UGW, the storage tank floor could be inspected from the outer perimeter of the tank which, together with tomographic reconstruction algorithms, enables to reconstruct a spatial view of the tank floor with the distribution of defects inside of it. The main benefits of these waves are that UGW can propagate quite long distances with significant low losses, low sensitivity to object curvature, a large number of modes, allowing to choose the most appropriate, etc. But the use of the UGW is complicated because of dispersion, mode conversion at plate overlap and object non-uniformities, energy leakage to the surrounding medium [30–32]. Measurements are also complicated due to multiple joints, such as shell-to-bottom (T-joint) and lap joint connections, and a excessive amount of weld seams inside storage tank floor, which directly affects the transmission efficiency of GW and propagation distance. As a result, at the moment it is particularly important to develop and investigate an ultrasonic measurement method, which will enable to detect and measure defects inside of the storage tank floor from an outer perimeter without emptying and cleaning of it.

Scientific-technological problem and working hypothesis

The scientific-technological problem that is solved in this work is as follows: how is it possible to assess the corrosion level of storage tank floors used in the petrochemical industry, accessing them only from the outside.

The work hypothesis follows from the formulation of the problem: the ultrasonic guided waves (UGW), in combination with tomographic reconstruction algorithms, should enable the assessment of the corrosion level accessing only from the outside of a storage tank.

The aim and tasks of the work

The aim of the present work is to develop and investigate a method of measurement that enables to detect and measure corrosion-caused defects inside of an aboveground storage tank floor without emptying and cleaning the storage tank. In order to achieve the aim, the following tasks were formulated:

1. To analyse the methods used for detecting defects and measuring their parameters inside of a storage tank.
2. To develop numerical models for the investigation of propagation of the UGW in the tank floor and its construction elements and to assess the expected losses, propagation distances, resolution, sensitivity and possible changes during exploitation.
3. To perform experimental verification of the developed models and investigation of the regularities observed by modelling.
4. To investigate the use of the UGW tomography technique and the development such technique which enables to detect damage in the storage tank floor and a selection of optimal parameters for tomographic reconstruction.

5. To perform theoretical and experimental verification of the proposed measurement method and to estimate the expected uncertainties.

Scientific novelty of the work

1. The regularities and parameters of the UGW in the case of their propagation through shell-to-bottom (T-joint) and lap joint connections used in the construction of storage tank floor.
2. The improved ultrasonic transmission tomography algorithm for the reconstruction of the true value of UGW attenuation spatial distribution using optimisation for each projection.
3. Spatial sensitivity and resolution of ultrasonic transmission tomography determined by modelling and experiments.

The practical applications of the work

The ultrasonic guided waves (UGW) transmission tomography method developed in the dissertation can be applied in the industry and designed to detect and characterise corrosion-type defects in the storage tank floor. UGW transmission tomography is one feasible approach for inspecting areas with restricted access by transmitting GW through the area and then processing the measured wave field into an attenuation map of the storage tank floor and other planar structures.

Research methodology

The tasks presented above were solved using analytical and numerical modelling studies that have been verified experimentally. Ultrasonic guided waves propagation analysis was carried out by applying mathematical expressions proposed in literature and in Prof. K. Baršauskas' Ultrasound Research Institute used numerical simulation methods and programs. The propagation modelling of ultrasonic guided waves has been carried out using the finite element method ANSYS and Abaqus software packages. The ANSYS and Abaqus simulation results were analysed using routines written in the MATLAB environment. The digital signal processing was carried out using the MATLAB software.

Measurements were carried out using a low-frequency ultrasonic measurement system "Ultralab" which was designed and manufactured in Prof. K. Baršauskas' Ultrasound Research Institute of Kaunas University of Technology. The ultrasonic transducers were also manufactured in Prof. K. Baršauskas' Ultrasound Research Institute. The test samples and a scaled down model of the storage tank and models of lap joint welded plates with scaling factor 1:8 made of stainless steel were developed and used to verify the modelling results. To verify the tomographic method for reconstructing ultrasonic guided waves spatial attenuation distribution, the measurements were performed on the specially developed 1 m diameter and 6 mm thickness circular stainless steel sample with artificial defects. The experimental research was performed by using the TecScan Systems Inc. TCIS-3000 11-axis large industrial scanner. The measurements were performed by using Panametrics-NDT

ultrasonic immersion V318-SU transducers. For the excitation and reception of the ultrasonic signals a UTPR-CC-50 pulser/receiver was used.

The measurement uncertainties have been evaluated according to the standard uncertainties estimation methodology.

Approbation of the results

During the research period, 2 scientific articles were published on the topic of dissertation in publications referred in the main list of the Institute of Scientific Information (ISI). The main results of the work were presented in 4 domestic and international scientific conferences held in Palanga, Lublin, Prague and Munich.

Results presented for the defence of thesis

1. The regularities of the symmetric S_0 UGW mode propagation through the shell-to-bottom (T-joint) and lap joint connections.
2. A modified algorithm of the ultrasonic transmission tomography that enables to obtain true values of attenuation of UGW and their spatial distribution.
3. A model of the storage tank floor for the verification of the tomographic reconstruction algorithm.
4. The experimental measurement results, resolution and sensitivity of estimated spatial attenuation distribution in the specially developed stainless steel sample with artificial defects.
5. The experimental measurement results of spatial attenuation distribution in a scaled-down storage tank mock-up floor, using the proposed ultrasonic transmission tomography algorithm with a limited number of projections.

Structure and content of the dissertation

The present doctoral dissertation consists of an introduction, five chapters of the main body, conclusions and a list of references. The dissertation contains 142 pages featuring 107 illustrations, 10 tables and 108 mathematical expressions. The list of references covers 178 items.

The introduction of the dissertation describes the relevance of the problem, the objective and tasks of the thesis, its scientific novelty and the scope of the practical application of the work, its research methodology and approbation of results.

In the first chapter, a review of the most common non-destructive testing (NDT) and measurement methods used for defect detection in the aboveground storage tanks (AST) and their floor are presented. The advantages and disadvantages of the presented measurement methods are discussed. Recent advances of the ultrasonic guided waves (UGW) inspection method for long range application, corrosion-related damage detection and tomographic reconstruction algorithms are analysed.

The second chapter of the dissertation is dedicated to the numerical investigation of the UGW propagation in the scaled-down storage tank and transmission through its construction elements, such as shell-to-bottom (T-joint) and lap joint connections, by applying finite element (FE) analysis method. The symmetric S_0 UGW mode propagation through the shell-to-bottom and lap joint connections in the welded plates

and their influence on S_0 wave mode transmission losses in the storage tank were analysed. The modelling results were presented.

The third chapter of the dissertation covers the experimental investigation of the symmetric S_0 UGW mode propagation through the lap joint welded plates and verification of the modelling results presented in Section 2. The transmission losses of the symmetric S_0 mode transmitted through the lap joint connection have been estimated and the measurement results are presented.

The fourth chapter of the dissertation is dedicated to the proposed improved transmission tomography reconstruction algorithm for the reconstruction of true values of attenuation. A numerical model of a storage tank floor for the verification and investigation of the performance of the tomographic reconstruction algorithm is presented.

The fifth chapter of the dissertation presents the experimental investigation results on the UGW propagation in the specially developed 1 m diameter and 6 mm thickness stainless steel circular sample with artificial defects and in the storage tank mock-up scaled-down by 1:8 factor. The reconstructed spatial distribution of the artificial defects and the view of the UGW attenuation distribution in a tank floor reconstructed by using the proposed improved tomographic reconstruction algorithm are presented.

At the end of each chapter, the conclusions are presented.

Each chapter of the dissertation ends with conclusions and the general conclusions of the theoretical and experimental investigations, the list of references and the list of publications on the topic of the dissertation are presented at the end of the dissertation.

1. ANALYSIS OF THE MEASUREMENT METHODS USED FOR DETECTING DEFECTS IN AN ABOVEGROUND STORAGE TANK

In the petrochemical industry, general and pitting corrosion are the main corrosion phenomena on the internal and external surfaces of the aboveground storage tanks (AST) which affect their operation time. In general, the inner and outer surfaces of the tanks may be the subject of different corrosion types. In this case, the outer surface corrosion of the storage tank may occur due to contact with atmosphere and soil. Meanwhile, the corrosion of the inner surface is mainly caused by aqueous electrolyte solutions, sludge, microbiologically influenced corrosion (MIC) which intensity in an AST depends on: the crude oil and petroleum product type, the technology of AST exploitation, constructive features, condition of surfaces (the presence of rust, coatings), etc. [33]. However, the most crucial part of the AST is its floor because of the occurring outer (hidden) and inner corrosion and limited accessibility, which in long term of exploitation may lead to the leakage of petroleum or chemical products. A typical storage tank floor used for petrochemical products consists of a set of steel plates having a thickness of 6–8 mm joined together by using multiple lap joint welds and may have a diameter up to 100 m [27, 28]. Therefore, to provide a high level of safety and reliability, periodical maintenance of the tank and its floor should be performed within ascertained time periods, in order to prevent unplanned repair shutdowns. Such situations require a careful analysis of the corrosion state of the AST, which is typically performed by using non-destructive testing (NDT) methods which help to prevent or reduce the possibility of accidents and enables the detection and evaluation of irregularities in the object or its construction elements which could affect the period of safe operation. These methods are based on various physical phenomena and enable the detection of defects in non-transparent materials.

Therefore, the objective of the research presented in this chapter is the analysis and investigation of the NDT and measurement methods used or methods that can be applied for storage tank floor inspection, to detect corrosion-caused defects.

1.1 NDT methods used for the inspection of storage tanks

Non-destructive testing (NDT) is a wide group of analysis techniques used in industry for evaluating the properties of objects without causing damage. Since the tank floor is a plate-like object made from multiple welded carbon steel plates, the mainly measurement methods applicable for plate-like or metal structures, such as eddy current, magnetic, acoustic emission and ultrasonic methods, are commonly used for their inspection. All these inspection methods are based on physical phenomena (electromagnetic radiation or sound) taking place inside of a metal or its surface and they are discussed below.

The **eddy current testing** (ECT) methods are commonly used to detect flaws at the surface or subsurface of conductive materials because the eddy current strength decreases with depth due to the skin effect. To overcome this, several other measurement methods based on the eddy current inspection, such as pulsed eddy

current testing (PECT) [34, 35] and remote field eddy current testing (RFECT) [5, 36] methods are proposed for detecting corrosion-type defects.

Pulsed eddy current testing (PECT) method is a recently developed NDT&E method used for measuring the thickness of steel objects, such as pipes, vessels, and tanks, which uses a pulsed coil excitation for structural inspection. Differently from the conventional ECT method where a harmonic signal is used for excitation of the inducing coil, the PECT method uses pulsed excitation with a wide range of frequencies and is composed of a wide spectrum of frequency components. Moreover, the PECT method allows simultaneous inspection at different depths because the depth of penetration into a structure under investigation by eddy current is depended on the frequency of excitation [34, 35, 37–40]. Generally, the dependence of the penetration depth δ of eddy currents into test material is defined by expression 1.1.1 [40]:

$$\delta = \frac{1}{\sqrt{\pi f \mu \sigma}}, \tag{1.1.1}$$

where f is the frequency of the signal injected into the inducing coil, μ is the magnetic permeability and σ is the electrical conductivity.

By using the PECT method, the excitation coil is driven with a repetitive broadband pulse, usually a rectangular wave. However, for the PECT systems which use detection coils, the existing signal interpretations are reference-needed. To overcome it through loading of the variable duty cycle excitation and varied pulse width excitation techniques for a no reference-needed PECT method have been found. The operating principle of the varied pulse width excitation technique is presented in Fig. 1.1.1 [35, 41]. In this technique, the excitation is composed of a sequence of rectangular pulses PW_{Init}, whose widths gradually increase with constant pulse width increment PW_{Incre}, and space time P_{Spac} between the neighbouring pulses.

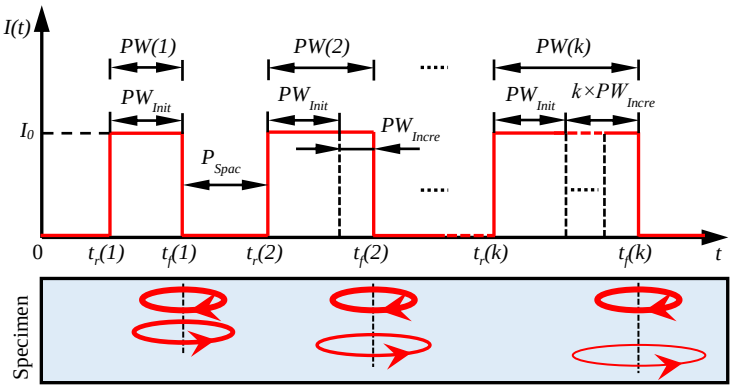

Fig. 1.1.1. Variable pulse width excitation and induced eddy currents [35, 41]

Generally, the peak time (rising and zero-crossing times) which is related to the depth of the defect, and peak value corresponding to the size of the defect, are the main features used in the PECT method [34, 38, 39]. However, the PECT method

suffers from noise and is not sufficient to extract more information about the defect. To overcome this disadvantage, advanced signal processing techniques, such as principal component analysis (PCA) and independent component analysis (ICA) are involved to interpret eddy current sensor response and to classify defects by feature extraction [38, 40, 42]. Moreover, the PECT method only allows inspecting the defects of the storage tank floor from the inside of the tank.

Remote field eddy current testing (RFECT) is an electromagnetic NDT method widely used in aviation and industrial applications for detecting corrosion and losses of wall thickness in the ferrous heat exchanger and boiler tubes [36, 43, 44]. Furthermore, several other studies on the use of the RFECT method for the detection of the back-side local corrosion in the flat bottom plates of an oil storage tank constructed of the ferromagnetic material were proposed [5, 6, 45].

According to the standard application of the RFECT method, the probe consisting of exciter and detector coils at a certain distance between each other is passed through the inspected object. The exciter coil is fed with a low frequency (10 Hz–1 kHz) alternating current and causes an electromagnetic field around it, which spreads out in the axial direction and as well into the wall and generates a secondary field which is much weaker than the primary field directly at the exciter coil. As it was obtained on the inspection of tubes, the direction of the energy flow is from inside to outside, and the area is called *near field*. The slope of an electromagnetic field in the *near field* in the axial direction is very fast because it has to provide the energy for the induction of eddy currents into the wall, while the slope of the secondary field at the outside is much smaller. Thus, at a certain axial distance from the exciter coil, there is an area at which the secondary field is stronger than the primary field which is called *remote field*. If a detector coil is placed in this area between the *near field* and the *remote field*, where the direction of energy flow is reverted, an electromagnetic field induced by energy which passed the wall thickness two times will be measured. On the direct coupling path, the energy comes directly from the exciter coil; however, on the indirect coupling path, the energy has passed to outside of the object and is transmitted back to the inside. If a defect is located in the wall on the indirect coupling path, it can be detected due to a change of the electromagnetic field in the *remote field* [36, 43, 44].

Meanwhile, to detect the flaws in flat plate structures used for the construction of the storage tank floor by the means of the RFECT method, the most important step is to make the indirect *remote field* penetrate the plate twice. To achieve the remote field eddy current effect in the flat plate, shielding unit is used in an RFEC probe to block the direct coupling field above the plate. As it was demonstrated on the applications of flat plates for detecting back-side local corrosion in the 6 mm thick bottom plates of an oil storage tank constructed of ferromagnetic material, it is possible to use the U-type component (UTC) made of the same material as the plates in the RFEC probe [5, 6, 45]. A schematic diagram of the RFEC probe with the U-type component is presented in Fig. 1.1.2 [5, 6, 45]. Eddy currents induced on the UTC and ferromagnetic plates attenuate the direct coupling field, therefore, the RFEC phenomenon occurs for detection of defects in ferromagnetic plates.

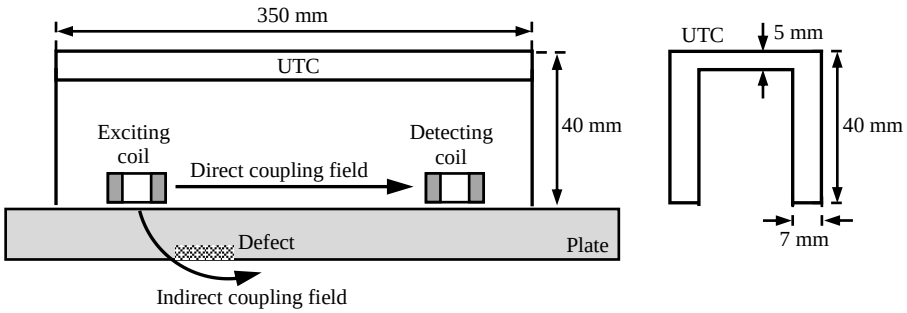

Fig. 1.1.2. A schematic diagram of the RFEC probe with a UTC for generating a remote field for detecting back-side flaws [5, 6, 45]

The main advantage of this inspection method is its high sensitivity to large wall thickness reduction (>50%) without sharp edges. Also, the RFECT method is not restricted by the skin effect. However, its main drawback is that this inspection method cannot differentiate whether the wall thinning is caused by internal or external defects and the storage tank floor can only be inspected from the inside. This requires emptying and cleaning the tank before the inspection. Moreover, it is essential to scan the entire floor of the storage tank to detect defects. A relatively high power consumption and the long probe length are also considered as drawbacks of the RFECT method [45, 46].

Magnetic flux leakage (MFL) testing is one of the most commonly used methods for the NDT&E of the ferromagnetic structures, such as steel pipes, aboveground storage tanks, such as those for oil and chemicals, rail tracks, ropes, etc. [2–4, 47–51]. In general, the MFL testing method uses a strong magnetisation system to yield a measurable magnetic flux leakage from the specimen. The magnetisation of the object in MFL systems is typically performed by using permanent magnets, successfully implemented in the pipeline inspection gauges (PIGs) for pipeline inspection. However, they are not always preferred, as magnetisation cannot be turned off when desired. To overcome this problem, electromagnets and electric currents are used to magnetise the object. The strength of the applied magnetic field is usually the saturation region of the magnetisation curve (B-H curve) of the ferromagnetic material, so that the reduction of material thickness will cause a large flux to leak [49, 51]. Ideally, the magnetisation system in a magnetic flux inspection system should produce a magnetic field of such characteristics:

- strong enough to cause a measurable magnetic field to leak from the test material at metal-loss regions;
- uniform from inside to outside surfaces of the inspected object thickness so that the measured signal is more linearly related to the depth of metal-loss;
- consistent in magnitude so that flux leakage measurements can be compared at different locations during an inspection run.

The magnetisation process is governed with equations 1.1.2 and 1.1.3 [51]:

$$M = \frac{\sum m_0}{V} = \chi_{\mathrm{m}} H \,, \tag{1.1.2}$$

$$B = \mu_0 H + \mu_0 M = \mu_0 (1 + \chi_m) H = \mu_0 \mu_r H = \mu H , \quad (1.1.3)$$

where M is magnetization intensity, H is the magnetic field intensity, B is the magnetic flux density, V is the volume of the magnetized specimen; $\sum m_0$ is the sum of the magnetic moments in a certain volume, χ_m is the magnetic susceptibility of a specimen; μ_0 is the permeability of air, μ_r is the relative magnetic permeability of materials with respect to air, μ is the absolute permeability of the medium.

There are two schemes for applying MFL testing to the inspection of defects in a storage tank floor. The usual method is used for detecting metal-loss defects in the so-called "near-side" of the materials, which could occur on the top of the tank floor due to the impurities of the stored product. The second method is used for detecting the "back-side" metal-loss defects of materials that might be caused by the environment and reaction with soil. However, in both cases the distribution of the magnetic flux leakage is strongly affected by the parameters of the defect (length, width, sharpness at the edges), thus making it difficult to differentiate between top and bottom defects [3, 47, 48]. It has been shown that internal flaws have a lower amplitude cross-section than external flaws. From that observation, the use of a separate sensor, such as eddy current sensors, which are less sensitive to internal corrosion was suggested to enable distinguishing between the top and bottom metal-loss [48].

The main advantage of the MFL testing method is that it allows a low-cost and efficient inspection with easy implementation. However, if a storage tank floor has not been magnetised to a sufficient extent, the defects cannot leak enough magnetic flux or it all can be flooded by noise. Moreover, the use of MFL testing method requires the inspected tank to be emptied and cleaned before the operator can perform the inspection. Since the area to be inspected is much bigger than the magnetizer, the tank floor can be inspected only locally and it is necessary to scan the floor.

Acoustic emission testing (AET) is a passive NDT method used in various industries, including the petrochemical industry. The application of AET to NDT&E allows a continuous monitoring and non-intrusive inspection for detecting active defects in storage tanks and pressure vessels. The AET method enables to overcome many shortcomings of the previously described PECT, RFEC and MFL inspection methods, because the tank does not need to be shutdown, emptied, and it does not require floor cleaning and scanning point by point [10–12, 15, 16, 52–55]. The main advantages of the AET method for the inspection of the storage tank are:

- high sensitivity;
- early and rapid detection of defects, flaws, cracks;
- cost reduction;
- minimised plant downtime, because there is no need to empty or clean the tank;
- inspects the whole tank floor;
- identifies tanks which need to be prioritised for inspection and repair;
- leaves good tanks on-line and saves on shut-down and cleaning time.

By using the AET method for inspection, the tested storage tank is typically 70% filled with product, which provides the required load pressure and generates an elasto-plastic strain in it. When a crack or another flaw grows, energy is released, and it propagates in the tested structure in the form of stress waves. The main characteristics of the AE signals used for damage detection and source identification are the signal amplitude, its duration, rise time, energy envelope and AE counts [55, 56]. Further evaluation of defects in the tank floor by using AET method is judged according to the distribution density of the AE events detected in the tank, which are usually localised by using *Time Difference of Arrival* (TDOA) measurements [52, 54]. The schematic diagram of the AE source location estimation in the 2D plane by using TDOA technique is presented in Fig. 1.1.3 [54]. By using TDOA measurements, each AE event is composed of more than 3 AE signals recorded by different AE sensors and generated by the same AE source. However, the TDOA measurements do not consider the situation when multiple AE sources generate signals simultaneously and might result in incorrect test results, because AE signals coming from different AE sources will be interpreted as one [52].

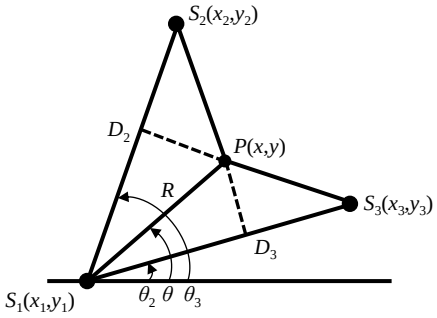

Fig. 1.1.3. A diagram of AE source location estimation by using the TDOA technique [54]

From figure presented, the distance and angle of the AE source from the sensor can be determined by solving the following 1.1.4 and 1.1.5 equations [54, 57]:

$$R = \frac{1}{2}\frac{D_2^2 - \Delta t_1^2 v^2}{\Delta t_1 v + D_2 \cos(\theta_2 - \theta)}, \tag{1.1.4}$$

$$R = \frac{1}{2}\frac{D_3^2 - \Delta t_2^2 v^2}{\Delta t_2 v + D_3 \cos(\theta - \theta_3)}, \tag{1.1.5}$$

where Δt_1 and Δt_2 are the time differences between sensors S_1–S_2 and S_1–S_3, respectively, v is the velocity in the material. Solving the set of these equations gives the location of the AE source in a polar form (R, θ).

The main advantage of the AET method is that it enables to perform the inspection and get the distribution of active defects in the 2D plane of a storage tank floor without emptying of it, by using sensors installed on the outside surface of the tank wall. However, the acoustic emission mainly occurs when the load is changed, thus some variation of the tank loading during the inspection is required. On the other

hand, acoustic emission is mainly expected by defects under development, so the passive defects can exist in the tank floor at the same time. Herewith, further analysis of the active defects should be carried out by using other NDT methods from the inside of the tank in order to get a more accurate estimation of defect parameters. Moreover, before formal AE inspection, background noise should be monitored to make sure it fulfils the requirements of the test. Therefore, it should be noted that AE tests on storage tanks should not be carried out in windy conditions or in the rain.

Ultrasonic testing (UT) is one of the most common and frequently used NDT methods for detecting and evaluating the defects and structure irregularities in objects or their construction elements. In most cases, the conventional ultrasonic NDT of the objects is performed by using bulk waves and scanning the whole object locally to determine the thickness of the object or any other defect parameters. However, in the case of AST inspection, it is related to extreme time-consumption since large areas of the tank should be inspected. Moreover, the tank should be emptied and cleaned for floor inspection in search of structural irregularities and made safe for human entry.

To overcome all these drawbacks of the conventional ultrasonic NDT, more advanced measurement techniques based on **ultrasonic guided waves** (UGW) are used. Guided waves are elastic perturbations propagating in a solid structure with free boundaries, for which displacements occur both in the direction of wave propagation and perpendicularly to the plane of the plate [58, 59]. In recent years, UGW inspection has been successfully used in NDT and structural health monitoring (SHM) applications for detecting defects and structural irregularities in the composite materials, plate-like structures and pipes since the possibility of rapid screening has been demonstrated for long lengths (up to 100 m), buried, coated, or in other ways inaccessible objects [13, 20, 60–65].

The main advantages of the UGW inspection which make the technique so attractive for NDT and SHM applications are [66–68]:

- the ability to inspect simultaneously a long segment of the object from a single transducer position;
- increased area coverage;
- no need for complicated and expensive insertion/rotation devices for scanning because the probe does not need to be moved during inspection;
- low sensitivity to object curvature and connecting joints;
- a large number of modes, allowing to choose the most appropriate;
- the ability to inspect under water, coatings, or insulation without significant loss of sensitivity;
- cost effectiveness of inspection.

At present, the UGW technology is used primarily to detect and locate discrete defects. These defects are detectable because they cause a reflection of the guided waves at an unexpected temporal location in the reflected waveform. However, the understanding of the reflection and scattering of UGW requires detailed knowledge of the interaction of the incident wave with different defect types. In this aspect, a significant amount of studies on the interaction of UGW with discontinuities in flat plates [69–72] and pipes [73–77] has been reported by a number of researchers. In most cases, the discontinuities, such as corrosion patches in the plates or pipes are

represented by relatively simple-shaped defects, such as flat-bottomed part thickness holes. Despite the fact that regular part thickness hole is not strictly representative of a corrosion patch, it is assumed that the nature of the UGW behaviour found in this study has generic applications to the behaviour in real cases. One challenge with the UGW inspection is that general corrosion which occurs over a large surface area may not reflect enough energy to be detected. In this regard, the primary effect on guided waves inspection when corrosion is present is an increase in the energy attenuation of guided waves. If the attenuation is measured, it may be possible to estimate the degree of corrosion through the inspected object [76]. Unfortunately, other mechanisms besides corrosion, such as additional coatings, liquid loadings, temperature, construction features, e.g. welds, bends and branches can increase the attenuation of guided waves and influence the achievable inspection range [30, 32, 65, 76]. In this case, the attenuation of the UGW propagating in the storage tank floor is conditioned by multiple welds and wave leakage losses into the surrounding medium. Thus, before the inspection technique can be developed to quantify corrosion of a tank floor using UGW, the attenuation caused by multiple welds used to connect separate plates in the construction of the tank floor must be investigated.

However, despite the ability of these waves to detect and locate the reduction of wall thickness, UGW are known to have a limited ability to accurately estimate the remaining thickness of the object. For this reason, the UGW are better known as a screening tool which allows to identify and localise the areas of a structure with possible defects which should be further inspected locally by other measurement methods [18, 19, 74, 78]. Moreover, it has been proposed that UGW tomography offers an opportunity to provide more accurate estimates of wall thickness by placing an array of transducers around the object at the fixed transducers position and improving monitoring sensitivity with a variety of mode choice and data analysis schemes [14, 68, 79–81]. Also, it allows to perform an inspection of the storage tank without emptying it from the outside perimeter of the tank and obtain the distribution of defects in the storage tank floor in a 2D plane. However, the use of the UGW and GW tomography in the NDT and SHM applications for damage detection is much more complicated due to the dependence of these waves on many parameters which are analysed in more detail in the following sections.

1.2 The characteristics and regularities of the ultrasonic guided waves propagation

Over the recent years, many new technologies have been developed with the potential for fast damage detection in the aerospace, civil and mechanical infrastructures. Lamb wave inspection is the most widely used damage detection technique based on the UGW, on which in the last few decades, a large amount of experimental research was published in a large number of publications related to the use of the UGW. However, the use of UGW is much more complicated in comparison to conventional UT due to the complex nature of these waves and their dependence on multiple parameters. Therefore, it is important to understand of the main parameters of UGW.

Lamb waves are guided waves in which elastic perturbations propagate in a solid plate with free boundaries, for which displacements occur both in the direction of wave propagation and perpendicularly to the plane of the plate [58, 59]. In an isotropic and homogeneous plate, as shown in Fig. 1.2.1, the waves, regardless of the mode, can generally be described in a form of *Cartesian* tensor by the following equation [82]:

$$\mu u_{i,jj} + (\lambda + \mu) u_{j,ji} + \rho f_i = \rho \ddot{u}_i, \quad (i, j = 1, 2, 3, \ldots), \tag{1.2.1}$$

where u_i and f_i are displacement and force in x_i direction, respectively, ρ is the density of the material, μ is the shear modulus, λ is the Lamé constant.

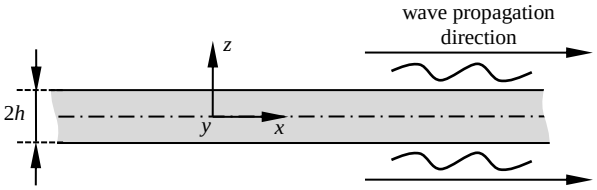

Fig. 1.2.1. Lamb wave propagation in a plate-like structure [58, 82]

There are two main types of ultrasonic Lamb wave propagating in a plate-like structure: symmetric modes, denoted as S_n and asymmetric modes, denoted as A_n. The motion of these symmetric and asymmetric Lamb wave modes are presented in Fig. 1.2.2 [58, 83].

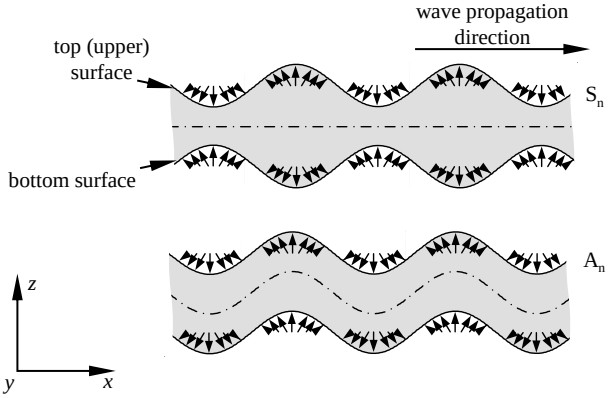

Fig. 1.2.2. Symmetric and asymmetric Lamb wave modes motion [58, 83]

By using *Helmholtz decomposition*, the 1.2.1 expression could be decomposed into two uncoupled parts, governing longitudinal and shear wave modes defined by the following equations [82, 84]:

$$\frac{\partial^2 \phi}{\partial x_1^2} + \frac{\partial^2 \phi}{\partial x_3^2} = \frac{1}{c_L^2} \frac{\partial^2 \phi}{\partial t^2}, \tag{1.2.2}$$

$$\frac{\partial^2\psi}{\partial x_1^2}+\frac{\partial^2\psi}{\partial x_3^2}=\frac{1}{c_S^2}\frac{\partial^2\psi}{\partial t^2}, \tag{1.2.3}$$

$$\phi=\left[A_1\sin(px_3)+A_2\cos(px_3)\right]e^{i(kx_1-\omega t)}, \tag{1.2.4}$$

$$\psi=\left[B_1\sin(qx_3)+B_2\cos(qx_3)\right]e^{i(kx_1-\omega t)}, \tag{1.2.5}$$

$$p^2=\frac{\omega^2}{c_L^2}-k^2,\ q^2=\frac{\omega^2}{c_S^2}-k^2,\ k=\frac{2\pi}{\lambda}=\frac{\omega}{c_{ph}}, \tag{1.2.6}$$

where c_L and c_S are longitudinal and shear wave velocities, respectively, c_{ph} is the phase velocity, x_1 – corresponds to the direction along the plate, x_3 – the direction perpendicular to the plate surface, A_1, A_2, B_1, and B_2 are constants which define boundary conditions, k is the wavenumber, λ is the wavelength and ω is the angular frequency.

Physical displacements of the plate can be expressed in terms of field variables according to the following expression [82, 84]:

$$u_1=\frac{\partial\phi}{\partial x_1}+\frac{\partial\psi}{\partial x_3},\ u_2=0,\ u_3=\frac{\partial\phi}{\partial x_3}-\frac{\partial\psi}{\partial x_1}. \tag{1.2.7}$$

The characteristic equation that describes the Lamb waves in isotropic, homogeneous plate can be written by following expression [82]

$$\frac{\tan(qh)}{\tan(ph)}=\frac{4k^2qp\mu}{\left(\lambda k^2+\lambda p^2+2\mu p^2\right)\left(k^2-q^2\right)}. \tag{1.2.8}$$

By using the expressions of longitudinal and shear wave velocities shown in 1.2.6, the characteristic equation can be decomposed into two parts which describe symmetric and asymmetric Lamb wave modes, defined with equations 1.2.9 and 1.2.10, respectively [82, 84]:

$$\frac{\tan(qh)}{\tan(ph)}+\frac{4k^2qp}{\left(k^2-q^2\right)^2}=0, \tag{1.2.9}$$

$$\frac{\tan(qh)}{\tan(ph)}+\frac{\left(k^2-q^2\right)^2}{4k^2qp}=0. \tag{1.2.10}$$

The phase c_{ph} and group c_{gr} velocity dispersion curves of the symmetric and asymmetric GW modes can be observed by using Rayleigh-Lamb equations (expressions 1.2.9 and 1.2.10). The following expressions relate angular frequency ω with wavenumber k and correspond to the frequency spectra or phase velocity c_{ph} with angular frequency ω and corresponds to the dispersion curves [85]. By taking into account the wavenumber k expression and phase velocity c_{ph}, the group velocity c_{gr} of the UGW could be calculated according to expression 1.2.11 [85]:

$$c_{\mathrm{gr}} = c_{\mathrm{ph}}^2 \left[c - \omega \frac{dc_{\mathrm{ph}}}{d\omega} \right]^{-1} = c_{\mathrm{ph}}^2 \left[c - \left(fd \frac{dc_{\mathrm{ph}}}{d(fd)} \right) \right]^{-1}, \quad (1.2.11)$$

where fd is the frequency times thickness. In this case, each Lamb wave mode has its own phase c_{ph} and group c_{gr} velocities depending on the frequency and plate thickness. The predicted phase c_{ph} and group c_{gr} velocity dispersion curves, calculated using the semi-analytical finite element (SAFE) method [86, 87], of the Lamb waves in an 8 mm thickness steel plate are presented in Fig. 1.2.3a and Fig. 1.2.3b, respectively.

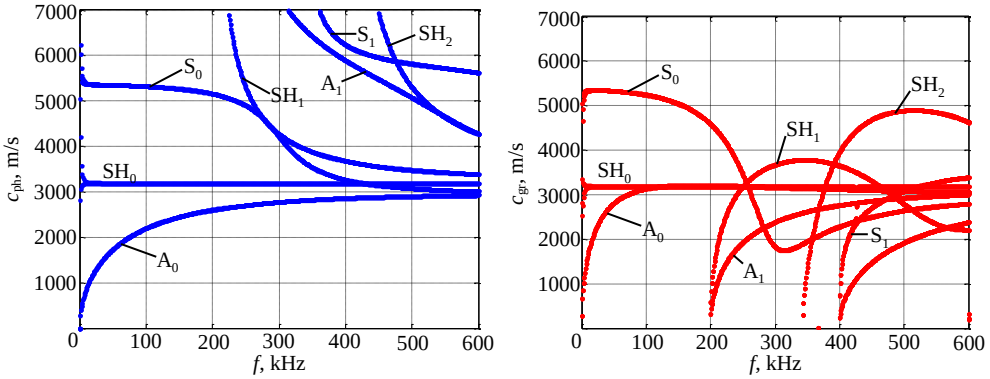

a) b)

Fig. 1.2.3. The predicted UGW phase c_{ph} (a) and group c_{gr} (b) velocity dispersion curves for 8 mm thickness steel plate

One of the principal difficulties when using UGW in various applications is their multi-modal nature. This means that even when the single incident GW mode is used for the inspection, the interaction of the wave with geometrical features of the structure under investigation or defect can result in a complicated multi-modal signal due to mode conversion. The multi-mode propagation of the UGW complicates the inspection and analysis of the measurement data because, in the worst case, different wave modes overlap in the signal, thus complicating the extraction of information of the single mode. Therefore, measurements usually are carried out using the fundamental asymmetric A_0 or/and symmetric S_0 guided waves modes. The most important parameters in selecting the operation frequency f_0 of the UGW are the phase c_{ph} and group c_{gr} velocities in the material which influence the spatial resolution and measurement sensitivity. In conventional ultrasonic measurements, the operation frequency f_0 or wavelength λ is the main parameter that influences the spatial resolution and sensitivity. On the other hand, other researchers have demonstrated that the dispersive guided waves could be used to detect and size the defect by measuring the relative amplitude of the modes generated by mode conversion at a defect. It was demonstrated that UGW may be used to find notches when the wavelength λ to defect depth ratio is of the order of 40, thus showing a higher sensitivity of the guided waves to some type of defects compared to the conventional bulk waves UT [88–90]. The correct selection of the operating frequency f_0 minimises the dispersive and multi-

mode propagation of the UGW. The dispersive propagation of the UGW distorts the signals in the time domain. Furthermore, it reduces the spatial resolution and the sensitivity of measurements and increases the risk of overlapping signals [31, 88, 91].

Other important parameters of the UGW used in the long-range inspection are the attenuation in the material and propagation losses. The attenuation in material directly influences the amplitude of UGW with increasing distance, while the propagation losses of the guided waves are most commonly caused by volume scattering. The UGW attenuation and propagation losses are directly affected by such factors as:

- signal distortion caused by wave dispersion;
- wave diffraction;
- wave mode transformation;
- material reduction;
- leakage of wave energy into the surrounding medium.

Direct influence on the UGW signal amplitude has a geometrical complexity of the structure which causes difficulties in the effective use of the GW because of the high level of scattering which leads to a complicated transmission, reflection, diffraction and mode conversion [92–95]. The propagation losses arising from the dispersion of the signal energy being dissipated not only in the wave propagation direction but also in other directions. To correct for radial fall-off of the waves energy, the signal measurements are typically normalised by $1/\sqrt{r}$ law, where r is the distance the wave has propagated [93]. Also, there is an acoustic wave energy transformation influenced by the material attenuation, when a part of the signal energy is converted into heat. However, this effect is more pronounced and more frequently observed in composite plates than in metallic constructions [96–98]. Another important factor influencing UGW attenuation is wave mode conversion caused by wave interaction with discontinuities/defects, as well as thickness reduction which leads to newly-converted modes and energy dissipation. Thus, the attenuation and propagation losses of the UGW are complex and can be influenced by many factors, such as roughness of the surface of the plate, plate material inhomogeneity and influence of the superimposed parts or components on the surface of the plate [32, 99, 100]. In the case of storage tank floor inspection, the propagation losses of the UGW are mainly caused by multiple lap welds, corrosion caused thickness reduction and wave energy leakage to the surrounding medium, thus complicating the inspection of storage tanks by the means of guided waves. At the same time, the dependence of UGW on many parameters creates the necessary preconditions for measurements and evaluation of the inspected structure integrity.

In this respect, the most essential are the UGW propagation losses due to the leakage of the wave energy into the surrounding medium. These leakage losses depend on the liquid boundary interaction between the object and the surrounding medium. In the ideal case, if the object is loaded with air, these leakage losses are very low because of the significantly different acoustic impedances between air and the test object and can be neglected. However, for the objects loaded with water, petrol or another acoustic environment, this phenomenon for some UGW modes may have

a significant effect and determine the main factors in choosing the most suitable operating GW mode. A steel plate submerged into water could be analysed as an example. To calculate the dispersion curves of the leakage losses, the commercially available "DISPERSE" software based on the global matrix model was applied [101]. The dispersion curves of leakage losses for an 8 mm thick steel plate loaded with water from one side are presented in Fig. 1.2.4.

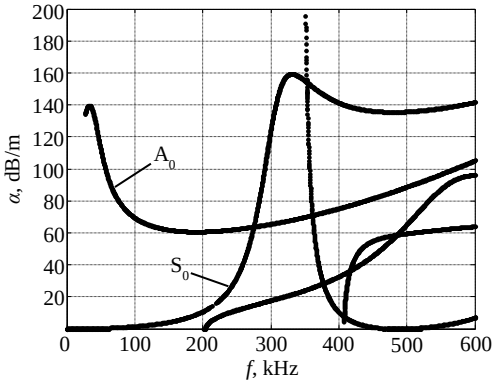

Fig. 1.2.4. Predicted dispersion curves of UGW leakage losses α for an 8 mm thick steel plate loaded with water

As the dispersion curves show, some wave modes have frequency bandwidths, where due to a large wave energy leakage to the surrounding medium, UGW modes are strongly attenuated and practically cannot propagate, thus complicating the use of UGW for the long-range inspection. As in the case of the most frequently used fundamental asymmetric A_0 and symmetric S_0 guided wave modes, it could be observed that the leakage losses for asymmetric A_0 wave mode in the frequency bandwidth from 30 kHz up to 200 kHz varies from 69.33 dB/m to 133.1 dB/m, as opposed to the symmetric S_0 mode which shows essentially lower leakage losses which vary from 0.12 dB/m to 10.88 dB/m. The main factor influencing the losses of guided waves is that in each mode the displacement and stress distribution changes with frequency and thickness. A general observation is that at low frequencies the out-of-plane u_y displacement component is dominant for the asymmetric A_0 guided wave mode and is almost constant through the thickness. However, when frequency increases, the out-of-plane u_y displacement component reduces compared to the in-plane u_x displacement component in relative amplitude. Meanwhile, for the symmetric S_0 wave mode, a general observation is that at low frequencies, the in-plane u_x displacement component is dominant and almost constant through the thickness. When the frequency value increases, the relative amplitude of the out-of-plane u_y displacement component increases, and u_x component gets more concentrated in the centre of the plate. Meanwhile, in the frequency bandwidth where leakage losses are lower, the out-of-plane u_y displacement component reduces, compared to the in-plane u_x component in the relative amplitude thus resulting in lower leakage losses to the surrounding medium. It is assumed that water or other liquids mainly have an impact

on the reduction of the out-of-plane u_y displacement component, while the in-plane u_x displacement component is affected only by liquids possessing high viscosity [102].

As the analysis of UGW characteristics indicates, the symmetric S_0 wave mode is the most suitable for inspecting the storage tank floors for several reasons. The symmetric S_0 wave mode has the highest propagation velocity and should pass the tank floor first, thus making it easier to separate from whole signals. Moreover, it is less dispersive in the frequency bandwidth where only fundamental guided wave modes exist. Furthermore, the symmetric S_0 wave mode contains lower leakage losses, ensuring longer propagation distance in fluid coupled structures.

1.3 Ultrasonic guided waves tomography

When UGW propagate in structures with corrosion defects, many phenomena, such as mode cut-off and conversion, velocity changes, mode frequency shifts, transmission and reflection amplitude ratio change can be observed and used to detect corrosion in the structures. Conventional UGW testing methods generally only evaluate change of the parameter of interest along the wave propagation path of either reflected or transmitted signal. As in the case of pipe inspection, it can be stated that the corrosion exists somewhere between the transmitter and the receiver. However, in the case of the storage tank floor inspection, the 2D distribution of the corrosion is preferred. The only technique which enables a 2D reconstruction of physical property distribution is tomography. Therefore, if UGW measurements are made for a number of transducer positions, then an image of the inspected region can be reconstructed by using tomographic reconstruction algorithms to give an easily interpretable spatial map of the parameter of interest [14, 79, 103–112].

In general, tomography reconstructs the distribution of some physical parameters in the cross section of the object from the so-called projections. The gathered UGW information is utilised according to the two main principal setups of tomography:

- *reflection tomography* – ultrasonic waves backscattered within the volume are processed using the complete signal for imaging;
- *transmission tomography* – attenuation or velocity of waves transmitted through the volume are processed using only the amplitude of the time-of-flight of the first arriving pulse for imaging.

Ultrasonic reflection tomography is more often used in the field where transmission tomography is not possible because of physical constraints of the object. The basic aim of reflection tomography is to reconstruct a cross-sectional image of the object from the reflection data. One major aspect of this form of imaging is that it is not necessary to encircle the whole object with transmitters and receivers for gathering the projection data because the transmission and reception are done from the same side of the object. However, ultrasonic reflection tomography fails when strong multiple scattering occurs, and large objects with respect to wavelength must be inspected [113, 114].

The most common approach of the UGW tomography is based on the use of transmission tomography, where the information could be gathered by using straight-

ray or diffraction tomography methods. The interaction of UGW with discontinuities affects the attenuation and velocity properties of the ultrasonic signals, thus the attenuation, speed variations, time-of-flight, frequency shift are among the main parameters used in tomographic reconstruction. However, the most common approach of UGW transmission tomography is based on the measurement of wave speed variations and converting it into thickness variations by using GW dispersion relations for wave speed as a function of the frequency-thickness product. The solution of this system yields a velocity map over the entire inspected region of the object which is converted into a thickness map used to detect corrosion or other types of defects [81, 106, 112-117].

According to the brief description of transmission tomography, it is assumed that in straight-ray ultrasonic tomography waves travel in straight directions without diffraction. A typical straight-ray parallel beam projection tomography set-up is presented in Fig. 1.3.1.

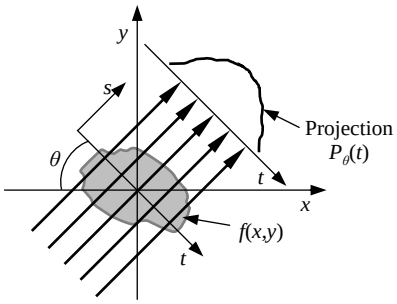

Fig. 1.3.1. Parallel beam projection for tomographic reconstruction

In straight-ray UGW tomography the projection data must correspond to the line integral of a given parameter and thus the ray theory must be valid [115, 118, 119]. The ray theory is valid when the characteristic size of a defect d is larger or comparable to the wavelength λ and the width of the first Fresnel zone L_F, which is defined with equations 1.3.1 and 1.3.2 [115, 118–120]:

$$d \gg \lambda\,,\ d \gg L_F\,, \tag{1.3.1}$$

$$L_F = \sqrt{L\lambda}\ , \tag{1.3.2}$$

where L is the length from the source to the receiver, λ is the wavelength.

When the sizes of defects or other heterogeneities in the object become comparable or smaller than the wavelength, it is not possible to use ray theory-based concepts, because of interference between the incident and scattered signals, and wave diffraction becomes dominant thus limiting the resolution of the straight-ray UGW tomography. If the propagation distance between the source and the receiver is reduced, the ray theory becomes valid but the required reduction is too large to be of practical use thus limiting the use of straight-ray tomography for long-range UGW inspection [115].

Since the guided Lamb wave cannot penetrate through strongly scattering defects, and the assumption of straight-ray tomography limited by the ray theory fails,

diffraction tomography is used as a way to incorporate scattering effects into tomographic reconstruction algorithms. The objective of the ultrasonic diffraction tomography is to reconstruct the spatial distribution of a target material property from the perturbation induced by the structure of the object on the free propagation of a wave field [116, 118, 121–123]. The processing of the scattered field in diffraction tomography is carried out in the spatial frequency domain. The mapping of the scattered field in the spatial frequency domain is presented in the Fig. 1.3.2 [116, 121].

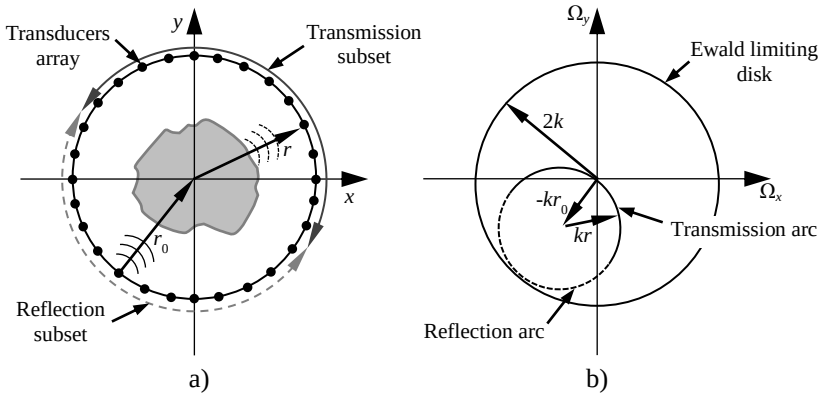

Fig. 1.3.2. A circular array that can illuminate an unknown object from all directions r_0 and detect the scattered field from any direction r (a), the two dimensional K space showing the mapping of the scattered field measured in direction r from an incident direction r_0 (b)

By using the configuration presented in Fig.1.3.2, the unknown object is illuminated from direction r_0 and the scattered field is detected in direction r. The scattered field measured in direction r maps into the K space at $k(r-r_0)$, where k is the wavenumber. As the position of the source rotates around the array, an Ewald limiting disk in the K space with a radius $2k$ is populated. For any source in the array, the sensors can be divided into transmission and reflection subsets. The scattered field measured with the transmission subset maps in the K space on the transmission arc and the reflection subset maps on the reflection arc. For any direction r_0, the transmission subset is contained within a circle of radius $\sqrt{2}k$ in the K space and the reflection subset is contained between $\sqrt{2}k$ and $2k$ (Fig.1.3.2). Therefore, the transmission subset contains the lower spatial frequencies and the reflection subset contains the higher spatial frequencies [116, 121].

To perform a diffraction tomography reconstruction, an approximation of the wave equation must be used to calculate the scattered field which is done by using the most common Born and Rytov approximation methods [116, 117, 124]. By using the Born approximation, the scattered field is obtained by subtracting the incident field from the total scattered field. It is considered that the field scattered by a defect is a superposition of the scattered field from many elemental scatterers and all these scatterers behave independently. However, as the wavelength passes through a scatterer, its phase becomes distorted, meaning that the elemental scatterers no longer behave independently. For the Born approximation, the phase difference between the incident field and wave propagating through the unknown object must be less than π.

Therefore, the Born approximation is only valid for small, low contrast (contrast being defined as the velocities difference between the background medium and the unknown object) or limited size defects, where the phase distortion is low. However, for many applications of the UGW tomography, it is important to detect and quantify large heterogeneities, such as corrosion depths which are up to 80% of the total wall thickness. This large thickness variation corresponds to a large velocity difference, thus causing the Born approximation to break. For this reason, the Born approximation is known to efficiently represent the perturbations caused only by weak scatterers [116, 118, 120, 124]. The Rytov approximation used for wave equation approximation focuses on the variations of phase and is more complex to implement because a complex algorithm needs to be evaluated. To use the Rytov approximation, the phase of the total and incident fields needs to be unwrapped. The change in the scattered phase over a wavelength is the most important parameter used for Rytov approximation. Moreover, Rytov approximation is valid when phase change over a single wavelength is small but it faces difficulties in its practical implementation [116, 120, 124].

In general, to take full advantage of the different properties of UGW, the transducers used in tomographic reconstruction applications should be broadband and excite any desired point on the dispersion curves. At the same time, a spatial sampling criterion must be kept because the quality of reconstruction depends on the density of rays passing through the object. According to this criterion, if the most common circular aperture is used for gathering the tomographic data, the minimum number N of transducers to correctly sample a wave field of wavelength can be expressed with equation 1.3.3 [125]:

$$N \geq \frac{2\pi r_0}{\lambda}\left(1+\frac{1}{\alpha_{N-1}}\right) \approx \frac{4\pi r_0}{\lambda}, \tag{1.3.3}$$

where r_0 is the radius of the circle which circumscribes the object; λ is the wavelength; $\alpha_n = \gamma_n / n$ where γ_n is the Bessel function maximum, n is the Bessel function order. Then the sampling interval between the transducers Δ deployed along the circular aperture of radius r could be defined according to expression 1.3.4

$$\Delta \leq \frac{\lambda r}{2r_0}. \tag{1.3.4}$$

Expression 1.3.4 shows that in the case of using the most common circular aperture, the sampling interval depends on the size of the defect to be imaged relative to the wavelength and on its position with respect to the aperture [125]. However, in the practical implementation of ultrasonic tomographic measurement method, it is impossible to measure a large number of projections thus a limitation of the quality of reconstruction occurs.

Since ultrasonic diffraction tomography is limited by the fail of Born and Rytov approximations for strongly scattering objects and difficulties in its practical implementation for the inspection of the storage tank floor, a straight-ray tomographic inspection method was selected as the most suitable. However, by using straight-ray

UGW tomography, only the defects that are bigger than the wavelength can be observed, thus a limitation of the resolution occurs.

1.4 Ultrasonic guided waves tomographic imaging algorithms

In UGW tomography, it is important to choose a practical tomographic reconstruction algorithm in order to get a good reconstructed tomographic image. The algorithms used in the tomographic reconstruction are divided into two main groups – filtered back-projection based algorithms and algebraic reconstruction algorithms.

The **filtered back-projection** (FBP) algorithm is a generally well-known algorithm for imaging the data collected by using tomographic inspection methods. FBP consists of three main steps: weighting, filtering and back-projection for image reconstruction. The key to FBP imaging is the Fourier slice theorem that relates the measured projection data to the two-dimensional Fourier transform of the cross-section of an object.

Parallel beam projection and *fan-beam* projection are two most common acquisition geometries used in filtered back-projection based tomography. By using the *parallel beam* acquisition geometry, the object is reconstructed from a set of line integrals taken at different angles around the object. In general, if a *parallel beam* acquisition scheme, presented in Fig. 1.4.1, is used for the reconstruction of an image $f(x,y)$, then its projection $P_\theta(t)$ at angle θ along line t could be defined according to equation 1.4.1 [103, 105]:

$$P_\theta(t) = \int_{-\infty}^{\infty} f(t,s)ds\,, \tag{1.4.1}$$

where (t,s) is the coordinate system at an angle θ to the (x,y) system.

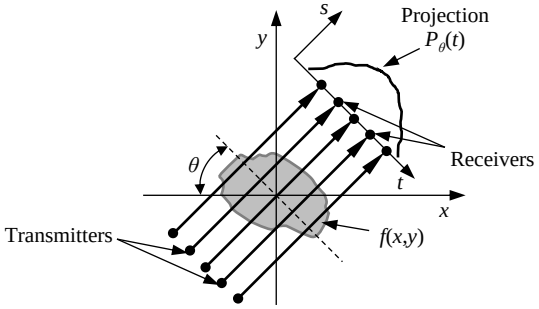

Fig. 1.4.1. Parallel beam projection for tomographic reconstruction

Then, the spatial Fourier transform of function $P_\theta(t)$ is defined according to equation 1.4.2 [103, 105]:

$$S_\theta(\omega) = \int_{-\infty}^{\infty} P_\theta(t)e^{-j2\pi\omega t}dt = \int_{-\infty}^{\infty}\int_{-\infty}^{\infty} f(x,y)e^{j2\pi\omega(x\cos\theta+y\sin\theta)}dxdy\,, \tag{1.4.2}$$

where the coordinate transform relation, presented with expression 1.4.3, has been applied [103]:

$$t = x\cos(\theta) + y\sin(\theta),\ \ s = -x\sin(\theta) + y\cos(\theta). \tag{1.4.3}$$

The object function $f(x,y)$ can be recovered by using the inverse transform and, taking into account the spatial frequency relation, can be defined according to equations 1.4.4 and 1.4.5 [103, 105]:

$$u = \omega\cos(\theta),\ \ v = \omega\sin(\theta), \tag{1.4.4}$$

$$f(x,y) = \int_{-\infty}^{\infty}\int_{-\infty}^{\infty} F(u,v)e^{j2\pi(ux+vy)}dudv. \tag{1.4.5}$$

If the Cartesian coordinate system for the frequency domain is changed to a polar coordinate system, equation 1.4.5 used for the reconstruction of the object function $f(x,y)$ can be written as [103, 105]:

$$f(x,y) = \int_{0}^{2\pi\omega}\int_{0} F(\omega,\theta)e^{j2\pi\omega(x\cos\theta + y\sin\theta)}\omega d\omega d\theta = \int_{0}^{\pi} Q_\theta(t)d\theta. \tag{1.4.6}$$

The filtered back-projection and the object function $f(x,y)$ in terms of (x,y) and projection angle θ could be defined according to equations 1.4.7 and 1.4.8 [103, 105]:

$$Q_\theta(t) = \int_{-\infty}^{\infty} F(\omega,\theta)e^{j2\pi\omega}|\omega|d\omega, \tag{1.4.7}$$

$$f(x,y) = \int_{0}^{\pi} Q_\theta(x\cos\theta + y\sin\theta)d\theta, \tag{1.4.8}$$

where $|\omega|$ is the filter response. However, in the tomographic reconstruction based on the use of the FBP method, the filtering of the projection results in the loss of true value of the measured parameter. Despite that, the spatial distribution is reconstructed correctly.

Differently from the parallel beam algorithm, by using the *fan-beam* acquisition geometry, the object is reconstructed from a set of line integrals spreading out from a single point which is rotated about the object. If a *fan-beam* scheme, presented in Fig. 1.4.2, is used for tomographic reconstruction of an image $f(x,y)$ then the filtered back-projection, in general, could be defined with equation 1.4.9 [126]:

$$f(x,y) = \int_{0}^{2\pi}\frac{1}{L^2}Q_\alpha(\gamma')d\alpha, \tag{1.4.9}$$

where L is the distance from the point P with coordinates (x,y) to the transmitter, $Q_\alpha(\gamma')$ is the filtered projection data along line $\gamma = \gamma'$ for the current projection,

γ – current receiver angle with respect to the central ray, γ' is the angle of the fan beam ray passing through the point *P*.

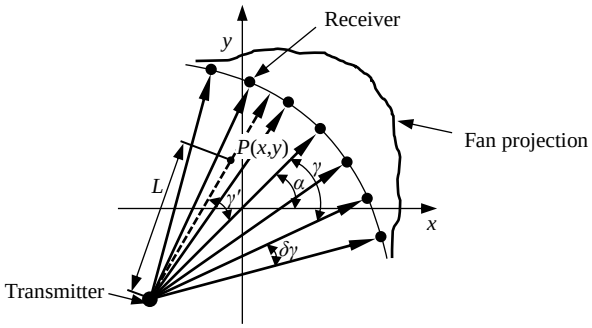

Fig. 1.4.2. Fan-beam projection with an evenly spaced circular transducer array

By using a *fan-beam* tomographic reconstruction scheme, it is assumed that each projection $R_\alpha(\gamma)$ has *N* data points sampled with a sampling interval $\delta\gamma$, where α is the projection angle. Then the modified projection data could be defined with equation 1.4.10 [126]:

$$R'_\alpha(n\cdot\delta\gamma)=R_\alpha(n\cdot\delta\gamma)\cdot R\cos(n\cdot\delta\gamma). \tag{1.4.10}$$

Convolving of each modified projection $R'_\alpha(n\cdot\delta\gamma)$ with the high-pass filter $g(\gamma)$ to get corresponding filtered projection $Q_\alpha(n\cdot\delta\gamma)$ is done by using equations 1.4.11 and 1.4.12 equations [14, 126]:

$$g(n\cdot\delta\gamma)=\begin{cases}\dfrac{1}{8(\delta\gamma)^2}, n=0\\ 0, n \text{ even}\\ -\dfrac{1}{2(\pi\sin(n\cdot\delta\gamma))^2}, n \text{ odd}\end{cases}, \tag{1.4.11}$$

$$Q_\alpha(n\cdot\delta\gamma)=R'_\alpha(n\cdot\delta\gamma)*g(n\cdot\delta\gamma). \tag{1.4.12}$$

Then weighted back-projection of each filtered projection along the fan is performed according to equation 1.4.13 [14, 126]:

$$f(x,y)\approx\frac{2\pi}{M}\sum_{i=1}^{M}\frac{Q_{\alpha_i}(n\cdot\delta\gamma')}{L^2(x,y,\alpha_i)}, \tag{1.4.13}$$

where *M* is the total number of projections, *L* is the distance from the transmitter to point $P(x,y)$, α_i is the i^{th} projection angle, γ' is the angle of the fan beam ray passing through point $P(x,y)$.

The main advantage of the FBP based reconstruction algorithms is that they are computationally fast, accurate and easily implemented. However, in the practical implementation of the FBP based tomographic reconstruction, it is not possible to measure a large number of projections necessary for the Fourier transform based

techniques to produce highly accurate results. To reduce the aliasing distortions caused by an insufficiency of the input data, the interpolation with respect to sample angle and projection angle based on the limit measurements are used. This allows to decrease some artefacts by generating the required projection data for the number of sampled grid values necessary for displaying an improved reconstructed image [14, 80, 127, 128]. Nevertheless, the main drawbacks of FBP based algorithms are that these algorithms require a strictly determined scanning configuration and are very sensitive to the noise in the experimental data.

Algebraic reconstruction algorithms used in the tomographic imaging assume that the cross section of the object consists of an array of unknowns, and sets up algebraic equations for the unknowns in terms of the measured projection data. Algebraic reconstruction algorithms are typically used in situations where it is not possible to measure a large number of projections, or in case those projections are not uniformly distributed.

The **algebraic reconstruction technique** (ART) based on the Kaczmarz algorithm is an iterative algebraic reconstruction algorithm used for tomographic image reconstruction from sparse data. By using algebraic methods, a square grid is superimposed over the unknown image and image values are assumed to be constant within each cell of the grid. In general, the ART can be defined according to equation 1.4.14 [14, 80, 108, 129]:

$$\mathbf{W}_{M\times N}\mathbf{F}_{N\times 1} = \mathbf{P}_{M\times 1}, \tag{1.4.14}$$

where $\mathbf{F}_{N\times 1}$ is an unknown column vector storing the image values, $\mathbf{P}_{M\times 1}$ – column vector composed of the ray sum values measured with each ray of total M projections, $\mathbf{W}_{M\times N}$ – weight (or coefficient) matrix in which an element ω_{ij} represents a measure of the contribution of the j^{th} cell to the i^{th} ray integral.

Equation 1.4.6 can be solved with an iterative scheme proposed by Kaczmarz, which is expressed with expression 1.4.15 [14, 108]:

$$f_j^{(k+1)} = f_j^{(k)} + \lambda \frac{p_i - \sum_{n=1}^{N} \omega_{in} f_n^{(k)}}{\sum_{n=1}^{N} \omega_{in}^2} \omega_{ij} \quad , \tag{1.4.15}$$

where λ is the relaxation factor (chosen as less than 1), ω_{ij} is the weight factor that determines the amount of influence that the j^{th} grid pixel has on the i^{th} ray. By using Kaczmarz method the algebraic reconstruction starts from an initial guess for the reconstructed object and then performs a sequence of iterative grid projections and correction back-projections until the reconstruction has converged.

The main advantages of ART over FBP based algorithms is that it has better noise tolerance and better handling of sparse and non-uniformly distributed projection data [14, 80, 108, 129].

The **simultaneous iterative reconstruction technique** (SIRT) is known to be useful for Lamb wave tomography because of great flexibility at practically any

scanning geometry and the existence of incomplete data sets. Moreover, the SIRT algorithm is relatively robust, computationally efficient, insensitive to experimental noise and, compared to ART, results in smoother tomographic image reconstruction [106, 109, 126, 130]. Typically, SIRT uses a double-cross hole geometry, presented in Fig. 1.4.3, which allows practically any scanning geometry.

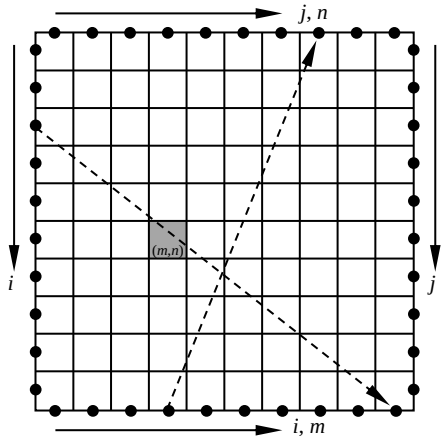

Fig. 1.4.3. Geometry for double-cross hole tomography [126]

The SIRT reconstruction algorithm attempts to solve for the Lamb wave velocity within each grid cell $v[m,n]$, where $[m,n]$ are the cell coordinates, which is done by solving equation 1.4.16 [106, 126]:

$$T[i,j] = \sum_{m,n \in \text{ray}[i,j]} t[i,j,m,n] = \sum_{m,n \in \text{ray}[i,j]} \frac{d[i,j,m,n]}{v[m,n]}, \tag{1.4.16}$$

where $T[i,j]$ is the total time it takes the wave to travel from the transmitter to the receiver, $t[i,j,m,n]$ is the amount of time $\text{ray}[i,j]$ travels within the $\text{cell}[m,n]$, which is equivalent to the length of $\text{ray}[i,j]$ in a $\text{cell}[m,n]$ divided by the cell velocity $v[m,n]$ [106]. The solution of this equation yields a velocity map over the entire region and by giving the operating frequency this velocity map can be converted into a thickness map used to detect defects.

The **probabilistic reconstruction algorithm** (PRA) used in tomographic reconstruction allows flexibility in array geometry selection. Additionally, PRA enables the reconstruction to be performed with good quality and fast speed. The formulation used in the algorithm for defect probability at any given point in space is presented with equation 1.4.17 [14, 67, 131]:

$$P(x,y) = \sum_{k=1}^{N} p_k(x,y) = \sum_{k=1}^{N} A_k \frac{\beta - R}{\beta - 1}, \tag{1.4.17}$$

where $P(x,y)$ is the estimation of the defect probability at position (x,y) within the reconstruction region, $p_k(x,y)$ is the estimation from the k^{th} transmitter-receiver pair, A_k is the input feature of the k^{th} transmitter-receiver pair, N is the total number of the

transmitter-receiver pairs in the sensor network, β is the scaling parameter which controls the size of effective elliptical distribution. For the k^{th} path, R is a ratio of the total distance measured from point (x, y) to the transmitter (x_{1k}, y_{1k}) and to receiver (x_{2k}, y_{2k}), which is defined with equation 1.4.18 [14, 67, 131]

$$R = \frac{\sqrt{(x - x_{1k})^2 + (y - y_{1k})^2} + \sqrt{(x - x_{2k})^2 + (y - y_{2k})^2}}{\sqrt{(x_{1k} - x_{2k})^2 + (y_{1k} - y_{2k})^2}}. \tag{1.4.18}$$

The most crucial part of the PRA is the separation of a given mode and selection of the extracted feature from the k^{th} actuator-sensor pair. Usually, a set of actuator-sensor pair signals is affected when a defect occurs. As a result, the pixel where the defect is located has a dominantly larger probability in the defect distribution probability image compared to other pixels. By using a 2D probability density function and applying the expectation-maximization algorithm one can select a threshold to defect estimation image and estimate the location of a defect.

The **reconstruction algorithm for the probabilistic inspection of damage** (RAPID) has been specifically formulated for applications with ultrasonic guided waves. A major advantage of the RAPID algorithm is that wave diffraction is accounted for by the elliptical location probability distribution.

RAPID consists of two main steps: signal comparison and image reconstruction. Signal comparison is based on damage index estimation, known as signal difference coefficient (SDC), which measures how statistically different the current signal is from a reference signal. The SDC for all transmitter-receiver pairs is estimated according to equation 1.4.19 [111, 131–135]:

$$SDC_{ij} = 1 - \left| \frac{\int_{t_0}^{t_0+\Delta T} \left[x_{ij}(t) - \mu\right]\left[y_{ij}(t) - \mu\right] dt}{\sqrt{\int_{t_0}^{t_0+T} \left[x_{ij}(t) - \mu\right]^2 dt \int_{t_0}^{t_0+\Delta T} \left[y_{ij}(t) - \mu\right]^2 dt}} \right|, \tag{1.4.19}$$

where t_0 is the direct arrival time for each transducer pair, μ is the mean of the corresponding signal, $x_{ij}(t)$ is the current signal, $y_{ij}(t)$ is the reference signal, and ΔT is the time window.

Image reconstruction by using RAPID is done by spatially distributing each obtained SDC value on the image plane in an elliptical pattern where the two foci of the ellipse correspond to the transmitter and receiver locations. The spatial distribution function in which SDC values are distributed is defined according to equation 1.4.20 [111, 132–135]:

$$s_{i,j}(x, y) = \begin{cases} \dfrac{\beta - R_{ij}(x, y)}{1 - \beta}, & \beta > R_{ij}(x, y) \\ 0, & \text{otherwise} \end{cases}, \tag{1.4.20}$$

where β is the shape factor controlling the size of ellipse (represents the size of ultrasonic beam width), which can be defined as the ratio of the sum of distances from point (x, y) to a transmitter *i* and receiver *j* for proper reconstruction image, $R_{ij}(x, y)$ is the ratio of the sum of distance from point (x, y) to the transmitter *i* and receiver *j* to the distance between the transmitter and receiver.

Finally, the image amplitude at each pixel is a linear sum of the location probabilities from each transmitter-receiver $s_{ij}(x, y)$ pair with the total number of transmitter-receiver pairs given by *N*, which is defined with equation 1.4.13 [111, 132–135]:

$$P(x, y) = \sum_{i=1}^{N-1} \sum_{j=i+1}^{N} SDC_{ij} s_{ij}(x, y). \tag{1.4.21}$$

However, if the defect is located not in the middle of the test object, the ray propagation path in each direction becomes different thus resulting in a distorted reconstructed image. Therefore, the variable shape factor is used to reconstruct a real defect image [133]. Despite the advantages of flexibility at any scanning geometry and reconstruction from the sparse data, the main drawback of the proposed algebraic reconstruction algorithms used for tomographic reconstruction is their inefficiency, since a large amount of physical unknowns are needed and required to be updated iteratively thus limiting the application of algebraic reconstruction methods for large-scale systems.

The presented review shows that there is a wide range of available tomographic reconstruction algorithms used for UGW visualisation, which differ in the requirements for projection geometry, reconstruction accuracy, computational speed, etc. All these algorithms traditionally are divided into two main groups – filtered back-projection (FBP) and algebraic reconstruction methods. At the same time, it cannot be unambiguously stated which of the methods presented is the most suitable for a particular case because they require separate studies of the problem in order to reach a compromise between the accuracy of the desired measurements and computational speed.

1.5 Related works in Prof. K. Baršauskas' Ultrasound Research Institute

Prof. K. Baršauskas' Ultrasound Research Institute represents the majority of ultrasonic research groups at Kaunas University of Technology which have been researching ultrasound for more than 50 years. The research of long-range guided wave ultrasonics started in 2004 with the 6th EU Framework programme for Research and Technological Development (FP6). Since then, the institute with its partners has participated in international projects (FP6 and FP7) related to the long-range and medium-range UGW inspection of storage tanks (Condition Monitoring of Large Oil and Chemical Storage Tanks Using Ultrasonic Guided Wave Tomography Without the Need to Empty and Clean the Tank, TANK INSPECT), offshore structures (Development of Ultrasonic Guided Wave Inspection Technology for the Condition Monitoring of Offshore Structures, OPCOM), on and offshore wind turbine blades

(In-situ wireless monitoring of on and offshore WINd TURbine blades using energy harvesting technology, WINTUR), engineering assets (Long Range Ultrasonic Condition Monitoring of Engineering Assets, LRUCM), tidal stream generators (Development of a Condition Monitoring System for Tidal Stream Generator Structures, TIDALSENSE) and sprinkler inspection (Medium Range Ultrasonic Inspection Technique for Detecting Micro-biologically Induced Corrosion in Automatic Fire Sprinkler Systems, SprinkTest) for finding defects, corrosion and condition monitoring of the objects.

During the TANK INSPECT project (2004–2006) the ultrasonic technique for non-destructive inspection of storage tank floor based on the application of the UGW tomography was developed. The pilot investigations were carried out on a real aboveground storage tank under *in situ* conditions proved the suitability of the technique for monitoring the condition of a tank floor. Additionally, the investigation of propagation of UGW in the storage tank floor has demonstrated a close relation between the properties of propagating waves and the presence of non-homogeneities or corrosion.

The objective of the OPCOM project (2005–2008) was to develop NDT methods for offshore structures using UGW. During the project, permanently mounted ultrasonic sensors and systems for continuous monitoring of offshore structures for crack and corrosion were developed.

The objective of the LRUCM project (2005–2008) was to develop a novel long-range ultrasonic condition monitoring technological tool for finding defects and corrosion in a wide range of degrading engineering assets, e.g. pipelines, offshore platforms, cable-stayed bridges, etc. During the period of the project, the institute proposed the optimal spatial arrangement of transducer arrays for long-range ultrasonic NDT.

The objective of the WINTUR project (2009–2011) was to develop an advanced integrated system for real-time SHEM and impending failure detection for on and offshore wind turbine blades, enabling a fundamental realignment of inspection/maintenance strategies that are based on the actual condition of the blades. During the project, the institute developed inspection and monitoring techniques for wind turbine blades based on the application of guided waves.

During the TIDALSENSE project (2009–2011), the SHM technique for tidal stream generators using a combination of long-range guided waves and acoustic emission was developed. The configuration and arrangement of the transducers for optimal generation and reception of UGW were determined and the technique of automatic classification of defect-free and defective regions of hydrofoil was developed.

The objective of the SprinkTest project (2013–2015) was the development of an automatic fire sprinkler inspection method based on the medium-range ultrasonic guided waves test. During the project, with the collaboration with partners, the numerical simulations, experiments and method validation was performed.

1.6 Conclusions of the Chapter 1

The analysis of the measurement methods used for detecting corrosion-caused defects in ASTs and their floor constructions demonstrated that inspection could be performed by using a series of different NDT methods based on different physical phenomena. Each of the aforementioned methods has its own advantages and disadvantages. However, most of the common inspection methods, such as the PECT, RFECT, MFL and conventional UT require the storage tank to be emptied and cleaned before any inspection could be performed. Additionally, all the mentioned measurement methods allow to detect the defects only locally and are time-consuming procedures. To overcome many of the shortcomings of the earlier mentioned inspection methods the AET for the inspection of the storage tanks is used. It allows to inspect the tank without emptying it, cleaning the floor and scanning point by point from the outer perimeter of the tank. However, AET is sensitive to background conditions and could not be performed under specific environmental conditions.

The only technique which enables to inspect or at least assess the corrosion of the storage tank floor without accessing into the tank is the ultrasonic inspection technique based on the application of GW together with ultrasonic transmission tomography. The analysis revealed that this technique has a potential to obtain a 2D map of general corrosion damage of the tank floor. However, the investigations carried out by different authors do not give the answers to the most important questions: firstly, the necessity to know the absolute value of attenuation as only it, and not the relative distribution can be related to the level of corrosion or to the level of thinning of plates in the storage tank floor. The second question relates to the fact that previous investigations do not explain the difference of losses on lap joint welds obtained by modelling and on real storage tanks. The question also relates to the regularities of UGW propagation through the lap joints when they are under the angle with respect to wave propagation path. The third essential aspect is the assessment of expected resolution and the sensitivity of UGW tomography to different levels of thickness reduction.

Therefore, in order to develop a technique for assessing the corrosion in the tank floor from the outside, the following tasks have to be solved:

- a development of numerical models for the investigation of UGW propagation in the tank floor and its construction elements and to assess the expected losses, propagation distances, resolution, sensitivity and possible changes during exploitation;
- the experimental verification of the developed models and the investigation of regularities observed by modelling;
- an investigation of UGW tomography technique and the development of such one which enables to detect damage in the storage tank floor and a selection of optimal parameters for tomographic reconstruction;
- theoretical and experimental verification of the proposed measurement method and estimation of the expected measurement uncertainties.

2. AN INVESTIGATION OF ULTRASONIC GUIDED WAVES PROPAGATION IN THE FLOOR OF A STORAGE TANK

The typical AST used for petrochemical products is constructed in accordance with the BS EN 14015:2004 standard (Specification for the Design and Manufacture of Site Built, Vertical, Cylindrical, Flat-Bottomed, Above Ground, Welded, Steel Tanks for the Storage of Liquids at Ambient Temperature and Above) [136]. Based on this standard, the floor of a storage tank is constructed of a set of 6–8 mm thick steel plates joined together by using multiple lap joint welds and may have the diameter up to 100 m (Fig. 2.1). As it was described in the previous chapter, the UGW propagate in planar structures, such as plates or sheets and may possess an unlimited number of modes. However, for ultrasonic measurements, mostly the fundamental asymmetric A_0 and symmetric S_0 wave modes are used. The transmission, reflection and mode conversion of these waves take place on all non-uniformities in the storage tank floor, including welds and defects, and cause energy losses of the propagating guided waves and directly influence the achievable inspection range. For this reason, it can be difficult to understand the UGW propagation in the storage tank floor and its interaction with discontinuities, as well as to interpret the UGW signals. Therefore, in order to answer the main questions related to the propagation of the UGW, numerical modelling is widely used.

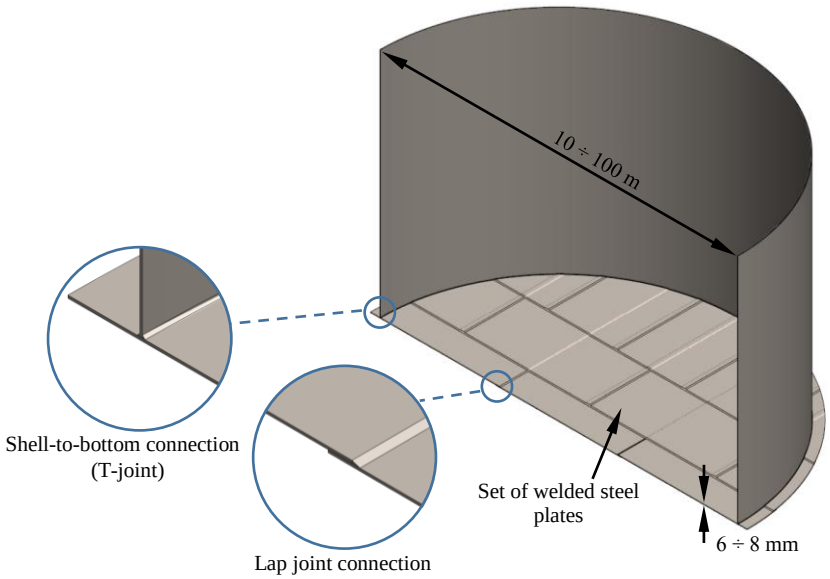

Fig. 2.1. The typical geometry of an aboveground storage tank

The aim of the present research is to investigate the UGW propagation through the shell-to-bottom (T-joint) and lap joint connections of the welded steel plates, commonly used in the construction of a storage tank floor (Fig. 2.1). This affects the UGW propagation and is not sufficiently investigated. The most important aspects which determine the diameter of a tank which can be inspected are the losses of UGW

propagating through the multiple joints of the welded storage tank plates which should be estimated, and it is important to analyse how they are affected by such factors as:

- the width of plates overlap zone;
- operating frequency;
- adhesion between steel plates;
- applied additional fluid loading, etc.

To answer those questions on the UGW propagation and determine the expected transmission losses, the numerical investigation by using the finite element (FE) method was carried out.

2.1 An analysis of ultrasonic guided waves propagation through the shell-to-bottom junction

In the case of long-range UGW application, the objects under testing are large, consequently, the test samples for the development of an inspection technique also are large and expensive to manufacture, as well as impractical to use in laboratory conditions. Due to this reason, it was decided to use a scaled-down physical, and as well numerical model of the object simultaneously in a corresponding way changing the frequency. Such approach is valid, as the properties of UGW depend on the frequency-thickness product $f \cdot d$. It means that if the dimensions of the object, including plate thickness, are reduced by the factor N and, at the same time, the frequency of the selected ultrasonic waves is higher by the same factor N, the properties of UGW will be the same. Thus, instead of investigating large objects, it is reasonable to carry out investigations with scaled-down models and verify the determined regularities on a real-sized object afterwards.

In order to answer the questions related to UGW propagation in a storage tank floor and its construction elements, such as shell-to-bottom (T-joint) and lap joint connections, the models with the scaling factor 1:8 were developed and investigated. The investigation was carried out by using stainless steel plates, elastic properties of which are presented in Table 2.1.1.

Table 2.1.1. The elastic properties of the stainless steel alloy used in modelling

Material	Density ρ, kg/m^3	Young's modulus E, GPa	Shear modulus G, GPa	Poisson's ratio v
Stainless steel alloy	8,000	193	77.2	0.31

The dispersion curves of the phase c_{ph} and group c_{gr} velocities in the 8 mm thick and in the scaled-down 1 mm thick stainless steel alloy plates were calculated using the SAFE method. The obtained dispersion curves are presented in Fig. 2.1.1. The dashed line denotes the frequency selected for investigations. This frequency for real-size objects is 50 kHz, and for scaled-down model – 400 kHz. The product fd in both cases is the same. The velocities of the fundamental UGW modes in the case of 8 mm and in the case of the scaled-down 1 mm thick stainless steel plates at the selected frequency are presented in Table 2.1.2.

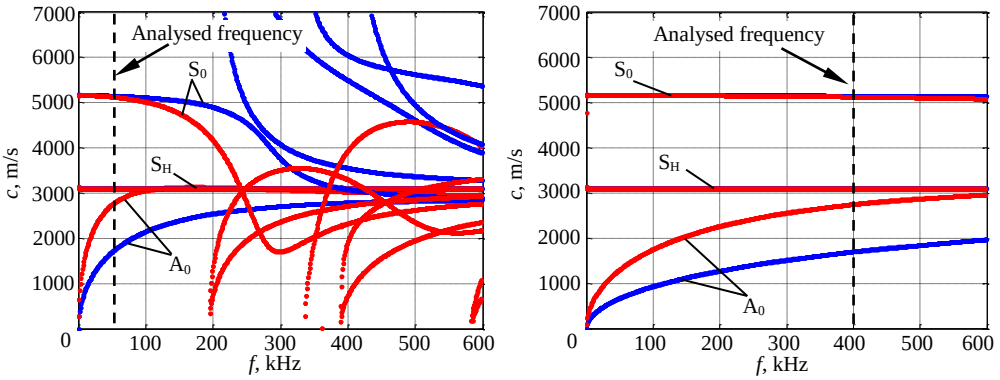

Fig. 2.1.1. The UGW phase (blue) and group (red) velocities dispersion curves for 8 mm thick (a) and 1 mm thick stainless steel plate (b)

Table 2.1.2. The velocity of the A_0, S_0 and S_H guided wave modes for the 8 mm and 1 mm thick stainless steel plates

Guided wave mode	8 mm thick stainless steel plate (f = 50 kHz)		1 mm thick stainless steel plate (f = 400 kHz)	
	Phase velocity c_{ph}, (m/s)	Group velocity c_{gr}, (m/s)	Phase velocity c_{ph}, (m/s)	Group velocity c_{gr}, (m/s)
Asymmetric A_0	1,698	2,747	1,701	2,751
Symmetric S_0	5,157	5,132	5,156	5,134
Shear horizontal S_H	3,107	3,105	3,106	3,106

The modelling of the UGW propagation was based on the analysis of the symmetric S_0 wave mode propagation because of several key properties of this wave mode that could be predicted from literature analysis and presented in Fig.1.2.3, Fig.1.2.4 and Fig.2.1.1:

- the group velocity c_{gr} of the symmetric S_0 wave mode is higher, ensuring that it arrives before any other modes, thus making it easier to identify and separate the time interval in the measured signals;
- symmetric S_0 wave mode is less sensitive to the liquid boundary interaction. It has lower attenuation and leakage losses compared to the asymmetric A_0 wave mode; thus it enables stronger signals to be received and longer propagation distance.

In order to investigate the UGW propagation, transmission efficiency of the selected symmetric S_0 wave mode and possibilities to use it for the inspection of a storage tank, numerical simulation of the wave propagation through the shell-to-bottom (T-joint) junction consisting of both-side and one-side filled welds, presented in Fig. 2.1.2, was carried out by applying the finite element (FE) method. The ANSYS finite element software was used to obtain the wave propagation through the 2D geometry which includes an implicit algorithm with Newmark time integration method for solving the transient wave propagation.

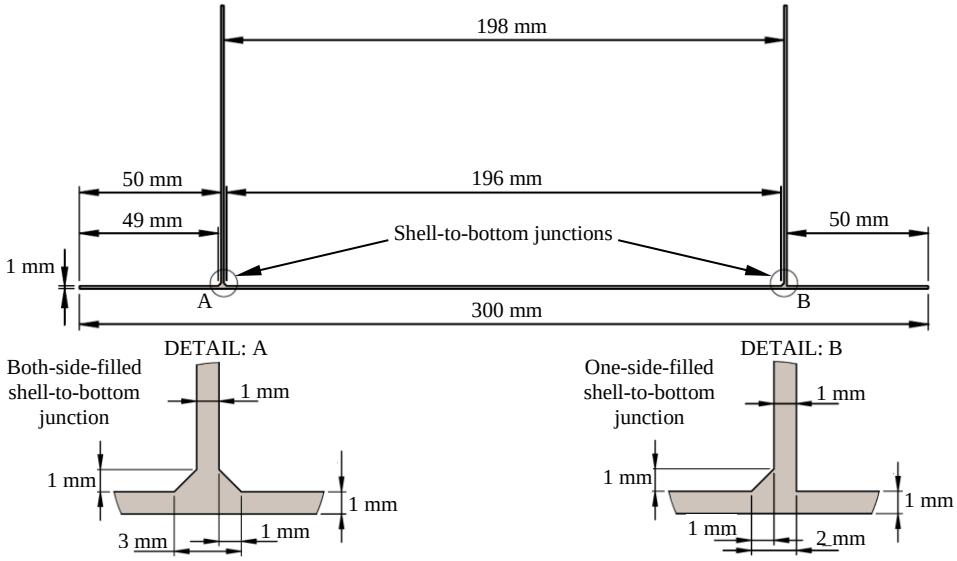

Fig. 2.1.2. The 2D model of the structure under investigation with shell-to-bottom junctions

Research on elastic wave propagation is based on the assumptions of linear elasticity. The general Navier equation of elastic wave motion in a matrix form is defined according to equations 2.1.1–2.1.5 [137–145]:

$$\mathbf{M}\ddot{\mathbf{u}} + \dot{\mathbf{C}}\mathbf{u} + \mathbf{K}\mathbf{u} = \mathbf{F}\,, \tag{2.1.1}$$

$$\mathbf{M} = \int_{\Omega} \rho \mathbf{N}^T \mathbf{N} d\Omega\,, \tag{2.1.2}$$

$$\mathbf{C} = \int_{\Omega} \mathbf{N}^T \kappa \mathbf{N} d\Omega\,, \tag{2.1.3}$$

$$\mathbf{K} = \int_{\Omega} \left[\mathbf{L}\mathbf{N}\right]^T \mathbf{D}\left[\mathbf{L}\mathbf{N}\right] d\Omega\,, \tag{2.1.4}$$

$$\mathbf{F} = \int_{\Omega} \mathbf{N}^T f_b d\Omega + \int_{\Gamma} \mathbf{N}^T \bar{\mathbf{t}} d\Gamma\,, \tag{2.1.5}$$

where $\mathbf{M}$ is the mass matrix, $\mathbf{C}$ is the damping matrix, $\mathbf{K}$ is the stiffness matrix, $\mathbf{u}, \dot{\mathbf{u}}, \ddot{\mathbf{u}}$ – are the nodal displacement, velocity and acceleration vectors, respectively, $\mathbf{F}$ is the externally applied nodal forces, ρ is the mass density, κ is the damping property, $\mathbf{N}$ is the shape function, $\mathbf{D}$ is the elasticity matrix, $\mathbf{L}$ is the strain-displacement operator, f_b is the body force, $\bar{\mathbf{t}}$ is the traction vector defined on the Neumann boundary Γ_N. To simplify the model, a linear elastic solid is considered and no damping are added in this study ($\mathbf{C}$=0).

The model under investigation was considered to be infinite in *z* direction, so that the plane strain condition which assumes that all strains occur in *x*-*y* direction is used and there are no strains in the *z*-direction. PLANE42 elements are used for 2D modelling of solid structures. The element has 4 nodes, each with 2 degrees of

freedom – translations in the nodal x and y directions. To ensure good spatial resolution in the FE modelling, 10 to 20 nodes per wavelength are normally required. The finite element size was selected according to equation 2.1.6, so that there would be on the order of 20 nodes per wavelength [137, 138, 140, 141, 146]:

$$l_e = \frac{\lambda_{\min}}{n}, \tag{2.1.6}$$

where l_e is the element length, $\lambda_{\min}$ is the shortest wavelength of interest, $n = 10 \div 20$ is the number of nodes per wavelength. To obtain the desired accuracy, the spatial size of the element was set to 0.2 mm, which corresponds to 21 elements per wavelength in accordance with the minimum wavelength of the slowest asymmetric A_0 wave mode at the frequency of 400 kHz (Table 2.1.2).

Time integration step that gives accurate solutions in an efficient manner was selected according to equation 2.1.7 [137, 138, 140]:

$$dt < \frac{1}{20 f}, \tag{2.1.7}$$

where f is the frequency of interest. The discretization step in the time domain calculated according to the presented equation is dt = 10 ns. The time interval of $\Delta t = 0 \div 130$ μs was selected for modelling wave propagation to ensure that the symmetric S_0, as well the newly generated UGW modes pass the whole distance in the analysed model.

For the excitation of UGW in the stainless steel plate, 5 periods of 400 kHz sine-burst with a Gaussian envelope signal was used. The bandwidth of the excitation signal at -6 dB level is from 335 kHz to 465 kHz. The waveform of the applied normalised excitation signal and its spectrum are presented in Fig. 2.1.3a and Fig. 2.1.3b, respectively.

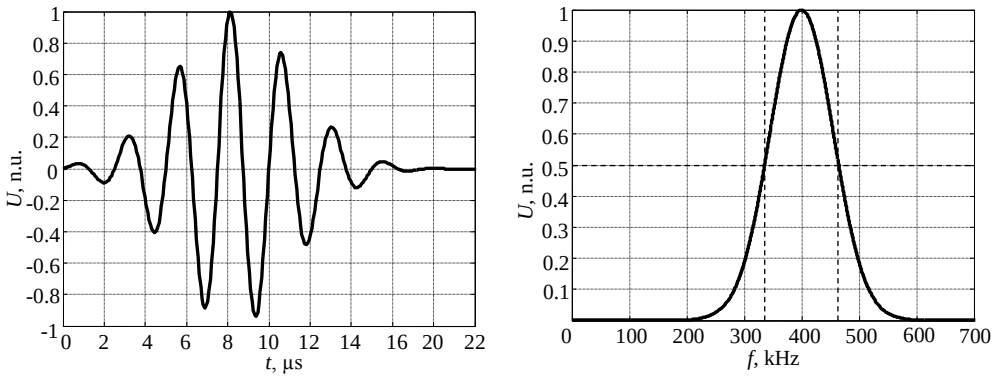

a) b)

Fig. 2.1.3. The waveform of the 400 kHz excitation signal (a) and the amplitude spectrum of the excitation signal (b)

In order to determine the transmission efficiency and expected transmission losses $\alpha_{S0}(f)$ due to the shell-to-bottom junction, two cases of ultrasonic symmetric

S_0 guided wave mode propagation through the shell-to-bottom junction, presented in Fig. 2.1.4, were investigated. In the first investigation, presented in Fig. 2.1.4a, the excitation of UGW was performed by applying a uniformly distributed and concentrated force in the longitudinal direction to the vertical wall of the model joined to the bottom plate by both-side filled weld (10 mm above the weld). In the second, presented in Fig. 2.1.4b, the uniformly distributed and concentrated force was applied at the edge of welded plates in the longitudinal direction. The thickness of the stainless steel plates was 1 mm and the width of the excitation zone in the performed FE analysis was set to be 1 mm for both cases. It should be noted that the models bellow are presented on different vertical and horizontal scales.

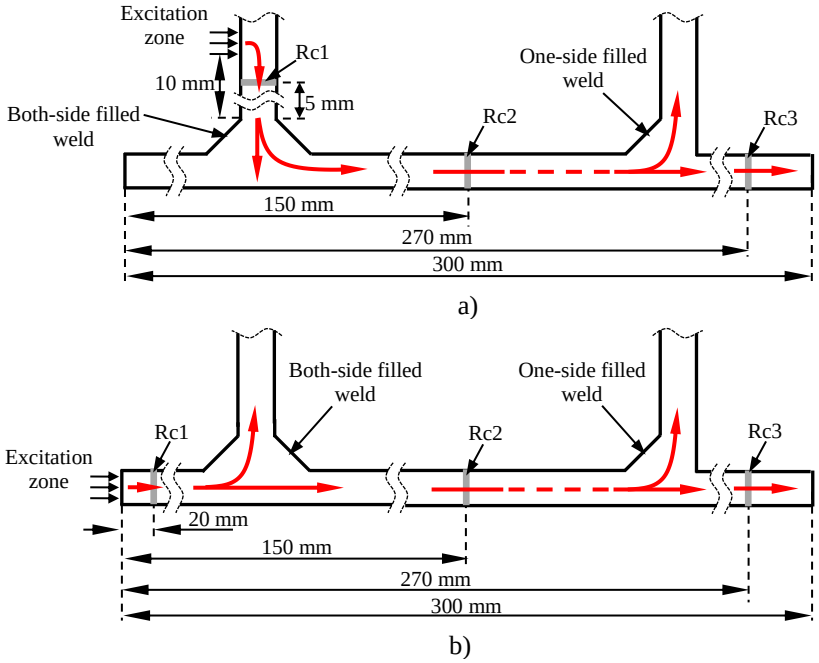

Fig. 2.1.4. Models used for investigating UGW propagation through the shell-to-bottom junction when excitation is performed on the vertical wall (a) and on the edge of welded plates (b)

To measure the transmission losses $\alpha_{S0}(f)$ of the symmetric S_0 UGW mode due to shell-to-bottom junction, three areas have been chosen in the model corresponding to the position before the shell-to-bottom junction, after first and second shell-to-bottom junctions, respectively. In the case of UGW excitation from the vertical wall of the model, signals of the longitudinal particle velocity were recorded to be Rc1 – 5 mm from excitation zone, Rc2 – 150 mm and Rc3 – 270 mm from the plate edge (Fig. 2.1.4a), which corresponds to the position before weld, after the first (both-side filled) and the second (one-side filled) welds, respectively. The distances were selected so that to ensure that the mode of interest separates in time from the other propagating GW modes as far as possible. It is noteworthy that no wave

dispersion was considered in the simulation. The mean value of the longitudinal particle velocity across the plate thickness was calculated by using equation 2.1.8:

$$u(t) = \frac{1}{N_e} \sum_{n-1}^{N_e} u_n(t), \tag{2.1.8}$$

where N_e is the number of nodes and u_n is the nodal value of the longitudinal particle velocity. The obtained waveforms of signals in the time-domain of the UGW propagation through the shell-to-bottom junction when excitation was performed on the vertical wall of the model (Fig. 2.1.4a) are presented in Fig. 2.1.5.

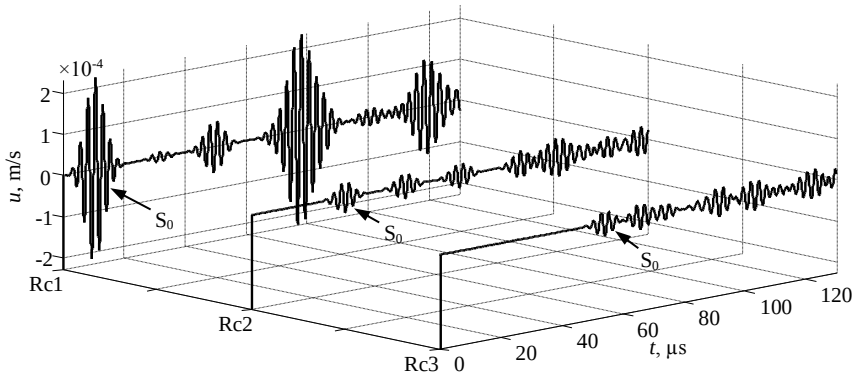

Fig. 2.1.5. The waveforms of signals obtained during the excitation from the wall: Rc1 – before shell-to-bottom junction, Rc2 – after the 1st (both-side filled) shell-to-bottom junction and Rc3 – after the 2nd (one-side filled) shell-to-bottom junction

The fastest propagating symmetric S_0 UGW mode signals were selected from the time diagrams of the received signals by using the Hanning window, and the frequency spectra $U(f)$ were calculated using the Fourier transform (FT). For better comparison of the frequency spectra, the results were normalised in respect of the reference signal spectra, according to the expressions presented below:

$$U_{\mathrm{r}}(f) = \mathrm{FT}[u_{\mathrm{r}}(t)], \tag{2.1.9}$$

$$U_{\mathrm{r}}^{\mathrm{n}}(f) = \frac{U_{\mathrm{r}}(f)}{\max(U_{\mathrm{r}}(f))},$$

$$U_{\mathrm{k}}^{\mathrm{n}}(f) = \frac{\mathrm{FT}[u_{\mathrm{k}}(t)]}{\max(U_{\mathrm{r}}(f))}, \tag{2.1.10}$$

where $u_{\mathrm{r}}(t)$ is the reference ultrasonic signal (picked-up by the virtual receiver Rc1 before the weld), $u_{\mathrm{k}}(t)$ is the ultrasonic signal transmitted through the weld (picked-up by the virtual receivers Rc2 and Rc3 behind the weld, respectively). The transmission losses $\alpha_{S0}(f)$ of the S_0 guided wave mode signals caused by the shell-to-bottom connection in the wave propagation path were obtained by comparing the frequency spectra of the signals received before, after the first and second joints,

respectively. The transmission losses $\alpha_{S0}(f)$ of the selected wave mode were calculated by using equation 2.1.11 presented below

$$\alpha_{S0}(f) = -20\lg\left|\frac{\mathrm{FT}[u_k(t)]}{\mathrm{FT}[u_r(t)]}\right|. \quad (2.1.11)$$

The results of the symmetric S_0 UGW mode spectra $U^n(f)$ and transmission losses $\alpha_{S0}(f)$ as it passes through the shell-to-bottom junction are presented in Fig. 2.1.6. During the investigation, it was presumed that the values of transmission losses obtained from frequency spectra ratio are reliable within the bandwidth where the spectra of the reference signal reduces by -20 dB. Under such assumption, the bandwidth where the measurements are reliable are presented with dashed lines in Fig. 2.1.6b.

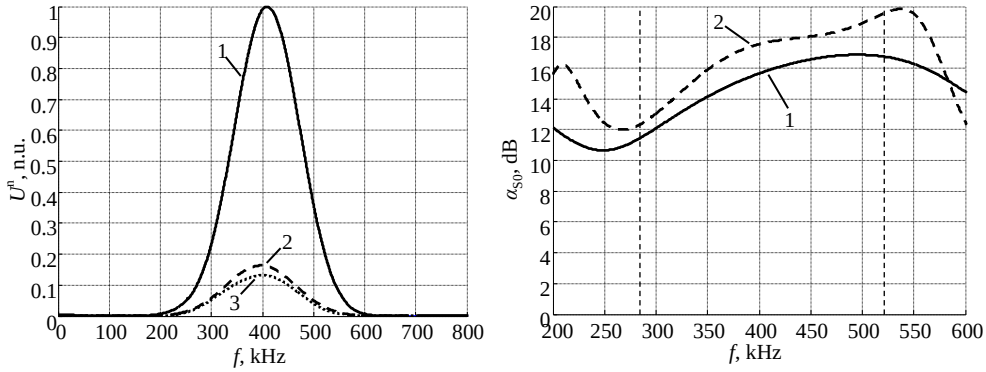

Fig. 2.1.6. Spectra of the S_0 UGW mode 1 – before, 2 – after the 1st, 3 – after the 2nd shell-to-bottom junction (a), b) the transmission losses $\alpha_{S0}(f)$ of the S_0 mode 1 – after the 1st, 2 – after the 2nd shell-to-bottom junction when excitation is performed from the vertical wall of the model (b)

The results demonstrate that the amplitude of the symmetric S_0 UGW mode as it passes through the both-side filled shell-to-bottom junction decreases by 15.9 dB at the central frequency of the 400 kHz of the excitation signal when excitation is performed on the vertical wall of the model. Meanwhile, the transmission losses $\alpha_{S0}(f)$ of the S_0 mode after the second one-side filled shell-to-bottom junction have been estimated to be 1.7 dB.

In the case of excitation on the edge of the model, signals of the longitudinal particle velocity were measured: Rc1 – 20 mm, Rc2 – 150 mm and Rc3 – 270 mm distances from the excitation zone (Fig. 2.1.4b). The mean value of the longitudinal particle velocity across the plate thickness and transmission losses $\alpha_{S0}(f)$ of the analysed S_0 wave mode were calculated by using equations 2.1.8 and 2.1.11. The obtained waveforms of the propagating signals, spectra $U^n(f)$ of the selected symmetric S_0 UGW mode, and the estimated transmission losses $\alpha_{S0}(f)$ as it passes

through the shell-to-bottom junction connections are presented in Fig. 2.1.7 and, Fig. 2.1.8, respectively.

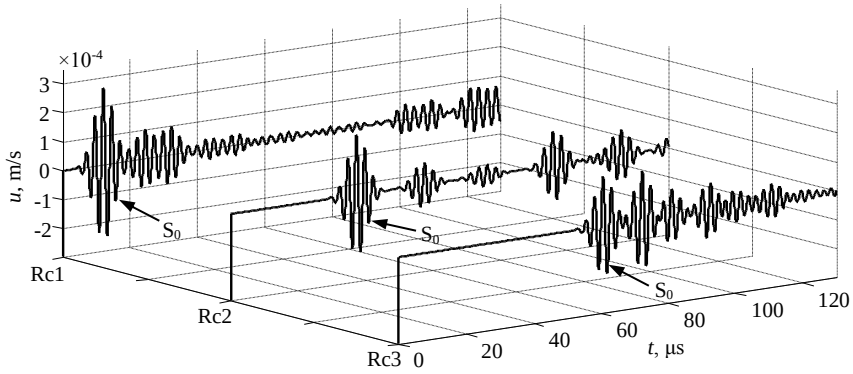

Fig. 2.1.7. The waveforms of signals obtained during excitation on the edge: Rc1 – before shell-to-bottom junction, Rc2 – after the 1st shell-to-bottom junction and Rc3 – after the 2nd shell-to-bottom junction

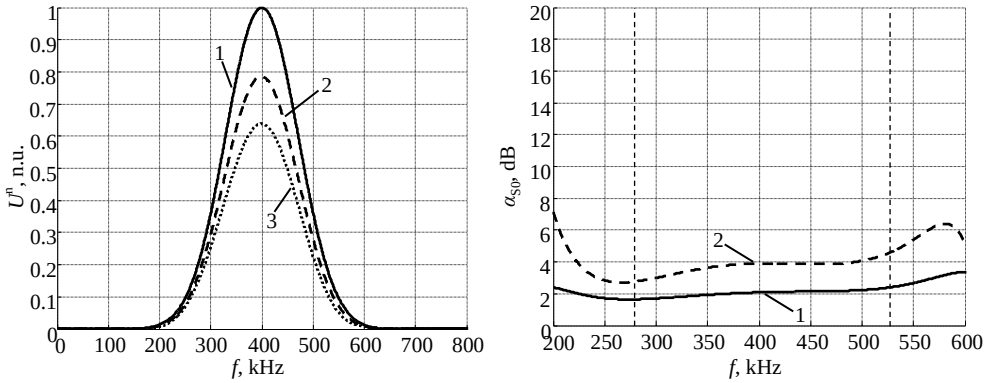

a) b)

Fig. 2.1.8. Spectra of the S_0 UGW mode 1 – before, 2 – after the 1st and 3 – after the 2nd shell-to-bottom junction (a), the transmission losses $\alpha_{S0}(f)$ of the S_0 wave mode 1 – after the 1st and 2 – after the 2nd shell-to-bottom junction when excitation is performed on the edge of the model (b)

The results demonstrate that in case of excitation on the edge of the presented model (Fig. 2.1.4b) the transmission losses $\alpha_{S0}(f)$ of the symmetric S_0 wave mode as it passes through the both-side filled shell-to-bottom junction are 2.1 dB at the 400 kHz centre frequency of excitation signal. Meanwhile, the transmission losses of the S_0 mode after one-side filled shell-to-bottom junction were estimated to be 1.8 dB. The results of different UGW excitation and wave transmission through the shell-to-bottom junction cases indicate that the transmission losses $\alpha_{S0}(f)$ of the symmetric S_0 wave mode when the transmission is from the shell (wall) to the bottom are up to 14 dB higher than it was estimated in the case of excitation from the edge. This suggests that significantly stronger UGW signals could be expected during the measurements on the edge of the storage tank floor.

The investigation of UGW transmission efficiency through the shell-to-bottom junction at different excitation signal frequencies was carried out in order to evaluate the operation frequency-dependent transmission losses $\alpha_{S0}(f)$ of the symmetric S_0 guided wave mode when excitation is performed on the edge of the welded plates by using the configuration presented in Fig. 2.1.4b. The frequency of the sine-burst with Gaussian envelope 5-periods excitation signal was changed in the frequency range from 150 kHz up to 500 kHz with the step of 25 kHz. The transmission losses $\alpha_{S0}(f)$ of the symmetric S_0 wave mode were estimated by using equations 2.1.8 and 2.1.11 taking only the value corresponding to the central frequency of the excitation signal. The results of symmetric S_0 UGW mode transmission losses $\alpha_{S0}(f)$ as it passes through the shell-to-bottom junction with both-side and one-side filled welds are presented in Fig. 2.1.9. The approximation of the observed discrete transmission losses of S_0 UGW mode results after the first and the second shell-to-bottom junctions are presented by solid and dashed lines, respectively.

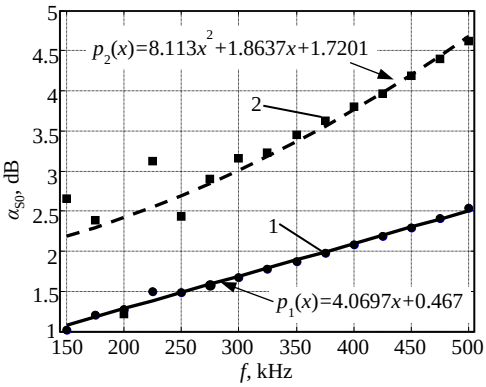

Fig. 2.1.9. The transmission losses $\alpha_{S0}(f)$ of S_0 UGW mode transmitted through the shell-to-bottom junction at different excitation signal frequencies: 1 – after the 1st (both-side filled) and 2 – after the 2nd (one-side filled) shell-to-bottom junctions

The numerical modelling demonstrated that due to the shell-to-bottom junction in the direct wave propagation path, when an excitation signal of different frequency is applied to the edge of the shell-to-bottom junction model, the transmission losses $\alpha_{S0}(f)$ of the propagating symmetric S_0 UGW mode increase practically in a linear manner with frequency. Meanwhile, the observed distribution of the signal transmission losses $\alpha_{S0}(f)$ at a lower frequency range after the second one-side filled shell-to-bottom junction are mainly caused by wave scattering and overlapping of the direct, newly generated, and reflected signals in the time-domain. The average value of variation of transmission losses after both-side $\Delta\overline{\alpha}_{S0\_1}$ and one-side $\Delta\overline{\alpha}_{S0\_2}$ filled shell-to-bottom junction due to the shift of excitation frequency and deviation σ_{S0_1}, σ_{S0_2} of results, in the case of linear approximation, were estimated by using the following equations:

$$\Delta\overline{\alpha}_{S0\_1} = \frac{1}{n}\sum_{i=1}^{n}\left(\alpha_{S0\_1,i+1}(f) - \alpha_{S0\_1,i}(f)\right), \tag{2.1.12}$$

$$\sigma_{S0\_1} = \sqrt{\frac{1}{n-1}\sum_{i=1}^{n}\left|\left(\alpha_{S0\_1,i+1}(f) - \alpha_{S0\_1,i}(f)\right) - \Delta\overline{\alpha}_{S0\_1}(f)\right|^2}\,, \tag{2.1.13}$$

$$\Delta\overline{\alpha}_{S0\_2} = \frac{1}{n}\sum_{i=1}^{n}\left|\left(\alpha_{S0\_2,i+1}(f) - \alpha_{S0\_2,i}(f)\right) - \left(\alpha_{S0\_1,i+1}(f) - \alpha_{S0\_1,i}(f)\right)\right|, \tag{2.1.14}$$

$$\Delta\alpha_{S0\_1,i} = \alpha_{S0\_1,i+1}(f) - \alpha_{S0\_1,i}(f), \tag{2.1.15a}$$

$$\sigma_{S0\_2} = \sqrt{\frac{1}{n-1}\sum_{i=1}^{n}\left|\left[\left(\alpha_{S0\_2,i+1}(f) - \alpha_{S0\_2,i}(f)\right) - \Delta\alpha_{S0\_1,i}\right] - \Delta\overline{\alpha}_{S0\_2}(f)\right|^2}\,, \tag{2.1.15b}$$

where $\alpha_{S0\_1,i}$, $\alpha_{S0\_2,i}$ are the transmission losses of the symmetric S_0 guided wave mode after both-side filled and one-side filled shell-to-bottom junctions, respectively; $i = 1 \div n$, n is the total number of measurement points at which transmission losses were measured. It was estimated that the average change of the symmetric S_0 wave mode transmission losses $\Delta\overline{\alpha}_{S0\_1}$ as it passes the both-side filled shell-to-bottom junction is 0.108 ± 0.052 dB at the 25 kHz excitation frequency shift. Meanwhile, the average change of transmission losses $\Delta\overline{\alpha}_{S0\_2}$ after one-side filled shell-to-bottom junction were expected to be 0.085 ± 0.055 dB at the 25 kHz excitation frequency shift, considering only the results of measurement (in the frequency bandwidth from 275 kHz to 500 kHz) where no significant variation of transmission losses were observed.

The finite element analysis of the symmetric S_0 UGW mode propagation through the shell-to-bottom junction demonstrated that the overall S_0 wave mode amplitude transmitted through the joint is strongly dependent on the selected excitation location. The measurement of transmission losses $\alpha_{S0}(f)$ has shown that significantly stronger symmetric S_0 UGW mode signals could be expected during the measurements on the edge of the tank floor. Moreover, the analysis of S_0 wave mode propagation through the shell-to-bottom junction has shown that the transmission losses $\alpha_{S0}(f)$ of the symmetric S_0 wave mode are linearly dependent and increase with the excitation frequency.

2.2 Transmission of ultrasonic guided waves through the lap joint

A typical storage tank floor used for petrochemical products consists of a set of carbon steel plates joined together by using two types of welding – butt-weld or lap joint welds. However, the most common and frequently used joint in the construction of the tank floor is based on the use of lap joint welds which are more than adequate for the service conditions and require no expensive weld preparation. Nevertheless, they are considered to be more complicated from the point of view of UGW

propagation, because of the occurring mode conversion, wave scattering at plate overlap region, etc. Therefore, the regularities of the UGW propagation through the lap joint welded plates depending on their parameters, such as the overlap length, operating frequency and bonding state condition should be considered as well in order to successfully apply UGW for the inspection of a storage tank floor. The purpose of this research is to assess lap joint-dependent transmission losses $\alpha_{S0}(f)$ of the symmetric S_0 wave mode for a single welded lap joint connection and determine how they are affected by the width Δl of the lap joint and applied excitation signal frequency.

In order to investigate how the overlap zone width Δl of a single welded lap joint connection influences the propagation of the symmetric S_0 UGW mode and its transmission losses $\alpha_{S0}(f)$, numerical modelling was carried out using the finite element (FE) method. The analysis of UGW propagation was performed by using the model of a lap joint presented in Fig. 2.2.1. It should be noted that the model is presented on different vertical and horizontal scales.

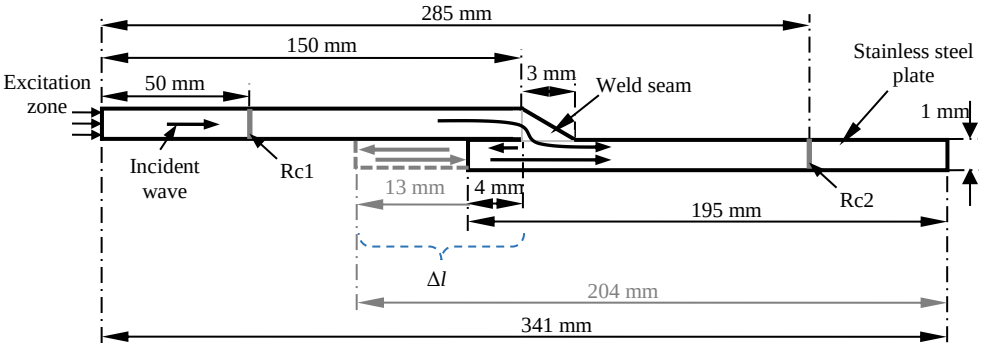

Fig. 2.2.1. The model used for the investigation of the S_0 UGW mode transmission through lap welded plates of different overlap zone width Δl

Four-node PLANE42 linear elements were used to represent the 2D section in plane strain. The finite element size was selected to be 0.2 mm. The discretization step in the time domain was selected to be dt = 10 ns and the time interval used for the modelling of elastic wave propagation was $\Delta t = 0 \div 80$ μs. The overlap zone width Δl of the lap joint between plates was gradually changed from 4 mm to 13 mm by a step of 1 mm. The investigation of the symmetric S_0 UGW mode propagation through a single lap joint was performed by applying 5 periods of 400 kHz sine-burst with the Gaussian envelope signal, which has been described in Section 2.1 and presented in Fig. 2.1.3, to the edge of the model in the longitudinal direction. The elastic properties of the material used in the analysis were the same as presented in Table 2.1. The attenuation of UGW was not considered in the model.

The signals corresponding to the fastest propagating symmetric S_0 UGW mode were acquired by selecting sets of nodes at positions Rc1 – 50 mm and Rc2 – 285 mm away from the excitation zone, so as to avoid overlapping of the direct, newly generated at lap weld and back-reflected signals in the time domain. The mean value of the longitudinal particle velocity across the thickness of the plate was calculated by

using equation 2.1.8. The waveforms of signals in the time domain of the symmetric S_0 wave mode for different overlap zone widths Δl are presented in Fig. 2.2.2. The transmission losses $\alpha_{S0}(f)$ of the analysed symmetric S_0 UGW mode as it passes through the lap joint welded connection were calculated according to equation 2.1.11 by comparing the frequency spectra of the symmetric S_0 mode signals measured before lap joint with the virtual receiver Rc1 and after it measured with virtual receiver Rc2. The transmission losses $\alpha_{S0}(f)$ of the symmetric S_0 wave mode for the current lap joint width Δl were estimated taking only the value corresponding to the frequency of f = 400 kHz. The dependency of S_0 wave mode transmission losses on the width of the lap joint overlap zone is presented in Fig. 2.2.3, where dots denote the values of transmission losses obtained by FE analysis, and the solid line denotes the interpolation by a piecewise cubic Hermite polynomial.

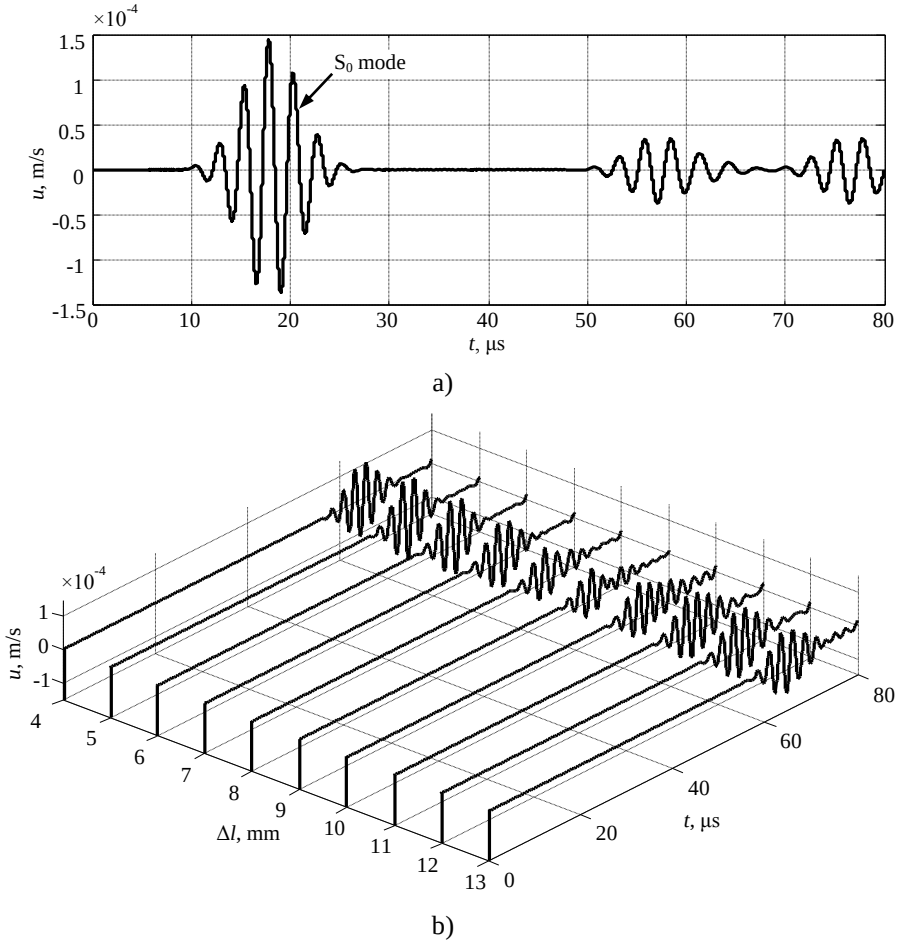

Fig. 2.2.2. The waveforms of signals measured before lap joint connection at Rc1 position (a), after lap joint connection at Rc2 position at different overlap zone widths Δl (b)

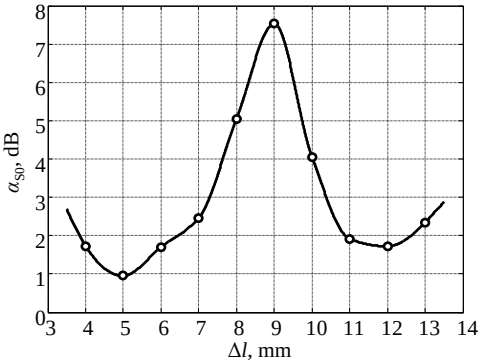

Fig. 2.2.3. The transmission losses $\alpha_{S0}(f)$ of the S_0 guided wave mode at different lap joint overlap widths Δl (dots – FE analysis results, solid line – interpolated by piecewise cubic Hermite polynomial)

It can be observed that the width of the overlap zone Δl in the welded lap joint connection influences the transmission losses $\alpha_{S0}(f)$ of the analysed symmetric S_0 UGW mode, which varies from 0.95 dB/weld to 7.53 dB/weld depending on the width of the lap joint. The results demonstrate that the highest transmission losses $\alpha_{S0}(f)$ for the symmetric S_0 wave mode are obtained when the overlap zone between lap joint connected stainless steel plates is 9 mm. The dependence of transmission losses $\alpha_{S0}(f)$ can be explained by the fact that waves are reflecting back and forth within the free edge of the overlapped part of the plate and produces a series of signals which interfere with each other and become essentially dependent on the length of the propagation path, defined by the width of the overlapped zone. On the other hand, it means that it is dependent on the wavelength λ of the symmetric S_0 wave mode.

Since the connections used for constructing the storage tank floor are not symmetrical, they might possess different lap joint width Δl and orientation-dependent transmission losses. For this purpose, numerical modelling was carried out when lap joint connection is oriented in the opposite direction with respect to wave propagation (bottom-top wave transmission) direction than it was presented in Fig. 2.2.1 (top-bottom wave transmission). UGW propagation was analysed by using the differently-oriented model of lap joint weld presented in Fig. 2.2.4, according to which the elastic wave transmission is performed from the bottom plate into the top (upper) plate. The numerical modelling was performed by using the same FE model parameters as described earlier. The transmission losses $\alpha_{S0}(f)$ of the analysed symmetric S_0 UGW mode were calculated according to the aforementioned method, taking only the value of transmission losses corresponding to the frequency of f = 400 kHz of the excitation signal. The dependency of transmission losses $\alpha_{S0}(f)$ on the width of the overlap zone Δl in the differently-oriented welded lap joint connection (bottom-top wave transmission) is presented in Fig. 2.2.5.

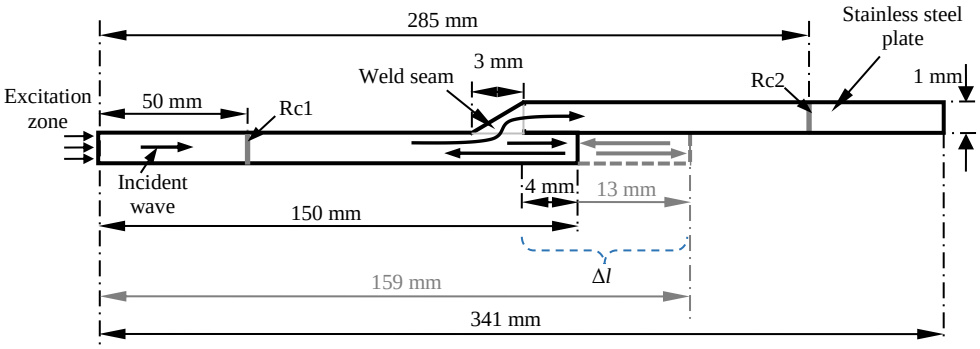

Fig. 2.2.4. The model used for the investigation of the S_0 UGW mode transmission through lap welded plates of different width Δl lap welded plates when joint is oriented in opposite directions with respect to wave propagation direction

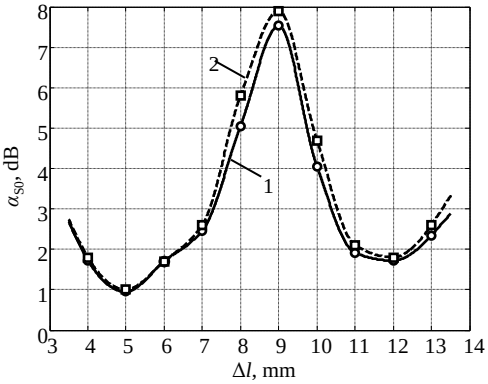

Fig. 2.2.5. The transmission losses $\alpha_{S0}(f)$ of the S_0 UGW mode of different lap joint overlap width Δl: 1 – top-bottom plate wave transmission direction, 2 – bottom-top plate wave transmission direction (dots – FE analysis results, solid and dashed lines – interpolated by a piecewise cubic Hermite polynomial)

The modelling demonstrated that transmission losses $\alpha_{S0}(f)$ of the symmetric S_0 UGW possess the same characteristic independently from lap joint orientation with respect to wave propagation direction. It was observed that the highest transmission losses are of 9 mm plates overlap zone width Δl and are equal to 7.9 dB/weld. The dependency demonstrates that the overall transmission losses $\alpha_{S0}(f)$ of the S_0 wave mode transmitted through the welded lap joint are expected to be up to 15% higher in the bottom-top plate wave transmission direction.

In order to determine how the transmission losses $\alpha_{S0}(f)$ of the symmetric S_0 wave mode for a particular width of the lap joint overlap zone Δl depend on the variation of excitation signal frequency, numerical modelling was carried out by using a model of lap joint connection presented in Fig. 2.2.1. The frequency of the excitation signal (5 periods of 400 kHz sine-burst with Gaussian envelope) was changed in the frequency range from 150 kHz to 500 kHz with the step of 25 kHz. The dependencies of transmission losses $\alpha_{S0}(f)$ of different excitation frequency and different widths

of the overlap zone (Δl = 4 mm, Δl = 9 mm, Δl = 13 mm) taking only the value of transmission losses corresponding to the centre frequency of excitation signal are presented in Fig. 2.2.6.

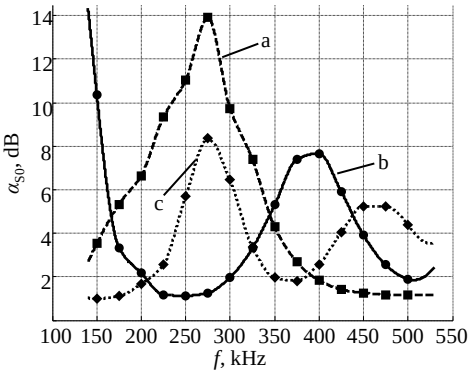

Fig. 2.2.6. Transmission losses $\alpha_{S0}(f)$ of the S_0 wave mode for different excitation signal frequencies of a – 4 mm overlap, b – 9 mm overlap and c – 13 mm lap joint overlap widths (dots – FE analysis results, solid and dashed lines – interpolated by piecewise cubic Hermite polynomial)

The results demonstrate that there are some regular changes of the maxima and minima in the dependency of transmission losses $\alpha_{S0}(f)$ versus excitation frequency. The dependency of transmission losses versus excitation frequency is different for different widths of the overlap zone. It can be assumed that the superposition of direct waves and the waves reflected by the free end of the lap joint of S_0 wave mode signals takes place and, hence, depending on the total width of the lap joint Δl, leads to a larger or smaller amplitude of the resultant wave. In the case of single-edge closed reflector, the maxima and minima appear at every integer number of ¼λ per lap joint width (Fig. 2.2.7a). Thus, it can be stated that the increase of transmission losses $\alpha_{S0}(f)$ of symmetric S_0 UGW mode transmitted through the lap joint is expected at every odd number of ¼λ per lap joint width. Meanwhile, the reduction of the transmission losses could be observed on the even number of ¼λ per lap joint width. This regularity can be expressed with:

$$\begin{aligned} \alpha_{S0}(f,\Delta l) &= \max\left(\frac{n\cdot c_{gr}}{4f}\right),\ n=1,3,5,\ldots, \\ \alpha_{S0}(f,\Delta l) &= \min\left(\frac{n\cdot c_{gr}}{4f}\right),\ n=2,4,6,\ldots. \end{aligned} \tag{2.2.1}$$

A graphical representation of the maxima and minima of transmission losses $\alpha_{S0}(f)$ versus the frequency and lap joint width Δl are presented in Fig. 2.2.7b.

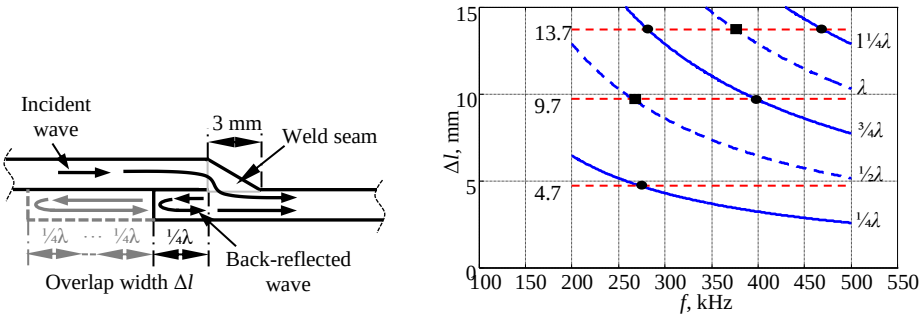

a) b)

Fig. 2.2.7. Wave propagation and reflection in the lap joint connection (a) and dependence of the transmission losses local maxima and minima on the wavelength for a particular lap joint width (square – local minima, dots – local maxima of the transmission losses) (b)

The numerical investigation of the UGW propagation through the single lap joint welded connection demonstrated that the overall transmission losses $\alpha_{S0}(f)$ of the symmetric S_0 wave mode are strongly dependent on the selected system parameters, such as the width of lap joint Δl and operation frequency. Thus, it was observed that, depending on the wavelength per lap joint width, the increase (related to the odd number of ¼λ) or the reduction (related to the even number of ¼λ) of the transmission losses could be observed. Such relationship could be clearly observed in Fig. 2.2.6, where, depending on the wavelength of the incident wave and overlap zone width, additional transmission losses maxima and minima for the S_0 mode transmitted through lap joint connection occurs.

2.3 The influence of bonding state between lap joint on the guided wave propagation

As it was demonstrated by previous investigations, the dispersive behaviour of UGW is strongly dependent on the bonding state between lap joint connected objects [147–153]. Thus, the velocity and amplitude of the UGW signals transmitted through lap joint are among the main parameters to be affected [150, 152, 154]. Typically, in adhesive bonding, the elastic waves are transmitted through the adhesive layer in the overlap region where the adhesive serves as a medium for wave transmission and the overall efficiency of the transmission is mostly affected by the width of the lap joint area and adhesive layer parameters by itself. Differently from adhesively bonded lap joints, the lap joints produced in a storage tank floor construction are commonly connected only by the weld seam. The overlap zone which in the original state does not possess acoustic coupling between the upper and lower plates, leads to partial cohesion of the plates in the overlap zone during the long years of tank exploitation (usually the design life of an AST is 25 years, but in practice, the tanks may be in use for even 50–70 years). The physical factor leading to it can be the pressure of the filled tank, moisture retention in the lap and corrosion. The example of a typical welded lap joint connection view of the storage tank floor edge in service is presented in Fig. 2.3.1. How such phenomena are affecting the transmission losses $\alpha_{S0}(f)$ of the selected symmetric S_0 UGW mode was the task of the presented investigation.

Fig. 2.3.1. Lap joint condition in a real storage tank floor during service and operation period

The main purpose of numerical investigation is to determine how the bonding condition between lap joint of the welded plates affects the transmission losses $\alpha_{S0}(f)$ of the symmetric S_0 UGW mode. To achieve this goal, three instances of the UGW propagation through the lap joint welded plates were analysed by using the scheme presented in the Fig. 2.3.2a:

a) plates are connected only at the weld seam position (Fig. 2.3.2b);
b) partially bonded plates (50% cohesion) (Fig. 2.3.2c);
c) fully bonded plates (100% cohesion) (Fig. 2.3.2d).

It should be noted that the model is presented on the different vertical and horizontal scales.

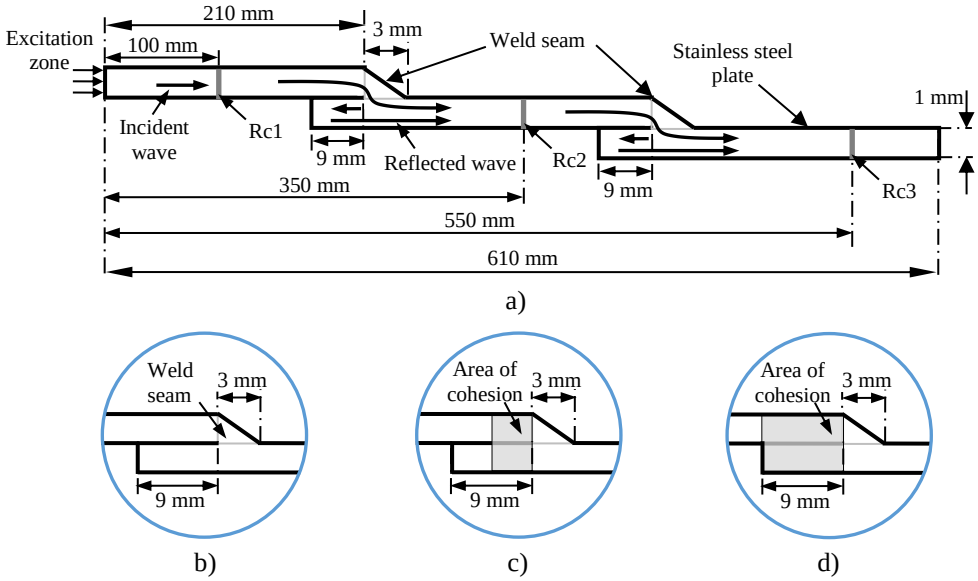

Fig. 2.3.2. a) the model used for the investigation of the symmetric S_0 wave mode propagation through the welded lap joints (a) when: plates are connected only at the weld seam position(b), partially bonded plates (c) and fully bonded plates (d)

The investigation of the symmetric S_0 UGW mode propagation through the lap joint welded plates was carried out by applying 5 periods of 400 kHz sine-burst with a Gaussian envelope signal, which was earlier described in Section 2.1 and presented in Fig. 2.1.3, to the edge of the model. The concentrated and uniformly distributed excitation force was applied in the longitudinal direction. The properties of the

material used were the same as presented in Table 2.1. Four-node PLANE42 linear elements were used to represent a two-dimensional section of the object and plane strain condition assumed to be present. The finite element size was selected to be 0.1 mm so that there were at least 10 elements per the thickness of the plate. The time domain discretization step was selected to be dt = 10 ns. The time interval used for the modelling of elastic wave propagation was $\Delta t = 0 \div 200$ μs. During the modelling, it was assumed that due to the cohesion of the plates in overlap region, there is solid contact. With such contact present, it was assumed that the contact layer between plates has the properties of stainless steel, which means that the contact allows the propagation of both – normal and tangential components of the waves in the overlap region.

In order to estimate the transmission losses $\alpha_{S0}(f)$ of the symmetric S_0 UGW mode transmitted through single and multiple welds, three areas of interest were chosen. The waveforms of the longitudinal particle velocity component were obtained by placing virtual receivers at Rc1 – 150 mm, Rc2 – 350 mm and Rc3 – 550 mm distances from the applied excitation zone, which corresponds to the positions before a lap joint, after the first and the second lap joints, respectively. The distances were selected to ensure that the analysed ultrasonic symmetric S_0 guided wave mode separates in time from the other newly-generated and back-reflected modes as far as possible. The mean value of the longitudinal particle velocity across the plate thickness and transmission losses $\alpha_{S0}(f)$ of the analysed symmetric S_0 guided wave mode were calculated by using equations 2.1.8 and 2.1.11. The acquired waveforms of the mean value of the longitudinal particle velocity, the spectra of the analysed symmetric S_0 wave mode selected from the time diagrams of the received signals by using the Hanning window and the losses of transmission $\alpha_{S0}(f)$ as it passes through the lap joint welded plates on different bonding state condition between plates are presented in Fig. 2.3.3–Fig. 2.3.8, respectively. The values of transmission losses $\alpha_{S0}(f)$ of the symmetric S_0 UGW mode as it passes through the lap joint connection at the frequency of 400 kHz excitation signal for the different bonding state conditions between stainless steel plates are presented in Table 2.3.1.

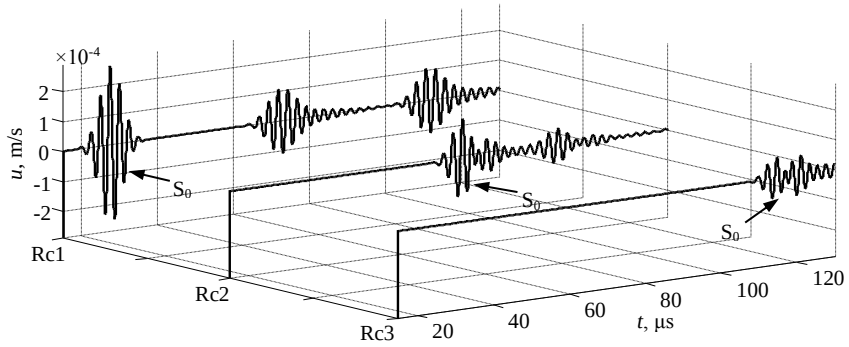

Fig. 2.3.3. Waveforms of the obtained signals in plates connected only at weld seam position picked up by receiver Rc1 – before the lap joint, Rc2 – after the 1st lap joint and Rc3 – after the 2nd lap joint connection, respectively

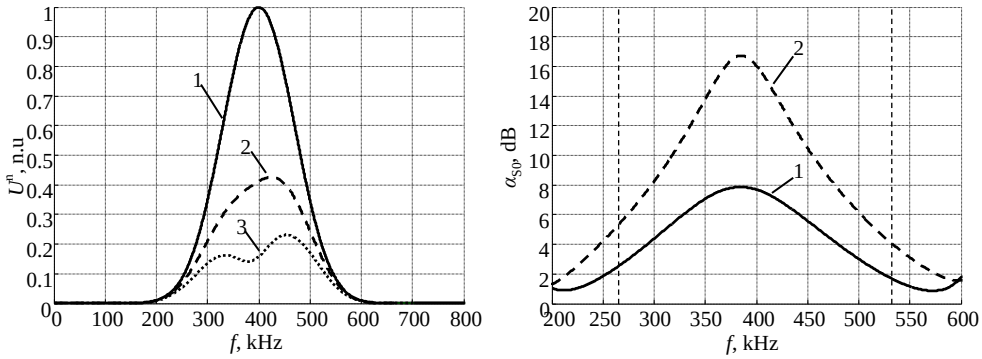

a) b)

Fig. 2.3.4. The spectra of the S_0 UGW mode: 1 – before the lap joint, 2 – after the 1st and 3 – after the 2nd lap joint, respectively (a) and the transmission losses $\alpha_{S0}(f)$ of the S_0 wave mode after 1 – the 1st and 2 – the 2nd lap joint in plates connected only at the weld seam position (b)

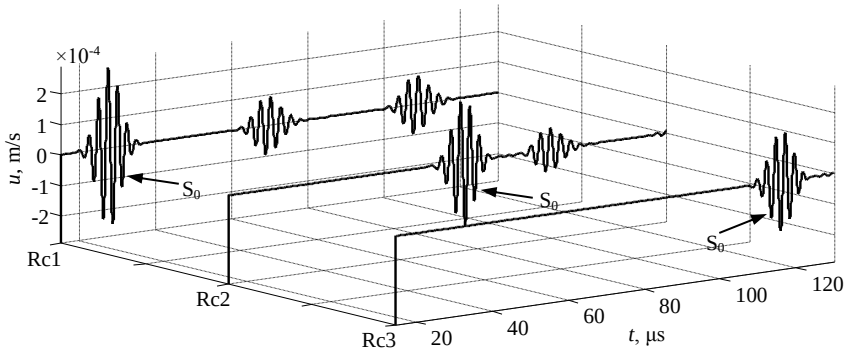

Fig. 2.3.5. Waveforms of the obtained signals in the partially bonded (50% cohesion) lap joint between plates picked up by receiver Rc1 – before the lap joint, Rc2 – after the 1st lap joint and Rc3 – after the 2nd lap joint, respectively

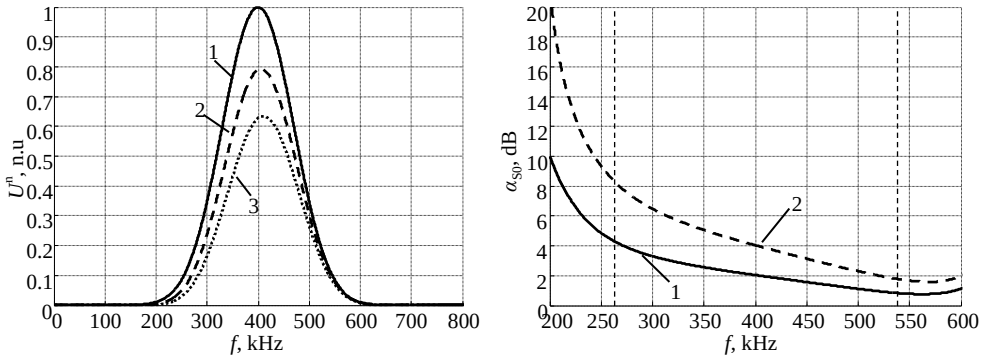

a) b)

Fig. 2.3.6. The spectra of the S_0 UGW mode: 1 – before the lap joint, 2 – after the 1st and 3 – after the 2nd joint, respectively (a) and the transmission losses $\alpha_{S0}(f)$ of the S_0 wave mode after 1 – the 1st lap joint and 2 – the 2nd lap joint in the partially bonded (50% cohesion) lap joint (b)

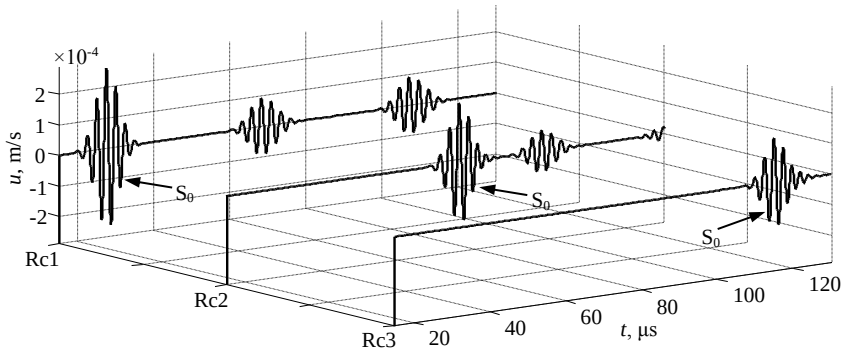

Fig. 2.3.7. Waveforms of the obtained signals in the fully bonded (100% cohesion) lap joint between plates picked up by receiver Rc1 – before the lap joint, Rc2 – after the 1st lap joint and Rc3 – after the 2nd lap joint, respectively

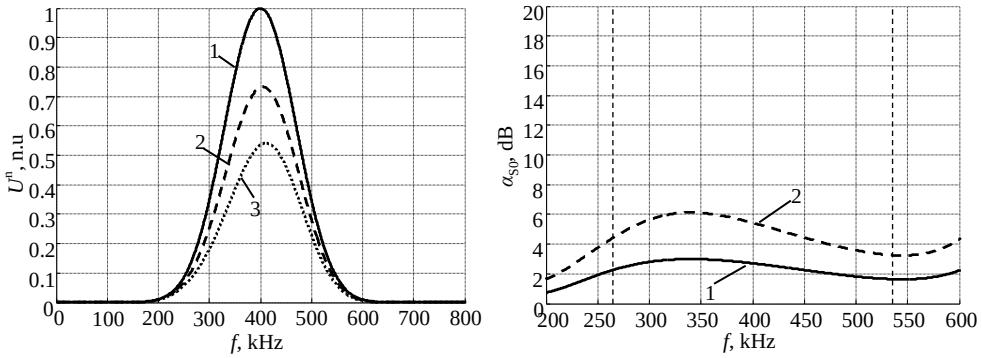

a) b)

Fig. 2.3.8. The spectra of the S_0 UGW mode: 1 – before the lap joint, 2 – after the 1st and 3 – after the 2nd lap joint, respectively (a) and the transmission losses $\alpha_{S0}(f)$ of the S_0 wave mode after 1 – the 1st and 2 – the 2nd lap joint in the fully bonded (100% cohesion) lap joint (b)

Table 2.3.1 Transmission losses $\alpha_{S0}(f)$ of the symmetric S_0 UGW mode on different lap joint conditions

	Case of inspect	α_{S0_1}, dB	α_{S0_2}, dB
1.	Plates connected at weld seam position	7.7	16.1
2.	Partially bonded plates	2.1	4.1
3.	Fully bonded plates	2.7	5.4

The carried out numerical investigation demonstrated that the highest transmission losses $\alpha_{S0}(f)$ of the analysed symmetric S_0 UGW mode are obtained when the plates are connected only by the weld seam in the lap joint. The predicted average value of transmission losses $\alpha_{S0}(f)$ of the S_0 mode transmitted through a welded lap joint at 400 kHz frequency was estimated to be 8.05 dB/weld. Meanwhile, in the partially and fully bonded lap joints, the transmission losses of the S_0 wave

mode were obtained to be 2.05 dB/weld and 2.7 dB/weld, respectively. Such decrease of transmission losses $\alpha_{S0}(f)$ for the analysed symmetric S_0 guided wave mode in the partially and fully bonded lap joints may be explained by the fact that cohesion changes the width area in the connection zone between lap joint welded plates and the UGW are transmitted more efficiently from one plate to another. In general, the numerical modelling demonstrated that the average value of transmission losses of S_0 UGW mode is at the level of 8 dB/weld; additionally, these losses strongly depend on the cohesion between plates. By considering that there can be tens of welds across the tank floor, the total transmission losses may exceed 100 dB. However, concerning possible cohesion of plates the losses are expected to be much lower in the overlap region, during long-term exploitation of the storage tank.

2.4 The influence of load on the ultrasonic guided wave propagation

The propagation of UGW in an AST is much more complicated from the point of view of NDT and SHM not only because of multiple joints but also because of liquid boundary interaction between the object and the surrounding medium which affects the behaviour of the guided wave propagation. Whenever UGW are propagating in objects that are in a vacuum, the energy of the system under investigation remains constant if all of the materials are elastic and there are no leakage losses to the environment. However, if the object is immersed or loaded by another acoustical material, the energy can leak into the surrounding material and be lost. This directly affects the amplitude of the propagating UGW signals and have a significant impact on further propagation of some of the modes. In this section, a storage tank which contains liquid is studied in order to estimate the effect of loading the storage tank floor with another material on UGW propagation. Water and petrol fluid loadings, as well a load of moist sand (which is used as pedestal of the tank) are considered in this study. Although there are differences between the properties of water and oil products, their effects are expected to have low relevance to the overall liquid loading, so they are neglected. Oil products, in particular, may be more viscous than water, which would increase the overall attenuation for propagating UGW modes, but this should be low for typical viscosities of oil products [81,155]. The purpose of modelling was to investigate the UGW propagation in a 2D section of a scaled-down storage tank containing multiple shell-to-bottom and lap joint connections in order to assess the expected transmission losses $\alpha_{S0}(f)$ of the symmetric S_0 UGW mode on different loading conditions.

In order to investigate the effects of the UGW propagation through multiple shell-to-bottom and lap joint connections and its dependence on different loading conditions, numerical simulations were performed by applying the FE analysis method. The acoustical properties of the materials used in FE analysis of the UGW propagation on different loading cases are presented in Table 2.4.1 [25, 156–158].

Table 2.4.1 The acoustical properties of materials used in modelling

Material	Density ρ, kg/m^3	Young's modulus E, GPa	Poisson's ratio ν	Bulk modulus K, GPa
Stainless steel alloy	8,000	193	0.31	–
Water	1,000	–	–	2.2
Petrol	800	–	–	1.07 (1.07–1.49)
Moist sand	1,980	–	–	37

The Abaqus/Explicit finite element software was used to obtain the wave propagation through the 2D geometry of the storage tank on different loading conditions, which includes an explicit algorithm with the central difference time integration method for solving the transient wave propagation. Compared with the implicit integration method, explicit integration method requires less computational effort per time step. However, the explicit integration method can only be conditionally stable and, in principle, is used when the size of the integration time step *dt* needed for accuracy is about the same as the time step limit defined by the stability limit [140, 142, 159, 160].

The investigation of UGW propagation in the 2D section of a scaled-down storage tank was performed for four different loading cases by using the model presented in Fig. 2.4.1:

a) there is no load applied on the storage tank floor (surrounding environment – vacuum);
b) water load is applied on the upper surface of the storage tank floor;
c) petrol load is applied on the upper surface of the storage tank floor;
d) water load is applied on the upper surface and moist sand load applied on the bottom surface of the storage tank floor.

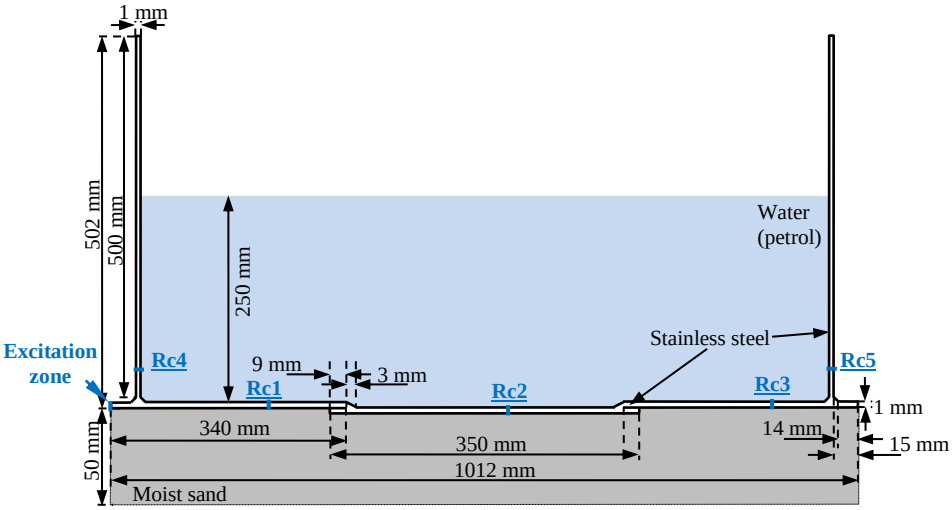

Fig. 2.4.1. The 2D storage tank section used for investigating the load impact on UGW propagation

The solid structure was modelled by using CPE4R – a 4-node bilinear plane strain quadrilateral, reduced integration with hourglass control elements (hourglassing is a numerical phenomenon by which zero energy modes propagate). For modelling of the acoustical medium (in case of wave propagation in an elastic medium – usually a fluid), the 4-node AC2D4R reduced integration with hourglass control acoustic elements were used. The linear bulk viscosity parameter which introduces damping associated with volumetric straining was set to be equal to $q_L = 1$. The liquid boundary interaction between the investigated object and the applied load was defined by using surface-to-surface tie constraint assumption, where the surfaces of the storage tank model were selected as *master* and surfaces of the surrounding medium (water, petrol and moist sand) were selected as a *slave*. Elastic wave propagation in the linear isotropic acoustical materials is described by an equivalent fluid. The speed of sound in such equivalent fluid is described by equation 2.4.1 [161]:

$$c = \sqrt{\frac{K}{\rho}}, \tag{2.4.1}$$

where ρ is the density, K is the bulk modulus.

The size of the finite element was selected according to equation 2.1.6 so that there would be on the order of 20 nodes per wavelength and was equal to 0.2 mm. For the excitation of UGW in the presented 2D storage tank model, 5 periods of 400 kHz sine-burst with a Gaussian envelope signal defined in 2.1 section was used. The concentrated and uniformly distributed surface force was applied to the edge of the storage tank floor in the longitudinal direction. The discretization step in time domain was selected to be $dt = 5$ ns. The time interval used for modelling of wave propagation was $\Delta t = 0 \div 250$ μs.

Modelling of the structural-acoustical problems by the means of the FE analysis method can lead to very large models, which may be prohibitively costly in terms of computational resources. Therefore, in order to reduce the size of the model and prevent multiple reflections occurring at the boundaries of water, petrol and moist sand layers, the non-reflecting boundary condition was used. It assumes that acoustic waves are transmitted across such a boundary with little reflection of energy back into the acoustic medium, and the amount of energy reflected is small if the boundary is far away from major acoustic disturbances.

The symmetric S_0 UGW mode propagating through the storage tank floor was selected by applying the rectangular time variable window whose position changes depending on the distance and group velocity c_{gr} of the wave mode under analysis. The time variable window is defined by equation 2.4.2:

$$h_w\left(t - \frac{x + x_0}{c_{gr}}\right) = \begin{cases} 1, & 0 \le t \le \Delta t_w \\ 0, & \text{other} \end{cases}, \tag{2.4.2}$$

where c_{gr} is the group velocity of the guided wave mode under analysis, x is the distance between the transmitter and the receiver, x_0 is the initial distance between transducers, Δt_w is the width of time variable window. The signals corresponding to the S_0 mode were distinguished by using the time variable window, and a peak-to-

peak amplitude of the symmetric S_0 wave mode was estimated according to equation 2.4.3:

$$U_{\text{p–p}}(x) = \max_t \left[u(t) \cdot h_{\text{w}}(t,x)\right] - \min_t \left[u(t) \cdot h_{\text{w}}(t,x)\right]. \quad (2.4.3)$$

The results of the UGW propagating in the investigated 2D storage tank section in the form of B-scan images with denoted S_0 wave mode, joint positions and relative $U_{\text{p-p}}$ amplitude change of the selected symmetric S_0 wave mode depending on applied load, within the boundaries of the time variable window, are presented in Fig.2. 4.2–Fig. 2.4.5. In general, the B-scan images presented in Fig. 2.4.2a–Fig. 2.4.5a reveal that the applied loading has the most significant impact on the asymmetric A_0 guided wave mode propagation. As a result of liquid boundary interaction between the investigated object and the surrounding medium, and the dominance of the out-of-plane u_y displacement component in A_0 wave mode motion, large energy leakage to the surrounding medium occurs. As a consequence of high leakage losses caused by the applied load, the asymmetric A_0 wave mode is strongly suppressed and propagates only short distances in the fluid-loaded storage tank. Meanwhile, the influence of the applied loading on the amplitude of the transmitted guided wave for the symmetric S_0 UGW mode is less noticeable because the dominant component of particle displacement for this wave mode is the in-plane u_x and mostly a shearing motion at the liquid-plate contact. Thus, the energy leakage losses to the surrounding medium for the symmetric S_0 UGW mode are mainly caused by out-of-plane u_y displacement component which is considered to be small at the liquid-plate contact and results in lower wave energy losses. As graphs of the propagating symmetric S_0 wave mode along the storage tank floor presented in Fig. 2.4.2–Fig. 2.4.5 show, the reduction of the S_0 wave mode $U_{\text{p-p}}$ amplitude is mainly caused by the shell-to-bottom and welded lap joint connections in the direct wave propagation path. Moreover, wave scattering, mode conversion, which leads to newly-generated modes, and energy dissipation takes place.

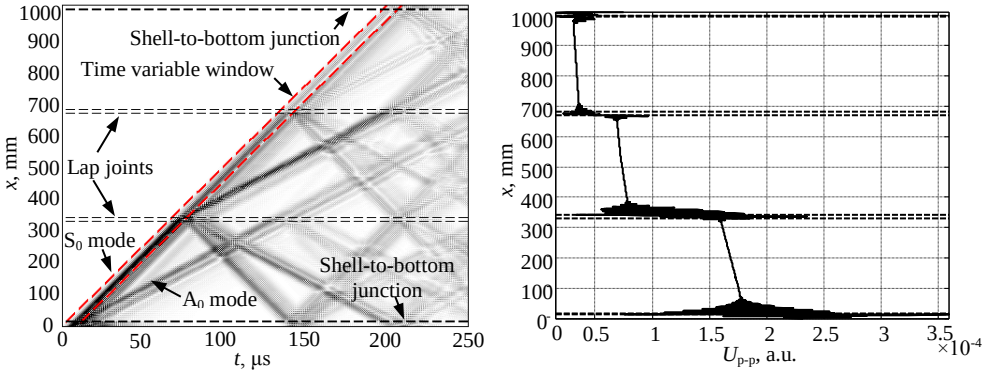

Fig. 2.4.2. B-scan image of the waves propagating along the floor of the AST (a), $U_{\text{p-p}}$ amplitude change of the S_0 wave mode when there is no load applied on the tank floor (b)

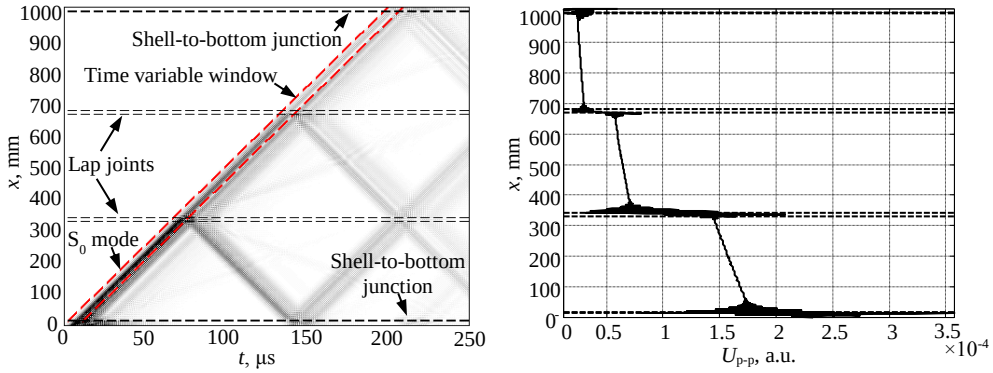

Fig. 2.4.3. B-scan image of the waves propagating along the floor of the AST (a), $U_{p\text{-}p}$ amplitude change of the S_0 wave mode when a water load is applied on the upper surface of the tank floor (b)

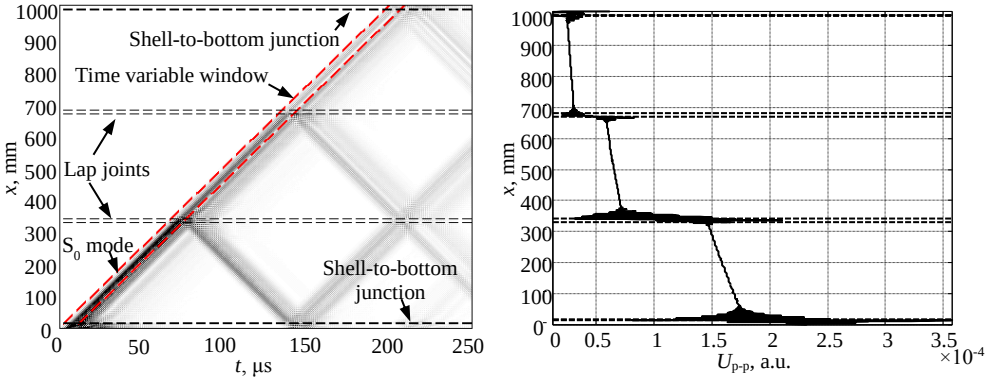

Fig. 2.4.4. B-scan image of the waves propagating along the floor of the AST (a), $U_{p\text{-}p}$ amplitude change of the S_0 wave mode when a petrol load is applied on the upper surface of the tank floor (b)

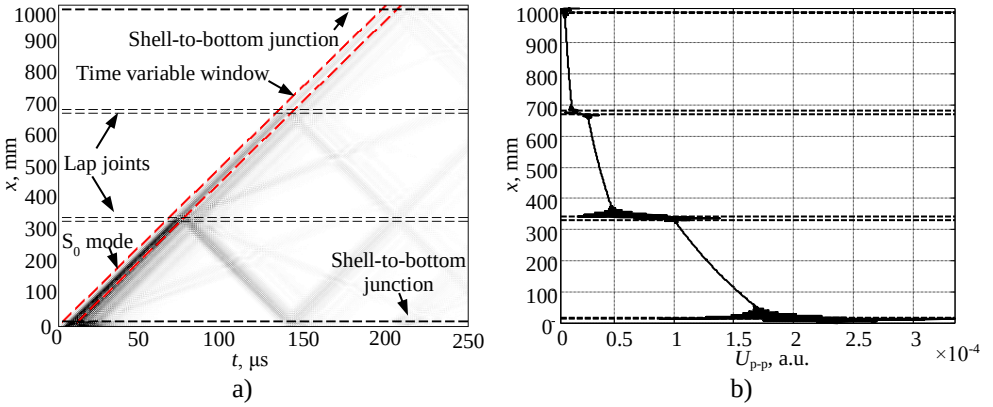

Fig. 2.4.5. B-scan image of the waves propagating along the floor of the AST (a), $U_{p\text{-}p}$ amplitude change of the S_0 wave mode when a water load is applied on the upper surface and the moist sand load is applied on the bottom surface of the tank floor (b)

In order to assess the attenuation caused by material damping and wave energy leakage into surrounding environment, the compensation of the S_0 wave mode amplitude due to wave interaction with shell-to-bottom and lap joint connections, in the ranges of X_1, X_2, X_3 of the storage tank floor was performed by using optimization of several variables:

$$U_{\text{p–p}}(x, A_1, A_2, A_3, \alpha_e) = \begin{cases} A_1 e^{-\alpha x}, & x \in X_1; \\ A_1 A_2 e^{-\alpha x}, & x \in X_2; \\ A_1 A_2 A_3 e^{-\alpha x}, & x \in X_3. \end{cases} \tag{2.4.4}$$

$$X_1 = [80:315],\ X_2 = [395:645],\ X_3 = [725:960];$$

$$U_{\text{p–p}}(x, A_1', A_2', A_3', \alpha_e') = \arg\left\{ \min_{A_1, A_2, A_3, \alpha_e} \sum_{x \in [X_1, X_2, X_3]} \left(U_{\text{p–p}}(x, A_1, A_2, A_3, \alpha_e) - U_{\text{p–p},ex}(x) \right) \right\}. \tag{2.4.5}$$

where x is the distance the wave has travelled from the initial location, A_1, A_2, A_3 are the unattenuated amplitudes of the propagating wave at some location, α is the attenuation coefficient of wave traveling in the x direction.

The compensated decay of the amplitude of the symmetric S_0 UGW mode on the different loading conditions and the overall attenuation are presented in Fig. 2.4.6. The results reveal that the attenuation caused upon damping in the stainless steel is $\alpha_{ss} = 3.6$ dB/m. Meanwhile, the additional decay of the S_0 wave mode is caused by wave energy leakage into the surrounding environment. The numerical modelling shows that the approximate wave leakage losses in water are $\alpha_{wt} = 2.2$ dB/m, in petrol – $\alpha_p = 1.9$ dB/m, and in moist sand and water load – $\alpha_{ws} = 12.3$ dB/m.

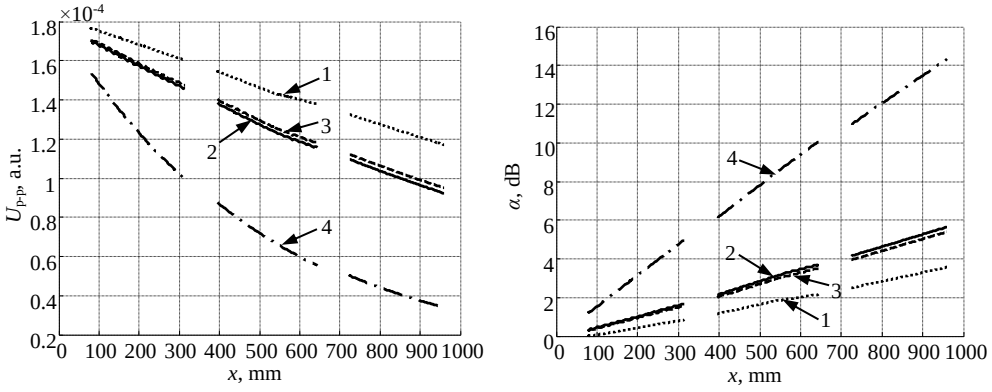

a) b)

Fig. 2.4.6. Amplitude change of the S_0 wave mode for the different loading cases (a); the dependence of overall attenuation into the environment on the distance in the cases when: 1 – no load applied, 2 – water load, 3 – petrol load, 4 – water and moist sand loads (b)

The expected transmission losses $\alpha_{S0}(f)$ of the symmetric S_0 UGW mode for different tank loading cases after shell-to-bottom and lap joint connections were

estimated by selecting sets of nodes at discrete positions on the storage tank. The set of nodes for gathering the propagating symmetric S_0 wave mode were selected at Rc1 – 240 mm, Rc2 – 570 mm, Rc3 – 895 mm away from the excitation zone and corresponding to the positions before, after the first and the second lap joint connections, respectively. In addition, the sets of nodes on the wall of the 2D storage tank model at position Rc4 and Rc5 were selected at 70 mm height in order to assess the expected transmission losses of the S_0 wave mode as it passes the entire tank floor and is induced into its shell (wall). The mean value of the longitudinal particle velocity of the symmetric S_0 wave mode over the thickness at the selected positions and its transmission losses were calculated by using equations 2.1.8 and 2.1.11. The spectra and transmission losses $\alpha_{S0}(f)$ of the analysed symmetric S_0 wave mode for different load cases were calculated from the spectra ratio of the S_0 mode signals and are presented in Fig. 2.4.7 and Fig. 2.4.8, respectively. Furthermore, the obtained transmission losses $\alpha_{S0}(f)$ of the propagating S_0 wave mode as it passes through multiple connections and in different load conditions at the central frequency of the excitation signal are presented in Table 2.4.2.

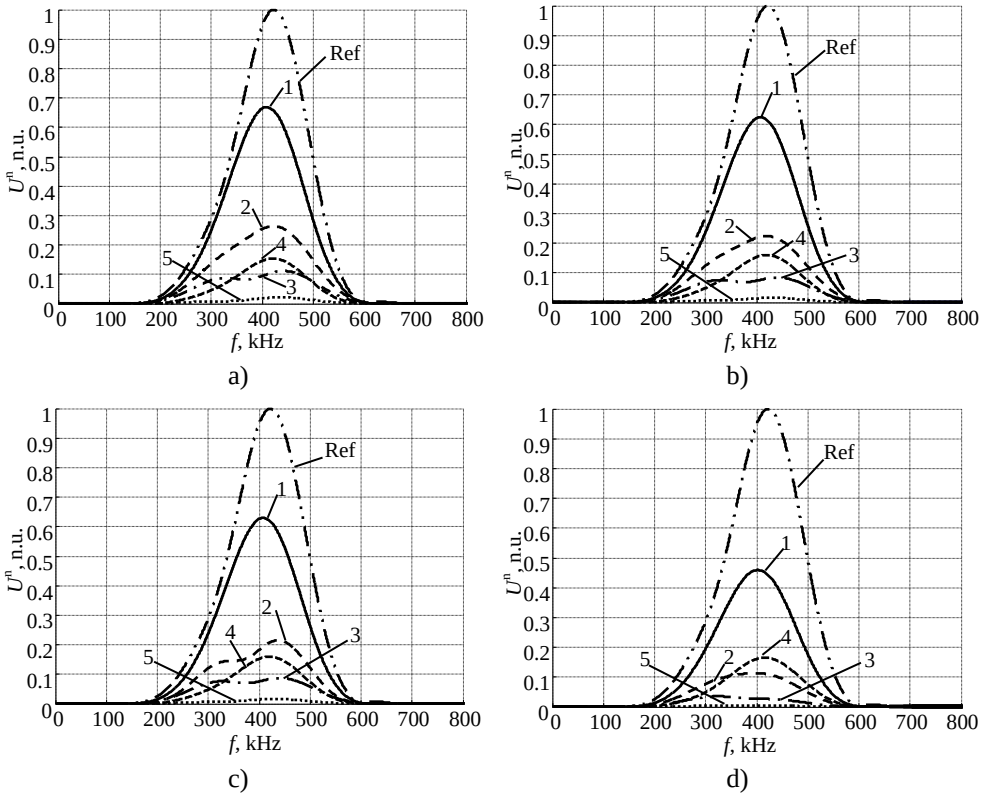

Fig. 2.4.7. The spectra of the S_0 UGW mode in the case of no load (a), a water load (b), a petrol load (c), water and moist sand loads (d) applied at Ref – excitation zone, 1 – before lap joint, 2 – after the 1st lap joint, 3 – after the 2nd lap joint, 4 – on the 1st vertical wall, 5 – on the 2nd vertical wall

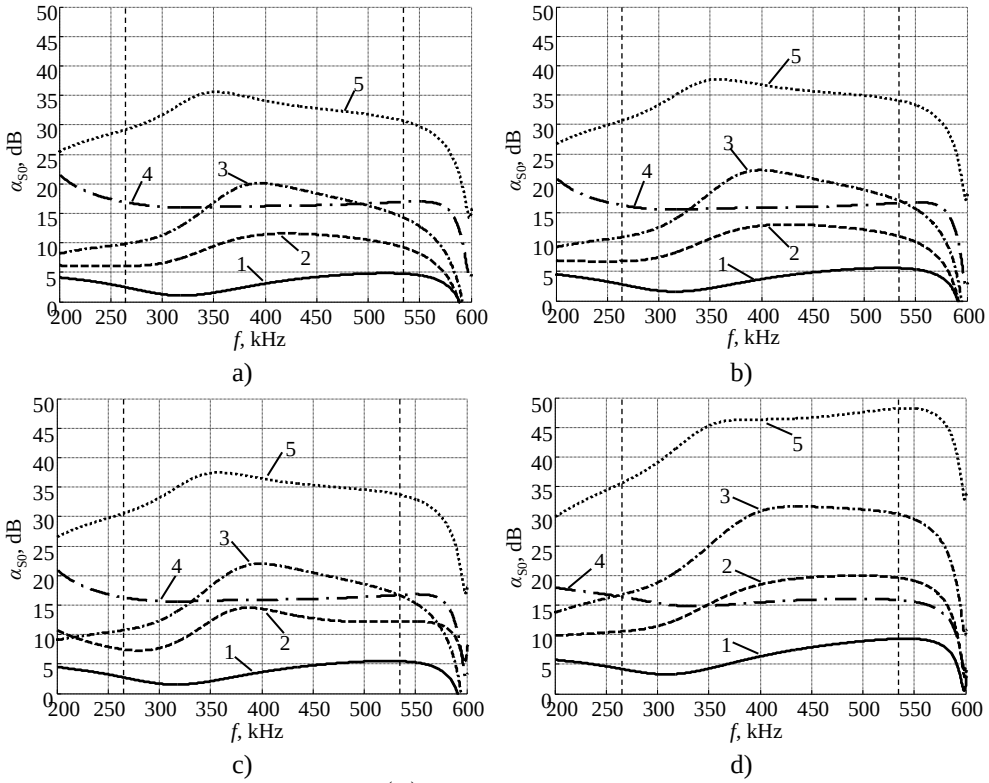

Fig. 2.4.8. Transmission losses $\alpha_{S0}(f)$ of the S_0 UGW mode across a section of the scaled-down AST in the case of no load (a), a water load (b), a petrol load (c) and water and moist sand loads (d) applied at 1 – before lap joint, 2 – after the 1st lap joint, 3 – after the 2nd lap joint, 4 – on the 1st wall, 5 – on the 2nd wall

Table 2.4.2 Transmission losses $\alpha_{S0}(f)$ of the symmetric S_0 UGW mode for different load conditions

Virtual receiver position	No load applied	Water load	Petrol load	Water and moist sand loads
Before lap joint	3.1 dB	3.7 dB	3.6 dB	6.3 dB
After the 1st lap joint	11.4 dB	12.8 dB	14.4 dB	18.4 dB
After the 2nd lap joint	20.1 dB	22.2 dB	22.2 dB	30.8 dB
1st vertical wall	16.2 dB	15.8 dB	15.9 dB	15.4 dB
2nd vertical wall	34.1 dB	36.7 dB	36.5 dB	46.3 dB

The result of this research show that the overall transmission losses $\alpha_{S0}(f)$ of the analysed symmetric S_0 guided wave mode increase due to liquid boundary interaction between the storage tank and the surrounding medium. As Table 2.4.2 demonstrates, the loadings of water and petrol have shown a similar effect on UGW transmission losses and further propagation of S_0 wave mode in the presented storage tank model. However, the oil products may be more viscous than water which would result in an increase of attenuation for this wave mode. Furthermore, the overall

increase of attenuation of UGW would be affected by the sludge on the tank floor which was not considered in the modelling. Meanwhile, the highest overall transmission losses $\alpha_{S0}(f)$ of the symmetric S_0 guided wave mode were obtained in the case of water and moist sand loads. The obtained transmission losses are mainly caused by the leakage of wave energy into the moist sand environment.

2.5 3D modelling of ultrasonic guided wave propagation in a storage tank

The plane strain assumption inherently used for the 2D modelling of elastic wave propagation implies that UGW are not geometrically attenuated and dissipated as they propagate. However, the propagation of UGW in the scaled-down AST and its floor is much more complicated than it was presented and analysed in the 2D modelling approach because of the shell-to-bottom junction, multiple lap joint connections, occurring mode conversion, wave scattering, energy dissipation and multiple reflections in the structure. The main advantage of 3D models is that they can capture almost all aspects of wave propagation behaviour, such as the waveform, reflections of boundaries or damage, or any other wave interactions. However, they require more time and computational resources and can lead to a large amount of data.

The main purpose of 3D modelling is to predict the complexity of UGW propagation in the scaled-down storage tank (Fig. 2.5.1) and to investigate the possibilities to perform measurements on the tank wall (shell) for gathering the required projection information needed for tomographic reconstruction of the storage tank floor. In order to achieve the aim, the following tasks should be investigated:

- is it possible to observe signals transmitted through the tank floor on the opposite side of the storage tank;
- how do the transmission losses of the UGW depend on the angle of wave propagation;
- at what angle the projections could be measured and are the UGW coming in the shorter way.

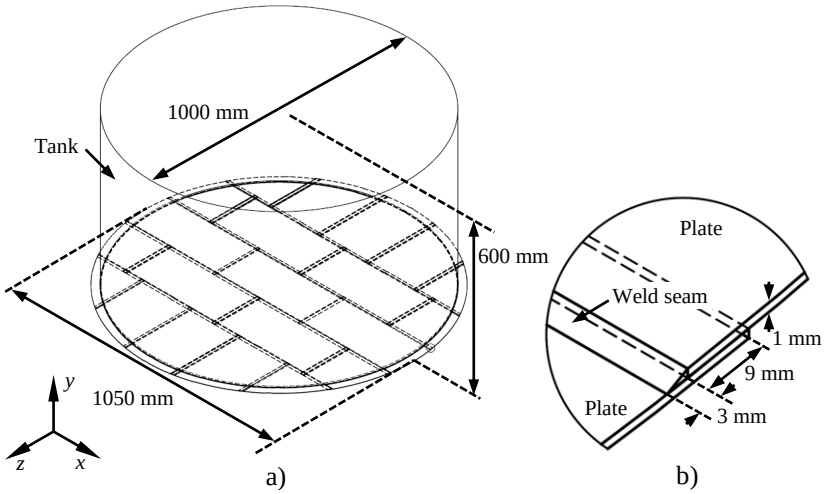

Fig. 2.5.1. A 3D model of the scaled-down storage tank (a), view of lap joint connection between plates used in the model (b)

For the simulation of the UGW propagation in a scaled-down 3D storage tank model, an explicit dynamic analysis using Abaqus/Explicit finite element package was performed. In order to reduce the size of the model and the computational time needed for the modelling of elastic wave propagation in a scaled-down 3D storage tank, the size of the finite element l_e was set to 0.5 mm. This satisfies the aforementioned equation 2.1.6 for good spatial resolution requirement in FE modelling only for the symmetric S_0 wave mode propagation, since the number of elements per wavelength for S_0 wave mode is $n_{S_0} = 25$, while for asymmetric A_0 wave mode – $n_{A_0} = 8$. For the 3D modelling of the storage tank floor consisting of multiple plates joined together by lap joint connections, a C3D8R standard Abaqus linear brick elements with reduced integration and hourglass control were used. For the modelling of the cylindrical part, C4R general purpose linear 4-sided shell elements were used, which correspond to the shell (wall) of the tank. The total number of elements in the presented model – 15,965,683 (C3D8R – 7,843,057, C4R – 8122,626).

Separate plates in the scaled-down storage tank floor model were connected to each other only at the weld seam positions by using surface-to-surface tie constraint assumption which generally avoids stress noise at tied interfaces. Typically, a tie constraint is defined at the interface at two zones to stitch the two meshes together. The excitation of the UGW into the presented 3D storage tank model was performed by adding a concentrated and uniformly distributed excitation force of 5 periods of 400 kHz sine-burst with a Gaussian envelope signal to the wall of the tank, 10 mm above its floor (in respect of the central plate of tank floor). The area of excitation zone is 9×9 mm. The discretization step in the time domain is dt = 12.5 ns. The time interval used for the modelling of wave propagation was set to be Δt = 250 μs.

Three cases of UGW propagation at different transmitter positions for the excitation of the arc of the storage tank wall were investigated. The transmitter position on the storage tank wall was defined according to the following expressions:

$$\begin{aligned} x_{\mathrm{Tr},n} &= R_{\mathrm{T}} \cos\left(\varphi_{\mathrm{Tr},n} - \pi/2\right), \\ y_{\mathrm{Tr},n} &= R_{\mathrm{T}} \sin\left(\varphi_{\mathrm{Tr},n} - \pi/2\right), \end{aligned} \tag{2.5.1}$$

where $x_{\mathrm{Tr},n}$, $y_{\mathrm{Tr},n}$ are the coordinates of the transmitters, $n = 1 \div N_{\mathrm{Tr}}$, where N_{Tr} is the number of transmitters, R_{T} is the radius of the tank shell, $\varphi_{\mathrm{Tr},n}$ is the transmitter angle. The modelling of wave propagation in the scaled-down 3D storage tank model was performed when the transmitters were located at $\varphi_{\mathrm{Tr},1} = 270^{\circ}$, $\varphi_{\mathrm{Tr},2} = 228.75^{\circ}$ and $\varphi_{\mathrm{Tr},3} = 187.5^{\circ}$. A graphical representation of the transmitters arrangement on the tank wall is presented in Fig. 2.5.2.

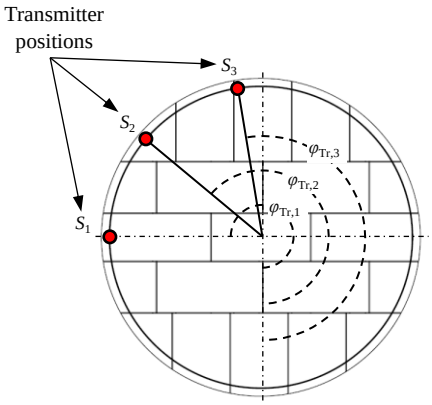

Fig. 2.5.2. The analysed cases of UGW propagation in a 3D storage tank model for different transmitter positions

The results of UGW propagation in the scaled-down 3D storage tank model for different transmitter positions and at different time instances are presented in Fig. 2.5.3–Fig. 2.5.5, respectively.

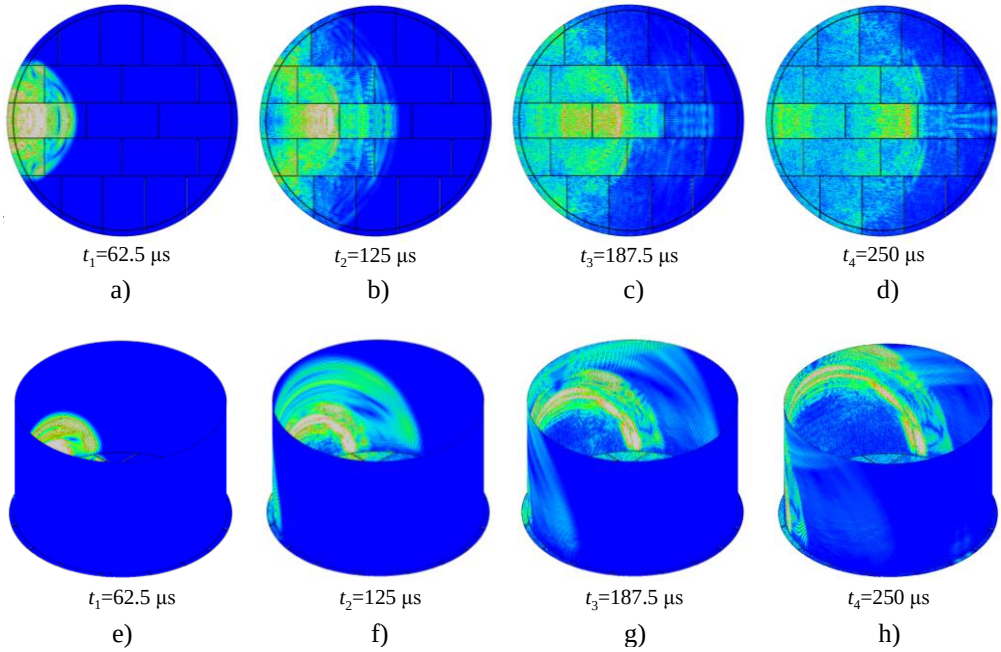

Fig. 2.5.3. A visualisation of UGW propagation in the scaled-down 3D storage tank model at different time instances when the transmitter is located at $\varphi_{Tr,1}$ = 270º

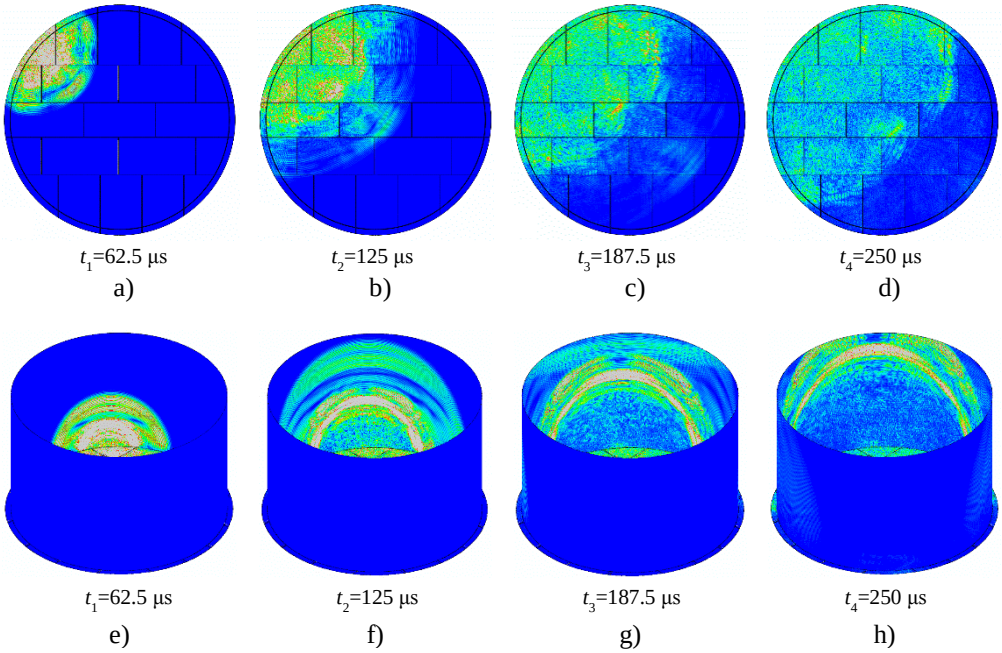

Fig. 2.5.4. A visualisation of UGW propagation in the scaled-down 3D storage tank model at different time instances when the transmitter is located at $\varphi_{Tr,2}$ = 228.75º

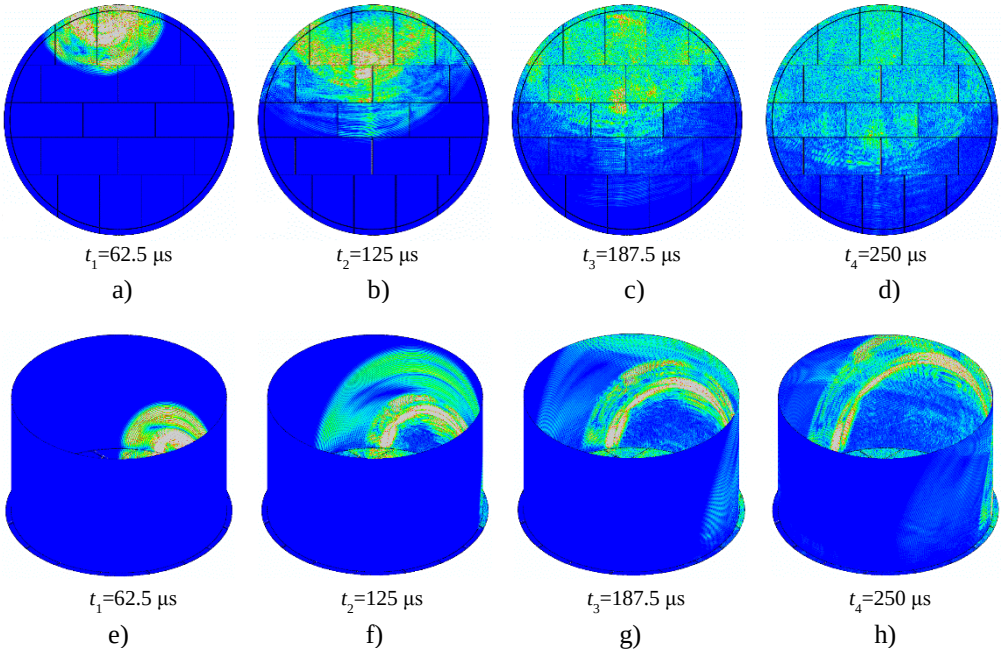

Fig. 2.5.5. A visualisation of UGW propagation in the scaled-down 3D storage tank model at different time instances when the transmitter is located at $\varphi_{Tr,3}$ = 187.5º

The amplitude modulus of the particle velocity distribution for different transmitter positions on the storage tank wall and at different time instances in *x*0*z* plane are presented in Fig. 2.5.3 (a, b, c, d), Fig. 2.5.4 (a, b, c, d) and Fig. 2.5.5 (a, b, c, d), respectively. The particle velocity distribution in the investigated storage tank model in *xyz* coordinate system at different time instances are presented in Fig. 2.5.3 (e, f, g, h), Fig. 2.5.4 (e, f, g, h) and Fig. 2.5.5 (e, f, g, h), respectively. By analysing the figures, the complexity of propagating UGW in the scaled-down storage tank can be observed. In general, it can be observed that the generated UGW in the presented structure spread in the radial direction in the wall, as well as into the floor of the storage tank. This is due to the fact that the size of the selected excitation zone with applied concentrated force is much smaller compared to the dimensions of a storage tank, and it becomes comparable to the point source having a wide directivity pattern. In contrast to transducers usually used in NDT, where a very narrow beam is essential for good lateral resolution, in ultrasonic tomography it is necessary that an as large as possible region is insonified with one transducer so that any objects in the cross-section of the beam are "illuminated" and their reflections are received by any of the other surrounding sensors. As it is indicated by the wave propagation visualisation in *x*0*z* plane which shows UGW propagation in the floor of the scaled-down storage tank, the change of the amplitude of the signal caused mainly by the geometrical complexity of the structure can be observed. As a result, a high level of scattering, leading to the complicated transmission, reflection, diffraction and mode conversion phenomena takes place, thus causing newly-converted modes and energy dissipation resulting in complicated transmission of the symmetric S_0 UGW mode over the storage tank floor constructed of multiple plates joined together by lap joint welds. It could also be stated that the signals of the symmetric S_0 wave mode with the highest amplitude transmitted through the storage tank floor could be observed only at the wave propagation path with a lesser number of welds.

The tomographic reconstruction algorithms in the first step require obtaining projections which in transmission tomography is done by using the amplitude of signals transmitted through the tank for the estimation of attenuation. The transmitted signals at each transmitter position shown in Fig. 2.5.2 were acquired by using 45 receiver positions equally spaced along the tank wall and approximately corresponding to the opposite 180° sector on the storage tank. The receiver positions on the tank wall were defined according to the below presented expression:

$$\begin{aligned} x_{\mathrm{Rc},k} &= R_{\mathrm{T}} \cos\left(\varphi_{\mathrm{Tr},n} + \gamma_{\mathrm{Rc},k}\right), \\ y_{\mathrm{Rc},k} &= R_{\mathrm{T}} \sin\left(\varphi_{\mathrm{Tr},n} + \gamma_{\mathrm{Rc},k}\right), \end{aligned} \tag{2.5.2}$$

where $x_{\mathrm{Rc},k}$, $y_{\mathrm{Rc},k}$ are the coordinates of the receivers, $k = 1 \div N_{\mathrm{Rc}}$, N_{Rc} is the number of receivers, R_{T} is the radius of the tank shell, $\varphi_{\mathrm{Tr},n}$ is the angle of transmitter positioning, $n = 1 \div N_{\mathrm{Tr}}$, N_{Tr} is the number of transmitters, $\gamma_{\mathrm{Rc},k}$ is the angle of receiver positioning, $\gamma_{\mathrm{Rc}} \in [-\pi/2 \quad \pi/2]$. The angle between neighbouring receiver positions was 4°.

The signals acquired in the form of a B-scan image for the current transmitter position φ_{Tr} are presented in Fig. 2.5.6. The "fan-shaped" coverage area of the storage

tank floor corresponding to the 180° sector for current transmitter position is shown by the grey area. It can be stated that only the front part of the acquired waveforms corresponds to the propagating and symmetric S_0 guided wave mode transmitted through the tank floor because it has a higher propagation velocity and should pass the tank floor first; this part of the signal should be used for the calculation of tomographic projections. Thus, to select the signal corresponding to the propagating symmetric S_0 UGW mode, the time variable window was used. The time window boundaries necessary to select the symmetric S_0 UGW mode in the time domain can be expressed with equations 2.5.3 and 2.5.4:

$$t_{\mathrm{w1},k} = \frac{1}{c_{\mathrm{S0}}}\sqrt{\left(x_{\mathrm{Rc},k} - x_{\mathrm{Tr},n}\right)^2 + \left(y_{\mathrm{Rc},k} - y_{\mathrm{Tr},n}\right)^2}\,, \tag{2.5.3}$$

$$t_{\mathrm{w2},k} = t_{\mathrm{w1},k} + \Delta t_{\mathrm{w}}\,, \tag{2.5.4}$$

where $x_{\mathrm{Rc},k}$, $y_{\mathrm{Rc},k}$, $x_{\mathrm{Tr},n}$, $y_{\mathrm{Tr},n}$ are the coordinates of the receiver and transmitter, respectively, c_{S0} is the velocity of the symmetric S_0 wave mode in stainless steel, $k = 1 \div N_{\mathrm{Rc}}$, N_{Rc} is the number of receiver positions, $n = 1 \div N_{\mathrm{Tr}}$, N_{Tr} is the number of transmitter positions, Δt_{w} is the width of the time window. The calculated time variable window boundaries are shown in Fig. 2.5.6 by black dots.

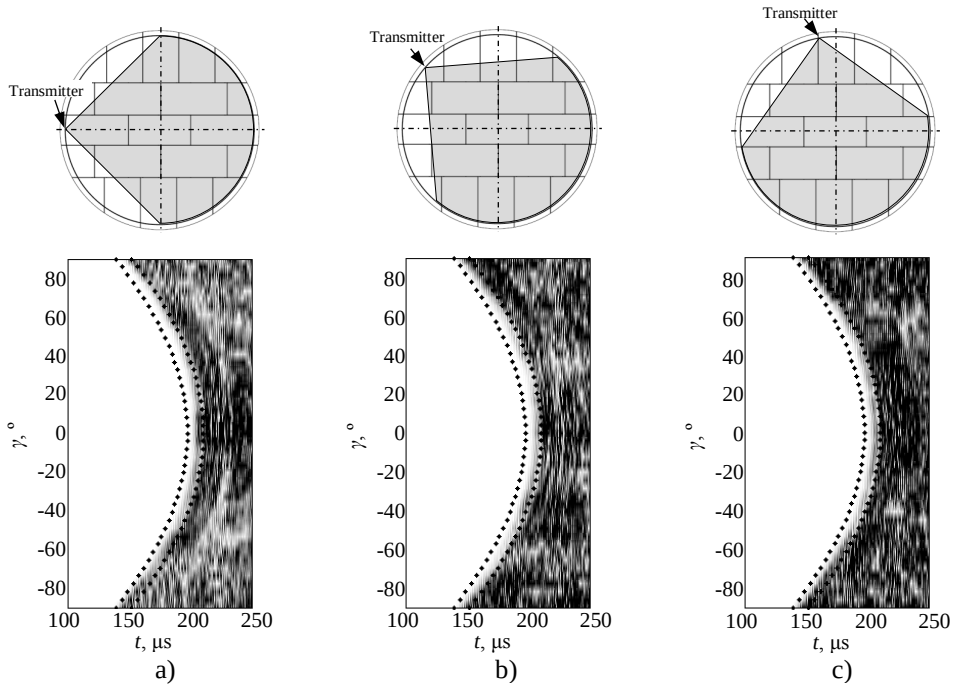

Fig. 2.5.6. The B-scan image of the particle velocity modulus measured on the opposite side of a storage tank wall when the transmitter is located at: $\varphi_{\mathrm{Tr},1} = 270°$ (a), $\varphi_{\mathrm{Tr},2} = 228.75°$ (b) and $\varphi_{\mathrm{Tr},3} = 187.5°$ (c)

The maximum amplitude of the analysed symmetric S_0 UGW mode particle velocity v_x, v_y and v_z components transmitted through the storage tank floor in the ranges of the time window were obtained, according to the expression presented below:

$$U^{n}_{\max,k} = \max\left[u_k(t)\right], \tag{2.5.5}$$

where $t \in \left\lfloor t_{w1,k},\ t_{w2,k} \right\rfloor$, $n = 1 \div N_{Tr}$, N_{Tr} is the number of transmitter positions, $k = 1 \div N_{Rc}$, N_{Rc} is the number of receiver positions. The results of particle velocity v_x, v_y, v_z components amplitude change along the arc of the storage tank wall for three different transmitter positions φ_{Tr} are presented in Fig. 2.5.7.

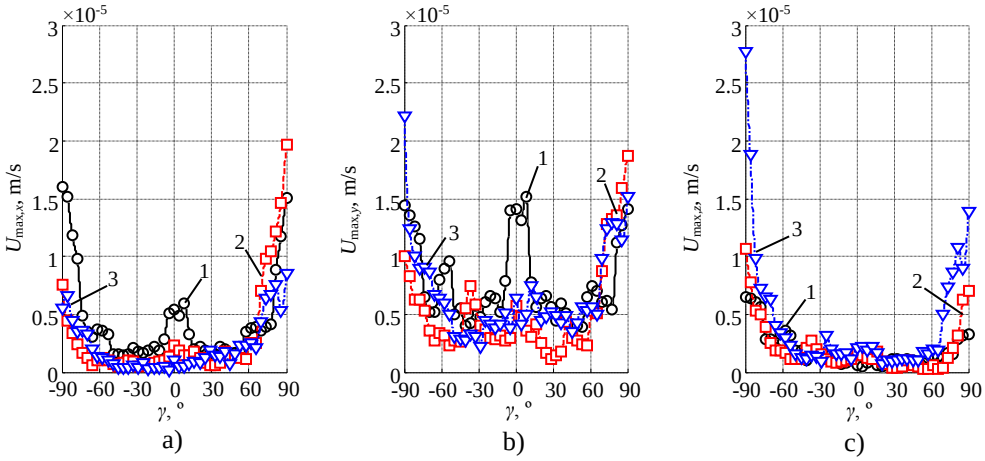

Fig. 2.5.7. The amplitude distribution of the symmetric S_0 UGW mode particle velocity v_x component (a), v_y component (b) and v_z component (c) along the arc of the storage tank wall in the case of 1 – $\varphi_{Tr,1}$ = 270º, 2 – $\varphi_{Tr,2}$ = 228.75º and 3 – $\varphi_{Tr,3}$ = 187.5º

The results suggest that the amplitude of the symmetric S_0 UGW mode transmitted through the scaled-down storage tank floor is strongly dependent on the structure of the tank floor. Thus, the signals with the highest amplitude for the presented excitation cases are obtained when the transmitter is located at $\varphi_{Tr,1}$ = 270º, and when there are only two shell-to-bottom and lap joint connections in the direct wave propagation path. The decrease of the amplitude of the symmetric S_0 UGW mode in the model is mainly caused by structure complexity and the fact that due the increase of connections in the direct wave propagation path, the overall transmission losses $\alpha_{S0}(f)$ of the analysed symmetric S_0 UGW mode transmitted over the storage tank floor and induced in the tank wall increases. Meanwhile, an increase in the relative signal amplitude at the marginal positions of the acquired projections is mainly caused by trailing waves, conditioned by occurring multiple reflections and mode conversion, as well as by waves traveling along the tank shell.

Based on the scaled-down storage tank 3D modelling results, it can be stated that the signals of propagating UGW could be measured on the tank wall with

transducers situated on the opposite side of the tank shell. However, the overall amplitude of the analysed symmetric S_0 wave mode is strongly depended on the number of joints in the wave propagation path and on the increase of transmission losses $\alpha_{S0}(f)$ conditioned by multiple connections. The modelling results also show that by using measurement configuration with transducers situated on the shell of the tank and corresponding to the 180° sector of a storage tank floor, the UGW propagating directly over the tank shell could be observed by receivers at the marginal positions.

2.6 Conclusions of the Chapter 2

1) The analysis of propagation of symmetric S_0 UGW mode has shown that the transmission losses $\alpha_{S0}(f)$ through the shell-to-bottom weld are up to 14 dB higher in the case of excitation on the wall comparing to the excitation on the edge of the storage tank floor. It has also been shown that these losses are linearly depended on the frequency.
2) The finite element modelling has demonstrated that the transmission losses $\alpha_{S0}(f)$ of the symmetric S_0 wave mode on lap joint welded plates vary in the ranges from 1 dB up to 8 dB per weld depending on the ratio between lap joint width Δl and wavelength λ. In addition, the modelling has demonstrated that additional bonding in lap joint caused by corrosion can essentially reduce the transmission losses.
3) The analysis of UGW propagation in the case of different loading conditions demonstrated that the leakage losses of the symmetric S_0 wave mode are dependent on the materials stored in the tank and can vary in the range of $2 \div 10$ dB/m. The most significant losses were observed in the case of tank floor loading by moist sand and water loads. The results of modelling suggest that moist sand on the bottom of the tank can lead to additional losses approximately equal to 10 dB/m.
4) The investigation using a 3D model of the scaled-down storage tank has demonstrated that there is no essential increase of losses in UGW propagating at some angle with respect to the weld. However, the angle on the opposite side of the storage tank at which the guided waves can be received is limited approximately to 180° due to the arrival of stronger waves directly through the tank wall.

3. EXPERIMENTAL INVESTIGATION OF ULTRASONIC GUIDED WAVES PROPAGATION THROUGH WELDED LAP JOINTS

The numerical investigation revealed that the most significant transmission losses of UGW transmitted through a storage tank floor are conditioned by lap joint welds used to join separate plates in the construction of the tank floor. By considering that there can be tens of welds across the storage tank floor, those losses may exceed 100 dB and may be the main factor limiting the achievable propagation distance. Therefore, the goal of the research in this chapter is the experimental evaluation of UGW transmission losses transmitted through the welded lap joints and its comparison with the results obtained by numerical investigation.

3.1 An analysis of ultrasonic guided waves transmission through the lap joint of different width

The objective of this research is the experimental verification of the modelling results, obtained by FE model presented in Section 2.2. For this purpose, a special test sample was manufactured by welding together two 1 mm thick stainless steel plates. The plates were welded using a lap weld with different width of the overlap zone Δl, which linearly changes from 2 mm to 15 mm (Fig. 3.1.1). The width of the weld seam was 3 mm. The experimental investigation of the symmetric S_0 UGW mode propagation through the lap weld was performed using the experimental set-up presented in Fig. 3.1.1.

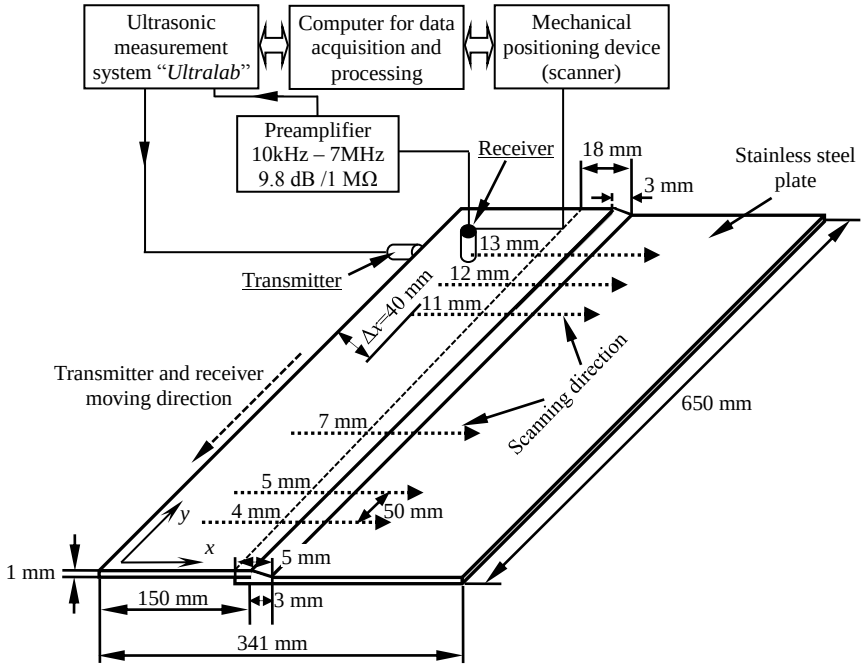

Fig. 3.1.1. The experimental set-up for the investigation of the symmetric S_0 UGW mode propagation through the welded lap joint of different overlap zone width Δl

The low-frequency ultrasonic measurement system "Ultralab", produced and manufactured at Prof. K. Baršauskas' Ultrasound Research Institute of Kaunas University of Technology was used as a control instrument for measurements. For the generation and reception of the UGW in the presented test sample having different widths of the overlap zone Δl lap joint connection, the broadband ultrasonic transducers operating in thickness mode were used [162–164]. The excitation was performed by using 3 periods of rectangular pulse with the frequency of 400 kHz and amplitude of 300 V. The reception of the propagating UGW was performed by using a low-frequency ultrasonic transducer with a special wear-proof convex form replaceable protector made from glass fibre with the width of contact area of 1 mm. The frequency responses of the ultrasonic transducers used as transmitter and receiver are shown in Fig. 3.1.2. The receiver was connected to a 9.8 dB preamplifier and after it the signals were amplified with the main amplifier. The total gain of the measurement system changed in the ranges of 36.8 dB–44.8 dB. The frequency range of the amplifier filter was 0.02–2 MHz. The signals were digitised with a sampling frequency of 100 MHz.

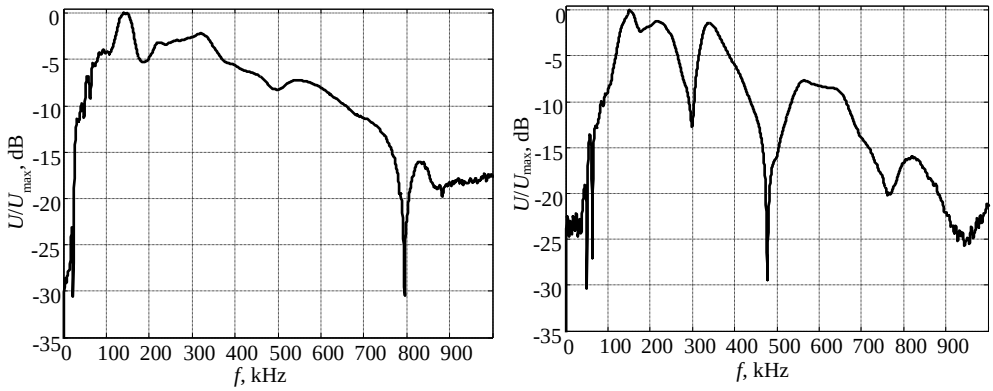

Fig. 3.1.2. The frequency responses of the transmitter without a replaceable protector (a) and a receiver with a convex protector (equivalent diameter of the contact area is 1 mm) (b)

During the experimental research, the transmitter was attached at the first position to the edge of the plate (in order to create longitudinal force) using a specially developed spring-type adjuster and the receiver was scanned across the weld in the x direction (Fig. 3.1.1.). Scanning of the test sample for the B-scan type data collection of the propagating UGW was performed by using the one-axis scanner with the scanning step of 0.1 mm and the total scanned distance was x = 270 mm. Oil was used as the coupling material between transducers and the test sample. At each position, the signals were recorded to form a B-scan image of the UGW propagating in the lap welded stainless steel plates. In order to improve the signal-to-noise ratio, the 8 signals were averaged at each measurement position. The initial distance between the transducers was set to be Δx = 40 mm. It was selected so that asymmetric A_0 and symmetric S_0 guided wave modes would separate in the time domain at the initial measurement position. Then, the transmitter was attached to the second position along the edge and the scanning was repeated. The distance between each next position

along the plate edge was 50 mm. The measurements were performed in the part of the edge with the length of 450 mm. It enabled to investigate the test sample in the area where the width of the lap joint overlap zone Δl gradually changes from 4 mm to 13 mm with the step of 1 mm.

As an example, the measured signals in the form of a B-scan image (4 mm overlap) is presented in Fig. 3.1.3a. The dashed lines denote the positions of the lap welds. In the B-scan image, the pattern of the propagating symmetric S_0 and asymmetric A_0 UGW modes could be clearly observed, as well as the occurring reflection and mode conversion on the weld. For a more advanced analysis of the measured multimodal UGW signals, the 2D Fourier transform (2D FT) was used to decompose the signals into both spatial and temporal domains. The advantage of a 2D FT is that the UGW modes with the same frequency but different wavenumbers can be differentiated, whereas Fourier analysis in the frequency domain alone cannot achieve this. According to the 2D FT method, the waves propagating along the object can be converted from the space–time domain into the wavenumber–frequency domain by a general expression [165–170]:

$$U(k, f) = \int_{-\infty}^{+\infty}\int_{-\infty}^{+\infty} u(x,t)e^{-i(kx+\omega t)}dxdt\,, \tag{3.1.1}$$

where x is the spatial coordinate, t is time, ω is the angular frequency, k is the wavenumber. By considering the wavenumber k and phase velocity c_{ph} relation, the waves propagating in the object could be expressed as a function of phase velocity c_{ph} and frequency. The reconstructed patterns of the dispersion curves of the UGW modes propagating in the lap welded plate are presented in Fig. 3.1.3b.

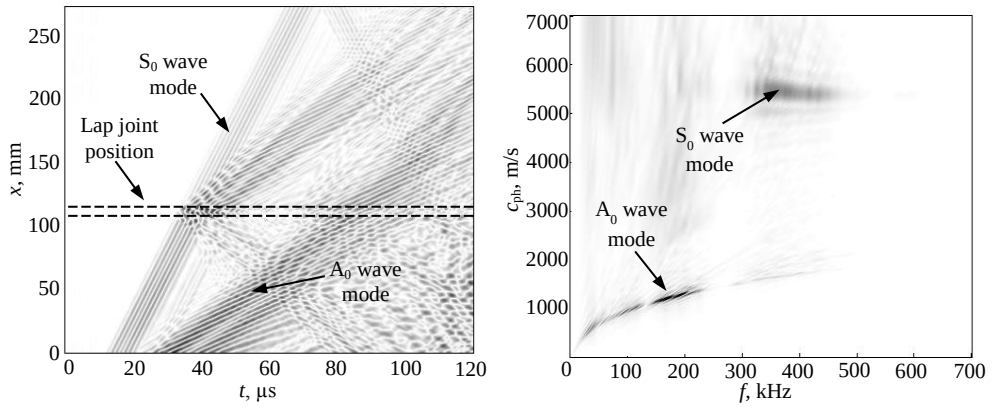

Fig. 3.1.3. An experimentally obtained B-scan image of the UGW propagating through the lap joint welded plates in the case of the 4 mm overlap zone width (a), reconstructed UGW dispersion curve pattern by using 2D FT (b)

The results presented in Fig. 3.1.3 reveal that the most dominant and strongest propagating UGW mode in the investigated test sample is the asymmetric A_0 wave mode. It could be explained by the fact that the thickness mode ultrasonic transducer

was used for the reception. Such transducer has an essentially higher sensitivity to the out-of-plane u_y displacement component which is dominant for the asymmetric A_0 wave mode motion. The propagating symmetric S_0 wave mode which has a lower amplitude, can be clearly observed also. It can be noticed that the asymmetric A_0 guided wave mode in the investigated test sample was generated at the 40–450 kHz frequency range. Meanwhile, the symmetric S_0 wave mode was generated at the frequency range of 320–450 kHz.

In order to separate the signals of the symmetric S_0 wave mode propagating in a forward direction from the reflected waves and from other UGW modes, the 2D filtering in wavenumber–frequency domain was used. The filtering process can be mathematically expressed as a product of the wavenumber–frequency spectrum $U(k, f)$ and filter function $W(k, f)$ [167–169]:

$$U_W(k, f) = U(k, f) \cdot W(k, f), \tag{3.1.2}$$

where, $W(k, f)$ is the 2D bandpass filter in the wavenumber – frequency domain and $U_W(k, f)$ is the filtered 2D spectrum. The filtered spectrum $U_W(k, f)$ is then transformed back into the space–time domain using the inverse 2D FT in order to obtain a filtered wave field $u_W(x,t)$ [167–169]:

$$u_W(x,t) = \mathrm{FT}_{2D}^{-1}\left[U_W(k, f)\right]. \tag{3.1.3}$$

The filtered 2D $U_W(k, f)$ spectrum converted into phase velocity–frequency domain $U_W(c_{\mathrm{ph}}, f)$ and reconstructed afterwards B-scan $u_W(x,t)$ images are presented in Fig. 3.1.4.

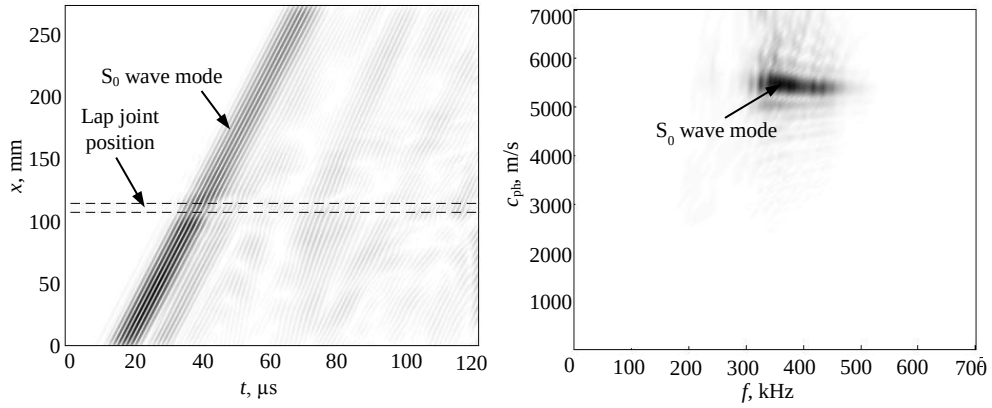

Fig. 3.1.4. Filtered B-scan image of the UGW propagating through the lap joint welded plates in the case of the 4 mm overlap zone width (a), reconstructed UGW dispersion curve pattern by using 2D FT from filtered data (b)

As the B-scan image shows, the other guided wave modes and reflected waves are completely filtered. Two signals were selected for the assessment of transmission losses $\alpha_{S0}(f)$ on the weld – one before the weld, another one – after. The first one,

used as a reference signal was measured at the distance of 90 mm ($x + \Delta x$) from the transmitter or the edge of the plate. The other was measured at 265 mm away from the transmitter. The obtained waveforms of the UGW signals measured before lap joint connection and transmitted through lap joint connections of different widths Δl are presented in Fig. 3.1.5 and Fig. 3.1.6, respectively. The Hanning time window was used to select the segment of the signal corresponding to the propagating symmetric S_0 wave mode. The transmission losses $\alpha_{S0}(f)$ on the lap weld of the symmetric S_0 UGW mode in the case of different width Δl lap joint connections were estimated according to the equation 2.1.11 considering only the value corresponding to the frequency of f = 400 kHz. The dependency of transmission losses, by taking into account the fall-off of the signal due to the distance, are presented in Fig. 3.1.7. For comparison, the dependency obtained by FE modelling is also presented.

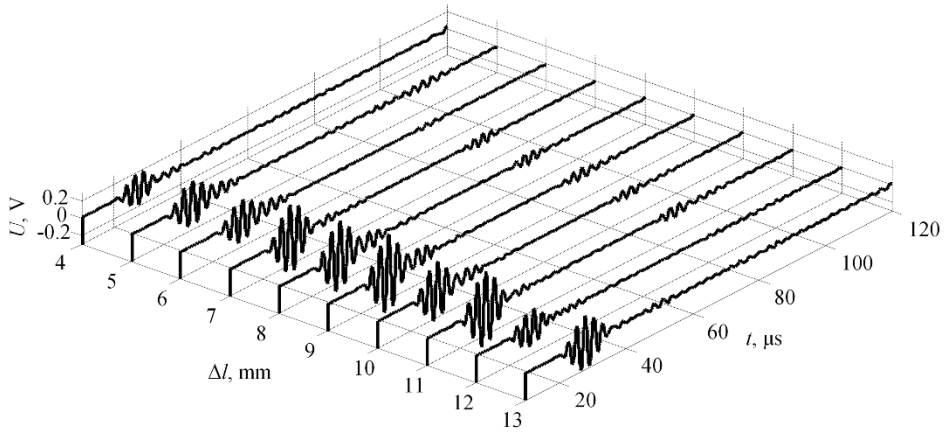

Fig. 3.1.5. The waveforms of the filtered UGW signals measured before lap joint connection in the different widths of the overlap zone Δl

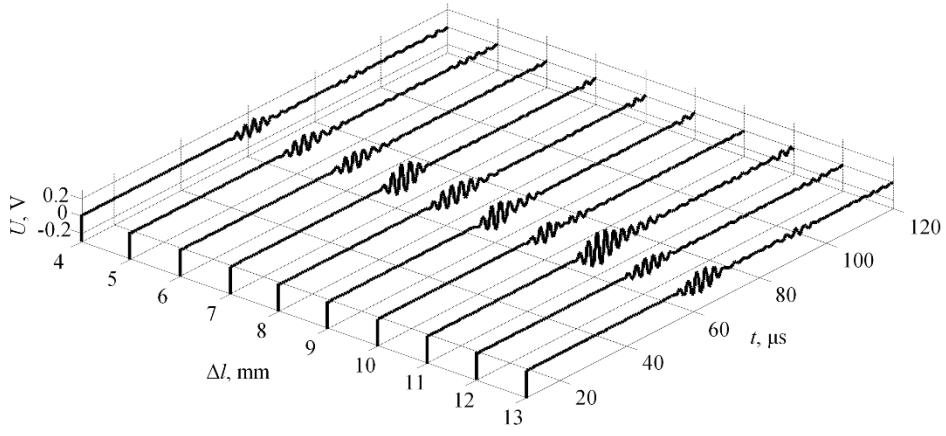

Fig. 3.1.6. The waveforms of the filtered UGW signals transmitted through the lap joint welded plates in the case of different widths of the overlap zone Δl

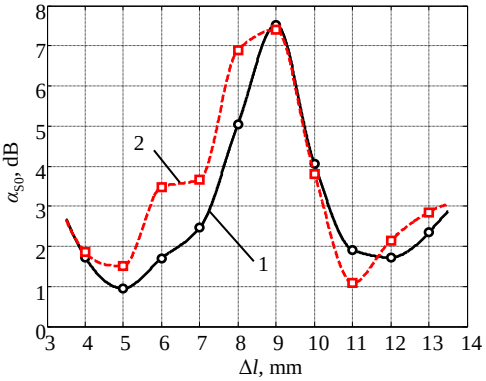

Fig. 3.1.7. The transmission losses $\alpha_{S0}(f)$ of the S_0 wave mode obtained by 1 – using the finite element (FE) method of numerical simulation, 2 – measured experimentally

It was observed that the experimentally measured transmission losses $\alpha_{S0}(f)$ of the symmetric S_0 UGW mode possess a variation similar to those obtained by FE modelling. It was estimated that the highest transmission losses are obtained in the 9 mm overlap zone width and are approximately 7.6 dB. This maximum of transmission losses occurs due to the interference of waves directly propagated through the lap joint weld and the waves reflected by the free edge of the lap joint. Meanwhile, the observed difference from the numerical results are mainly conditioned by mounting of the transmitting transducer to the edge of the plate, i.e. parallelism of fixing which directly affects the acoustical contact and are particularly important in amplitude measurements.

3.2 An analysis of the guided waves propagation through the lap joint

The purpose of the experimental investigation is to determine the transmission losses $\alpha_{S0}(f)$ of the symmetric S_0 UGW mode as it passes through the multiple lap joint connections of welded stainless steel plates and to compare the experimentally measured results with those obtained by using the FE analysis method. To achieve this purpose, an experimental investigation on the UGW propagation through multiple lap joint connections of the welded stainless steel plates was carried out by using the experimental set-up presented in Fig. 3.2.1.

The measurements of UGW propagation through multiple lap joint welded stainless steel plates was performed by using a low-frequency ultrasonic measurement system "Ultralab", produced and manufactured at Prof. K. Baršauskas' Ultrasound Research Institute of Kaunas University of Technology. For the excitation of the UGW Pz29 piezoceramic sample (12×7×5 mm), with natural vibrations mode frequencies of around 400 kHz mounted directly to the surface of the lap joint welded plates sample via epoxy was used. The excitation was performed by using 3 periods of rectangular pulse with the frequency of 400 kHz. The reception of the propagating UGW in the investigated object was performed by using a low-frequency ultrasonic transducer operating in thickness mode and having a special wear-proof convex form replaceable protector made out of glass fibre with a contact area of 1 mm [162–164].

The thickness of the welded stainless steel sheets was 1 mm. The width of the lap joint overlap zone and the width of the weld seam were 9 mm and 3 mm, respectively. Scanning of the test sample for the B-scan type data collection was performed by using the one-axis scanner with the scanning step of 0.25 mm. The total scanned distance was x = 450 mm. To ensure good acoustical contact between the receiver and the test sample, oil was used as coupling material. The initial distance between transducers was set to be Δx = 60 mm. The receiver was connected to a 13.4 dB preamplifier and after it the signals were amplified by the main amplifier. The total gain of the measurement system was 45.4 dB. The frequency range of the amplifier filters was 0.02–2 MHz. In order to improve the signal-to-noise ratio averaging of 8 signals at each measurement position was performed. The signals were digitised with a sampling frequency of 100 MHz. The experimentally obtained B-scan image of the propagating UGW and dispersion curves pattern reconstructed by using the 2D FT method are presented in Fig. 3.2.2.

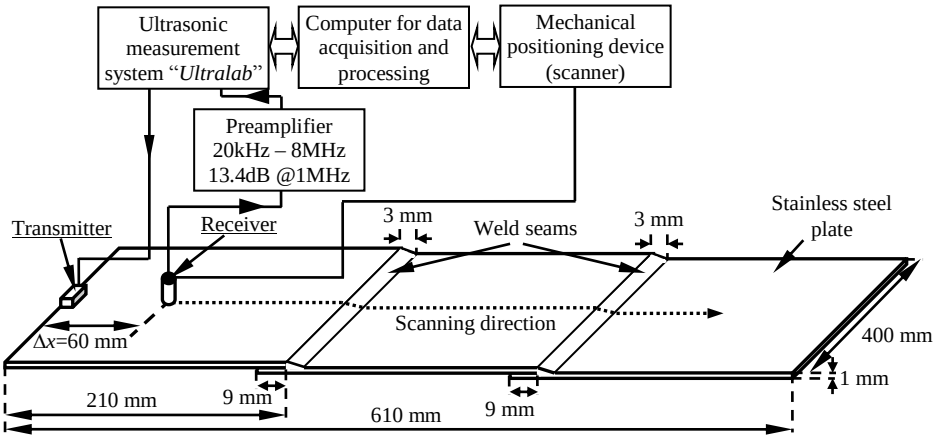

Fig. 3.2.1. The experimental set-up used for the investigation of UGW propagation through multiple lap joint welded plates

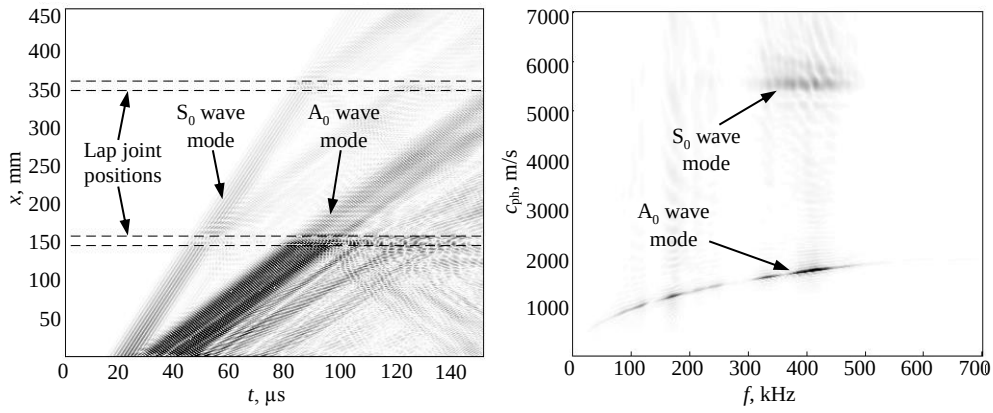

Fig. 3.2.2. The experimental B-scan image of UGW propagating in the lap joint welded plates (a), UGW dispersion curve pattern reconstructed by using 2D FT (b)

The results presented in Fig. 3.2.2a allow the observation that by using the presented excitation scheme both asymmetric A_0 and symmetric S_0 wave modes are generated in the investigated object. Amplitude reduction and mode conversion leading to newly generated modes and energy dissipation at the lap joint connection positions could be observed as well. The reconstructed symmetric S_0 guided wave mode dispersion curve pattern presented Fig. 3.2.2b indicates that the symmetric wave mode in the investigated structure was generated in the 300–450 kHz frequency bandwidth. In order to separate the signals of the symmetric S_0 UGW mode propagating in a forward direction from the reflected waves and from other guided waves modes, the 2D filtering in wavenumber–frequency domain was performed by using the technique presented in Section 3.1. The filtered B-scan image of the propagating UGW in the welded stainless steel plates and dispersion curves pattern of the symmetric S_0 mode reconstructed with 2D FT are presented in Fig. 3.2.3.

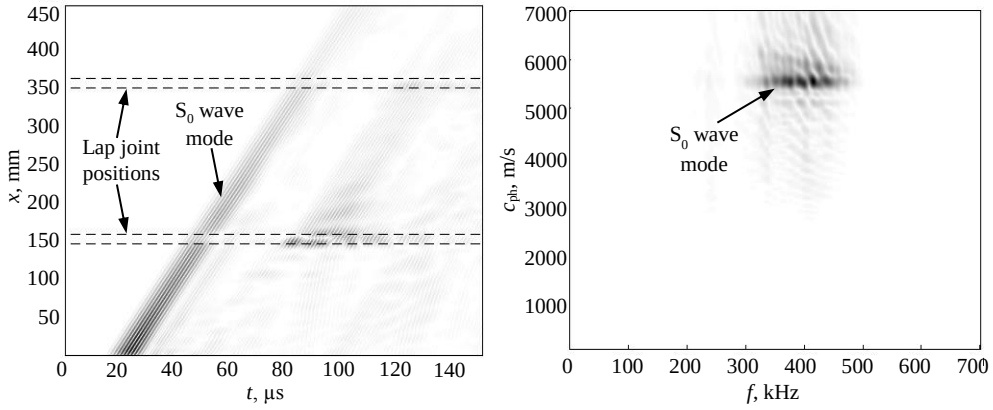

Fig. 3.2.3. The filtered B-scan image of the UGW propagating in the lap joint welded plates (a), reconstructed UGW dispersion curve pattern by using 2D FT from filtered data (b)

To estimate the transmission losses $\alpha_{S0}(f)$ of the propagating symmetric S_0 UGWe mode as it passes through the lap joint connection, the signals at different positions were distinguished. They were obtained at Rc1 – 160 mm, Rc2 – 330 mm and Rc3 – 510 mm away from the transmitter, which corresponds to the position before lap joint, after the first and the second lap joint connections, respectively. The analysed symmetric S_0 guided wave mode was picked by using a Hanning window and the spectra ratio of this mode was calculated by using equation 2.1.11. The obtained waveforms of the propagating ultrasonic guided waves signals, spectra of the windowed symmetric S_0 guided wave mode and its transmission losses $\alpha_{S0}(f)$ as it passes through the lap joint connection of welded stainless steel plates are presented in Fig. 3.2.3–Fig. 3.2.5, respectively.

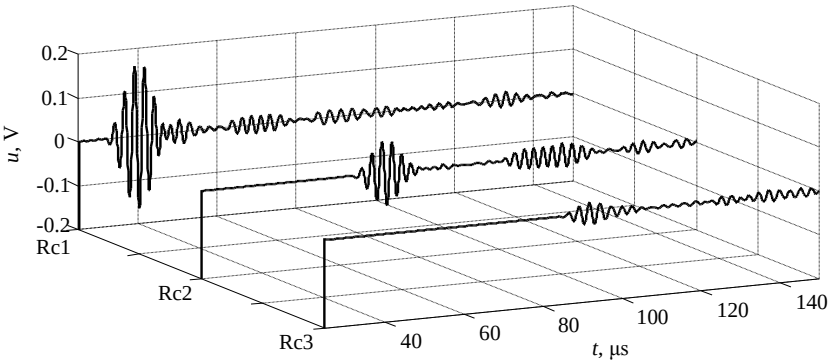

Fig. 3.2.4. Waveforms of the UGW signals in the lap joint welded plates at Rc1 – before lap joint, Rc2 – after the 1st lap joint and Rc3 – after the 2nd lap joint connection, respectively

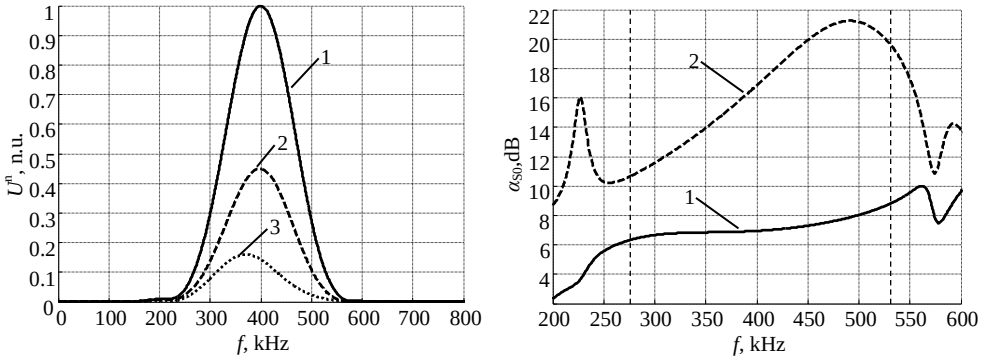

a) b)

Fig. 3.2.5. The spectra of the S_0 UGW mode propagating in lap joint welded plates: 1 – before the lap joint, 2 – after the 1st lap joint and 3 – after the 2nd lap joint connection (a), transmission losses $\alpha_{S0}(f)$ of the S_0 UGW mode after 1 – the 1st lap joint, 2 – the 2nd lap joint (b)

The experimental investigation has revealed that due to the lap joint connection between the welded stainless steel plates, the amplitude of the symmetric S_0 guided wave mode transmitted through the lap joint decreases by 7.2 dB as it passes through the first lap joint connection. Meanwhile, the total transmission losses of this wave mode transmitted through multiple – first and second lap joint connections were estimated to be 16.8 dB at the frequency of 400 kHz. It is possible to claim that the average transmission losses $\alpha_{S0}(f)$ of the investigated symmetric S_0 wave mode are approximately 8.4 ± 1.7 dB/weld. In addition, the experimentally obtained results demonstrated good agreement with the results predicted by FE analysis method in the case of symmetric S_0 UGW mode propagation through the lap joint connection when plates are connected with each other only by a weld seam.

3.3 Conclusions of the Chapter 3

1) The experimental investigation of GW losses on lap welds in general has proven the regularities obtained by modelling by demonstrating the variation of transmission losses $\alpha_{S0}(f)$ of the symmetric S_0 wave mode in the ranges of 1–8 dB per weld that are related to the ratio of the overlap zone width and wavelength of propagating waves.
2) To better demonstrate the dependency of transmission losses on the width of the overlap zone and wavelength, additional experimental investigation was carried out. It has shown that in the case of the 9 mm overlap zone width, the average transmission losses of the S_0 wave mode are 8.4 ± 1.7 dB per weld, by taking results corresponding to the central frequency of the excitation signal.

4. AN EVALUATION OF THE OPTIMAL ULTRASONIC TOMOGRAPHY PARAMETERS BY USING THE PROPOSED MODEL

Tomography is a technique mainly known as x-ray or computed tomography. The key feature of tomography is that it enables relatively accurate imaging of the internal structure of an object. In the case of x-ray tomography, the features of reconstructed image are related to the density variation of the object under investigation. In this regard, ultrasonic tomography is more complicated due to the presence of several factors affecting the amplitude of propagating ultrasonic waves. Such factors are wave diffraction, refraction, scattering, attenuation, dispersion, etc. Additionally, the storage tank floor inherently has sources of attenuation, such as wave energy leakage losses into the surrounding environment and the transmission losses on the weld. In most works related to ultrasonic transmission tomography, mainly the spatial distribution of attenuation is presented and the results of reconstruction do not relate them to the absolute value of the losses. However, in NDT this absolute value of attenuation is the key parameter as it can be related to the level of corrosion, or in most cases, to the level of thickness reduction which enables to reconstruct the true values of attenuation at the same time reconstructing the spatial distribution.

4.1 The tomographic reconstruction algorithm

The tomographic reconstruction technique, in general, is defined as the method which enables to reconstruct the spatial distribution of some physical property in the cross-section of an object using the so-called projections. The basic principle of ultrasonic tomography and tomographic reconstruction methods were defined in more detail in Section 1.3 and Section 1.4. In our case, for a storage tank floor inspection, the physical parameter that needs to be reconstructed is the attenuation distribution of the symmetric S_0 UGW mode.

The storage tank floor is a relatively good object for tomographic reconstruction as it possesses a circular shape. The tomographic technique consists of two main stages – data acquisition and image reconstruction. The acquisition of data for one projection is performed by exciting one transducer (transmitter) and receiving the signals with transducers allocated on the opposite circumferential edge of the storage tank floor, as it is presented in Fig. 4.1.1. Afterwards, the same procedure is repeated for other transmitter positions, thus acquiring signals for the definition of projections. The attenuation of the UGW is expected by the amplitude of the signal segment corresponding to the arrival instance of symmetric S_0 wave mode. As the symmetric S_0 wave mode is the fastest, it appears in the front part of the received guided waves trails.

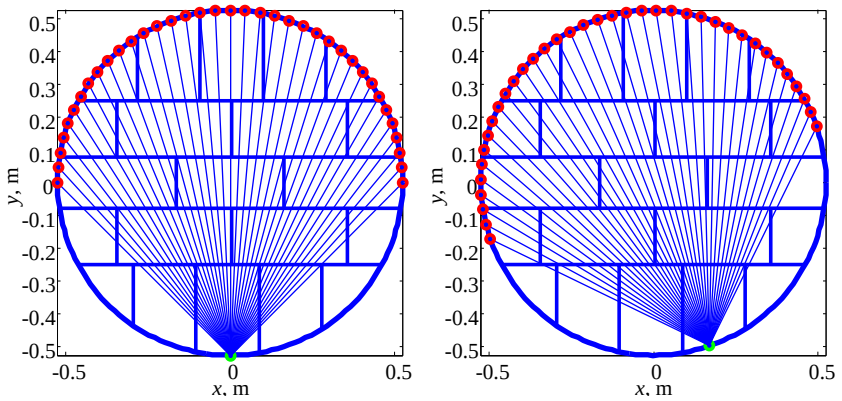

Fig. 4.1.1. A distribution of transmitters and receivers on the edge of the tank floor in two positions of transmitters using a fan-type configuration

The projection is defined as the variation of the amplitude $A(n,m)$ of the symmetric S_0 wave mode along the opposite to transmitter circumferential edge on the storage tank floor, where $n = 1 \div N$, $m = 1 \div M$; N is the total number of the receiver positions for each transmitter position; M is the total number of the transmitter positions. In the simplest case, if there are no welds in the storage tank floor (Fig. 4.1.2a), the projection for a single transmitter position could be observed (Fig. 4.1.2b). The circular areas in the storage tank floor model were used to introduce zones with an increase in attenuation of the UGW as the primary effect of corrosion. Before reconstruction, each of the projections is filtered according to the requirement of tomographic reconstruction by using a filter. Typically, filtering of the projection data is performed by using a ramp filter, which is a high-pass filter that does not permit low frequencies that cause blurring to appear in the reconstructed image. The typical tomographic ramp filter is defined as:

$$H_{\mathrm{T}}(f_{\mathrm{x}}) = \begin{cases} f_{\mathrm{x}}, & |f_{\mathrm{x}}| < f_{\mathrm{x,max}} \\ 0, & \text{otherwise} \end{cases}, \tag{4.1.1}$$

where f_{x} is the spatial frequency, $f_{\mathrm{x,max}} = 1/2d_{\mathrm{x}}$ is the maximum spatial frequency (the upper analysed frequency range); d_{x} is the step between receivers (sampling of the projection in space domain). An example of a typical tomographic filter is presented in Fig. 4.1.3a. The filtering was performed in the frequency domain by using the expression presented below:

$$A_{\mathrm{F}}(n,m) = \mathrm{Re}\left\{ \mathrm{FT}^{-1}\left[\underset{n}{\mathrm{FT}}\left[A(n,m)\right] \cdot H_{\mathrm{T}}(f_{\mathrm{x}}) \right] \right\}, \tag{4.1.2}$$

where FT^{-1} is the inverse Fourier transform and $\underset{n}{\mathrm{FT}}\left[A(n,m)\right]$ denote a direct Fourier transform of the projections. An example of a filtered projection for a single transmitter position is presented in Fig. 4.1.3b.

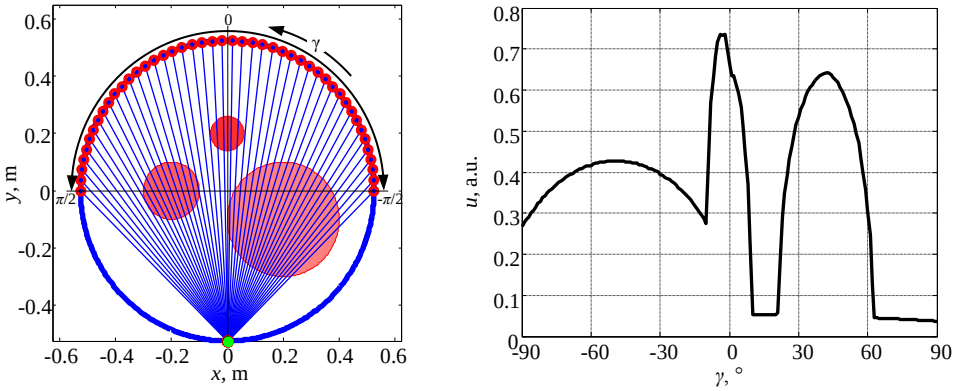

a) b)

Fig. 4.1.2. The distribution of the transmitter and receivers on the edge of a storage tank floor without welds (a) and an example of one projection as a variation of amplitude at one position of the transmitter (b)

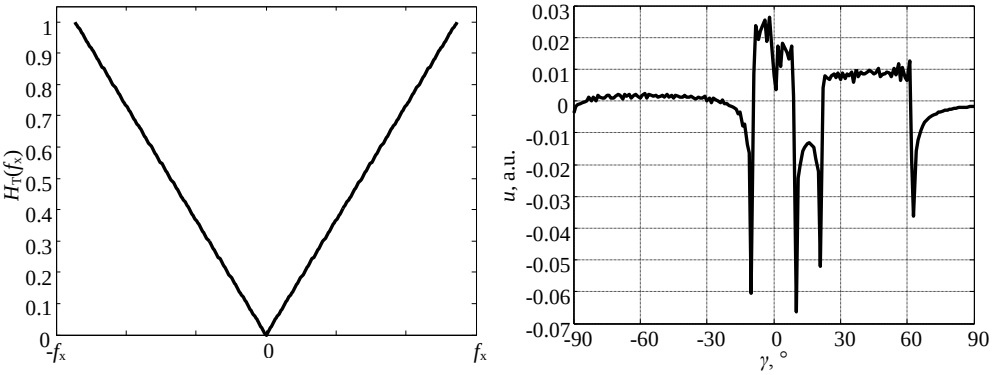

a) b)

Fig. 4.1.3. The frequency response of the ramp filter (a) and an example of a filtered projection at one position of the transmitter (b)

However, such a filter with the characteristic linearly increasing with spatial frequency leads to relatively strong reverberations (high-frequency noise) in the filtered projection which is caused by the amplification of statistical noise in the measurement results (Fig. 4.1.3b) even in the case of a smooth projection (Fig. 4.1.2b). In order to reduce the effect of amplification of high frequencies, the ramp filter was combined with a low-pass filter. The common method to reduce statistical noise is the application of the smoothing filter, which is a low-pass filter and allows the low frequencies to be retained unaltered and block the high-frequencies. The smoothing filter used in this research is defined as:

$$H_{\mathrm{sf}}(f_{\mathrm{x}}) = \begin{cases} e^{-a_{\mathrm{sf}}(f_{\mathrm{x}}-(f_{\mathrm{sf0}}-\Delta f_{\mathrm{sf}}))^2}, & |f_{\mathrm{x}}| < f_{\mathrm{sf0}} - \Delta f_{\mathrm{sf}} \\ 1, & \text{otherwise} \end{cases}, \tag{4.1.3}$$

where f_{sf0} is the cut-off frequency of the smoothing filter at 6 dB level; $a_{sf} = -\frac{\ln 0.5}{\Delta f_{sf}^2}$, Δf_{sf} is the bandwidth of the smoothing filter. The tomographic filter was corrected by multiplying the ramp filter $H_T(f_x)$ and smoothing filters $H_{sf}(f_x)$:

$$H_{Tc}(f_x) = H_T(f_x) \cdot H_{sf}(f_x). \tag{4.1.4}$$

The frequency responses of the filters are presented in Fig. 4.1.4a. The final version of projection filtering is performed according to:

$$A_{Fsf}(n,m) = \mathrm{Re}\left\{ \mathrm{FT}^{-1}\left[\underset{n}{\mathrm{FT}}\left[A(n,m)\right] \cdot H_{Tc}(f_x) \right] \right\}. \tag{4.1.5}$$

An example of a filtered projection when the corrected filter $H_{Tc}(f_x)$ is used is presented in the Fig. 4.1.4b. As the figure shows, the high-frequency noise, or reverberations, are essentially reduced.

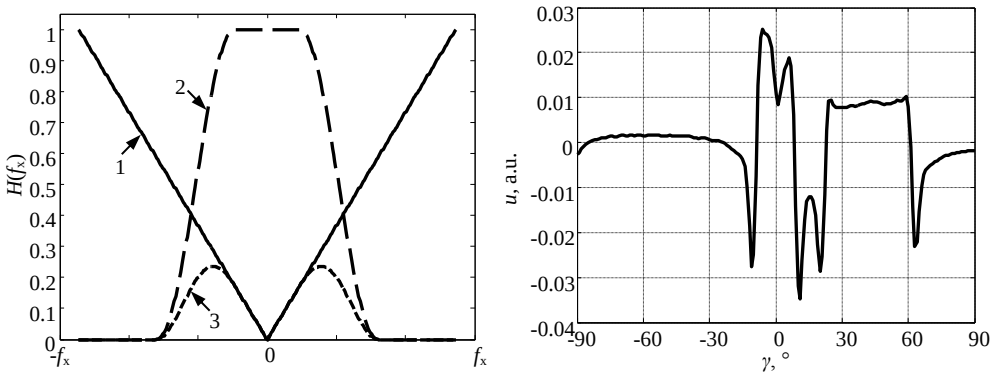

a) b)

Fig. 4.1.4. The frequency responses of the tomographic filters: 1 – ramp filter $H_T(f_x)$, 2 – smoothing (low-pass) filter $H_{sf}(f_x)$, 3 – corrected tomographic filter $H_{Tc}(f_x)$ (a), the filtered projection when the corrected tomographic filter is used (b)

The back-projection is performed by creating an array of the storage tank floor which is defined by the set:

$$\left\{ x_{tf}(n_x, n_y),\ y_{tf}(n_x, n_y),\ \alpha_{tf}(n_x, n_y) \right\}, \tag{4.1.6}$$

where n_x, n_y are the number of points along x and y-axis; x_{tf}, y_{tf} are the spatial coordinates of these points and α_{tf} is the reconstructed attenuation coefficient in dB/m at the positions of virtual points. At the beginning $\alpha_{tf} = 0$ for all points. In the following stage, each of the filtered projections is back-projected on this virtual image. The back-projection is performed in the following steps:

1. Each of the paths between the transmitter and the receiver is expressed in the form of a linear equation:

$$A_{BP}(n,m) \cdot x + B_{BP}(n,m) \cdot y + C_{BP}(n,m) = 0, \tag{4.1.7}$$

where $A_{BP}(n,m) = y_{Rv}(n,m) - y_{Tr}(n,m)$; $B_{BP}(n,m) = -\left[x_{Rv}(n,m) - x_{Tr}(n,m)\right]$; $C_{BP}(n,m) = A_{BP}(n,m) \cdot x_{Tr}(n,m) - B_{BP}(n,m) \cdot y_{Tr}(n,m)$.

2. The distances between each of the points and in the virtual image and back-projection lines are estimated:

$$D_{BP}(n,m,n_x,n_y) = \frac{\left|A_{BP}(n,m) \cdot x_{tf}(n_x,n_y) - B_{BP}(n,m) \cdot y_{tf}(n_x,n_y) + C_{BP}(n,m)\right|}{\sqrt{A_{BP}^2(n,m) - B_{BP}^2(n,m)}}. \quad (4.1.8)$$

3. The index of the closest path in each of the projections is estimated for each virtual point:

$$K_{min}(m,n_x n_y) = \arg \min_n \left[D_{BP}(n,m,n_x,n_y)\right]. \quad (4.1.9)$$

4. The image is obtained by integrating the closest part for each virtual point:

$$\alpha_{tf}(n_x,n_y) = \sum_{m=1}^{M} A\left(K_{min}(m,n_x,n_y),m\right). \quad (4.1.10)$$

To investigate the performance of the tomographic reconstruction algorithm for the reconstruction of attenuation distribution in the storage tank floor, the numerical model was created and is presented in the next section.

4.2 Tank floor model for the verification of tomographic reconstruction algorithm

The objective of the modelling is to determine the possibilities of tomographic reconstruction in the case of different values of attenuation in the plate, corroded areas and in welds. And at the same time, to determine expected sources of uncertainties for the reconstruction of the spatial attenuation distribution in the storage tank floor. To achieve it, a model of the storage tank floor, allowing to define the possible losses in welds and in the arbitrary form defects, has been built and is presented in this section. The model of the storage tank floor is represented as a circular or disk-shaped structure in Fig. 4.2.1.

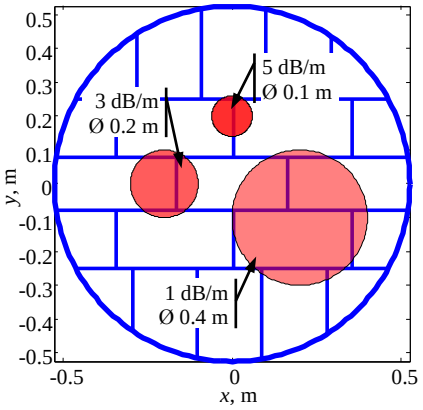

Fig. 4.2.1. The example of a storage tank floor model with denoted welds (blue line) and corroded areas with higher attenuation (red areas)

The parameters defining the structure and geometry of the storage tank floor are:

- Diameter D_T of the tank floor;
- Positions of the welds, defined as segments of the line with the start and end coordinates defined as the set $S_W\{x_{1W}(n_w); x_{2W}(n_w); y_{1W}(n_w); y_{2W}(n_w)\}$, where x_{1W}, y_{1W} are weld start coordinates; x_{2W}, y_{2W} are weld end coordinates; $n_w = 1 \div N_x$, N_x is the total number of welds in the tank floor;
- A virtual image of the tank floor representing the distribution of the attenuation in the tank floor. For that purpose, the area of the tank floor is sampled in spatial step d_{xy} and the array of the virtual image is created as a matrix $\alpha_T(n_T, m_T)$, where $n_T = m_T = 1 \div N_T$, $N_T = D_T/d_{xy} + 1$. Each point of this matrix defines attenuation per meter of the symmetric S_0 mode of UGW in the plate at that point. The coordinates of the points are defined by $P_T(n_T, m_T)$, $x_T = (n_T - 1)\cdot d_{xy} - D_T/2$, $y_T = (m_T - 1)\cdot d_{xy} - D_T/2$. In principle, the model enables to set any arbitrary distribution of attenuation on the tank floor. Additionally, some temporal matrix $K_T(n_T, m_T)$ is created the purpose of which is explained below.

The next group of parameters defines the possible losses of UGW in the storage tank floor. In general, this is reference information which needs to be reconstructed by the tomographic algorithm. It includes the following values:

- Attenuation per meter α_{S0} of the symmetric S_0 wave mode in the tank floor plate, which defines the average attenuation in the plate.
- Attenuation in corroded areas. Two possible shapes of corroded areas were introduced in the tank floor model – circular and rectangular. The circular areas of higher attenuation were introduced by the following parameters:
    1. Attenuation $\alpha_{cd}(n_{cd})$, $n_{cd} = 1 \div N_{cd}$, N_{cd} is the total number of circular defects;
    2. Position of the centre $\{x_{cd}(n_{cd}); y_{cd}(n_{cd})\}$;
    3. Diameter $d_{cd}(n_{cd})$ of the circular defect.

  The rectangular corroded areas with higher attenuation were introduced by the following parameters:
    1. Attenuation $\alpha_{rd}(n_{rd})$, $n_{rd} = 1 \div N_{rd}$, N_{rd} is the total number of rectangular defects;
    2. Positions of the left upper and right lower corners of the rectangular area $S_{rd}\{x_{1rd}(n_{rd}); y_{1rd}(n_{rd}); x_{2rd}(n_{rd}); y_{2rd}(n_{rd})\}$;
- Losses in the weld α_W. Usually, the losses in the weld are defined as attenuation per weld. However, in our case, the reconstruction parameter is attenuation per meter. In order to meet this requirement, the losses in the weld are also defined as attenuation per meter with an introduced width of the weld. It is necessary to take into account that the width of the weld is relatively small compared with the dimensions of the tank floor or even steel plates sheets which compose the storage tank floor. Thus, if to calculate the losses

per weld into the attenuation per meter with a real width of the weld, an extremely high attenuation value will be obtained. So, in the models, a virtual value of the weld width d_W was used which can be bigger than the real one. In such approach, the attenuation in the weld is introduced as a rectangular area $\{S_W, d_W\}$ with a corresponding attenuation coefficient α_W. In the present model, it is also assumed that the attenuation in the welds does not depend on the wave incident angle and is the same and uniform for all welds.

The virtual attenuation map created by comparison of each point of attenuation map $\alpha_T(n_T, m_T)$ with attenuation zones and corresponding attenuation value is assigned. It means:

$$\alpha_T(n_T, m_T) = \begin{cases} \alpha_W, P_T \in \{S_W, d_W\}; \\ \alpha_{cd}, P_T \in \{x_{cd}(n_{cd}); y_{cd}(n_{cd}); d_{cd}(n_{cd})\}; \\ \alpha_{rd}, P_T \in S_{rd}. \end{cases} \quad (4.2.1)$$

If the point belongs to several zones, only the attenuation of the first zone according to priority is assigned. In order to implement this approach, the temporal array $K_T(n_T, m_T)$ is used. The described attenuation zones are analysed according to the priority order. When the first attenuation zone where the point under analysis is situated is found, the corresponding element of the temporal array is set to one $K_T(n_T, m_T) = 1$. In other zones, the element of the temporal array is already equal to 1 and the modification of the attenuation map $\alpha_T(n_T, m_T)$ is not performed. Such an algorithm enables to control the calculation of the attenuation map when the point $P_T(n_T, m_T)$ belongs to several attenuation zones; for example, to the weld and circular area. In this case, only the first assignment is performed.

Another condition is related to the fact that the attenuation map covers a rectangular area as the storage tank floor is circular object. Therefore, all points of the attenuation map outside the tank floor are set to zero:

$$\alpha_T(n_T, m_T) = \begin{cases} 0, & \sqrt{x_T^2 + y_T^2} > D_T/2 \\ \alpha_T(n_T, m_T), & \text{otherwise} \end{cases}. \quad (4.2.2)$$

Several specific cases of attenuation distribution in the storage tank floor using the model developed have been created and are presented in Fig. 4.2.2. The cases are:

1. there is some value of ambient attenuation (0.5 dB/m) in non-corroded plate areas and no attenuation in welds (Fig. 4.2.2a);
2. there is some value of ambient attenuation (0.5 dB/m) in non-corroded plate areas and the attenuation in welds is 2 dB/weld (Fig. 4.2.2b).

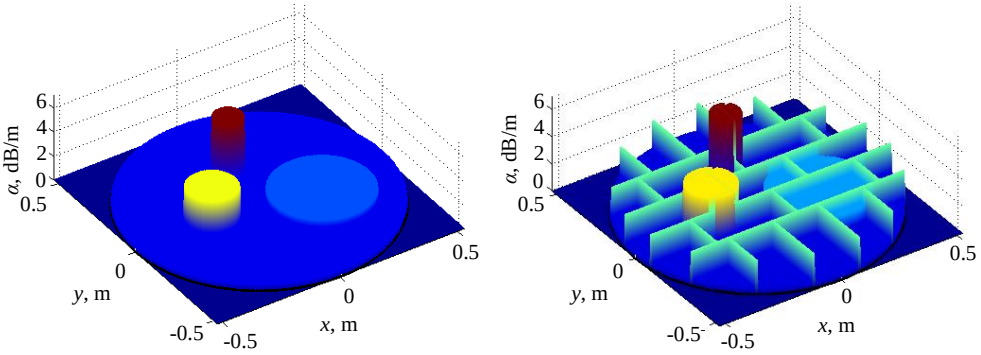

a) b)

Fig. 4.2.2. The distribution of attenuation in the model of the storage tank floor when: the ambient attenuation in the non-corroded areas is 0.5 dB/m and there is no attenuation in welds (a), the ambient attenuation in the non-corroded areas is 0.5 dB/m and the attenuation in the welds is 2 dB/weld (b)

The value of projections is calculated separately for each path between the transmitter $\{x_{\mathrm{Tr}}(m), y_{\mathrm{Tr}}(m)\}$ and the receiver $\{x_{\mathrm{Rv}}(n,m), y_{\mathrm{Rv}}(n,m)\}$. The procedure is:

1. The distance between the transmitter and the receiver is estimated:

$$d_{\mathrm{TR}}(n,m) = \sqrt{\left(x_{\mathrm{Tr}}(m) - x_{\mathrm{Rv}}(n,m)\right)^2 + \left(y_{\mathrm{Tr}}(m) - y_{\mathrm{Rv}}(n,m)\right)^2}\ ; \tag{4.2.3}$$

2. The angle of the path in the coordinate system is calculated:

$$\theta_{\mathrm{TR}}(n,m) = \arctan\left[\frac{y_{\mathrm{Tr}}(m) - y_{\mathrm{Rv}}(n,m)}{x_{\mathrm{Tr}}(m) - x_{\mathrm{Rv}}(n,m)}\right]. \tag{4.2.4}$$

3. The path between the transmitter and the receiver is sampled:

$$\begin{aligned} x_{\mathrm{TR}}(n,m,k) &= (k-1)\cdot \Delta x_{\mathrm{TR}} \cdot \cos\left(\theta_{\mathrm{TR}}(n,m)\right) + x_{\mathrm{Tr}}(m), \\ y_{\mathrm{TR}}(n,m,k) &= (k-1)\cdot \Delta x_{\mathrm{TR}} \cdot \sin\left(\theta_{\mathrm{TR}}(n,m)\right) + y_{\mathrm{Tr}}(m) \end{aligned} \tag{4.2.5}$$

where Δx_{TR} is the linear path sampling step; $k = 1 \div N_{\mathrm{pth}}$; $N_{\mathrm{pth}} = \dfrac{d_{\mathrm{TR}}(n,m)}{\Delta x_{\mathrm{TR}}} + 1$

4. The values of attenuation $\alpha_{\mathrm{pth}}(n,m,k)$ at points $\{x_{\mathrm{Tr}}(n,m,k); y_{\mathrm{Tr}}(n,m,k)\}$ are obtained from the attenuation map $\alpha_{\mathrm{T}}(n_{\mathrm{T}}, m_{\mathrm{T}})$ using two-dimensional linear interpolation.
5. The projections as the total losses along the path from the modelled attenuation map are obtained by integrating all interpolated attenuation values along the $\alpha_{\mathrm{pth}}(n,m,k)$ path:

$$A_{\mathrm{M}}(n,m) = \Delta x_{\mathrm{Tr}} \cdot \sum_{k=1}^{N_{\mathrm{pth}}} \alpha_{\mathrm{pth}}(n,m,k). \tag{4.2.6}$$

In order to investigate how accurate is the reconstruction of attenuation distribution and the parameters it depends on, the modelling using the developed tank floor model has been carried out and is presented in the next section.

4.3 An investigation of the performance of a reconstruction algorithm

In order to investigate the possibilities of the developed reconstruction algorithm, investigations were carried out using the developed storage tank floor model. The investigation was carried out for two specific cases of a storage tank floor – by assuming that there is no attenuation in the weld, andwhen attenuation in the weld is present concurrently introducing 3 circular zones with high attenuation values to represent an increase in attenuation of UGW as the primary effect of corrosion in the proposed model. The distribution of these zones in the storage tank floor model for both analysed cases are presented in Fig. 4.3.1.

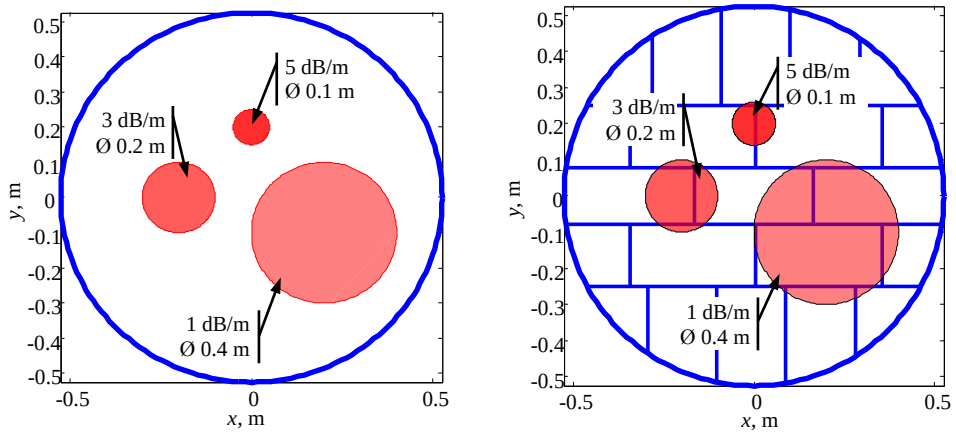

Fig. 4.3.1. The storage tank floor model with corroded areas with higher attenuation values when there is no attenuation in weld (a) and when there is attenuation in weld (b)

Firstly, the reconstruction of attenuation distribution in the storage tank floor was carried out by assuming that the attenuation in the plate is very low (0.05 dB/m) in non-corroded zones and there is no attenuation in the welds (Fig. 4.3.1a). Using the presented model, 360 projections have been calculated by positioning the transducer at positions around the storage tank floor model with the step of 1°. The projections were calculated by assessing the attenuation at 180 virtual receiver positions, situated along the circumferential edge of the tank floor, for each position of the transmitter. The projections were calculated according to the description presented in section 4.1. The projections were then filtered according to the description presented earlier. The reconstructed images of spatial attenuation distribution in the form of a 3D image and a C-scan image are presented in Fig. 4.3.2.

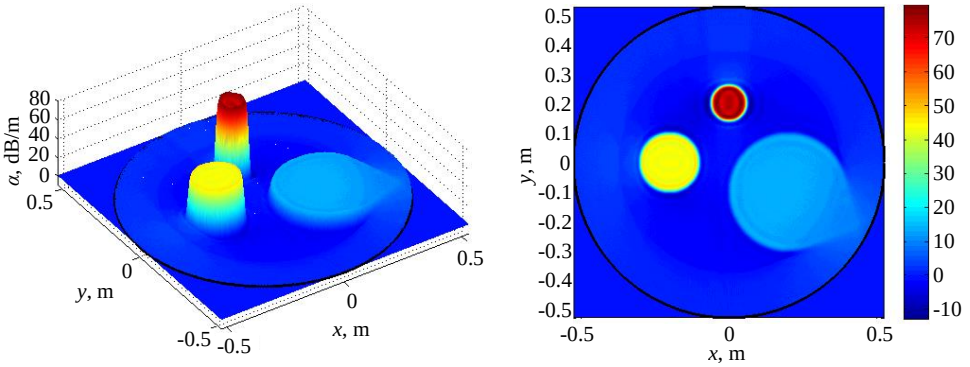

a) b)

Fig. 4.3.2. The reconstructed distribution of the attenuation in the storage tank floor when there is no attenuation in the weld in the form of a) a 3D image (a) and b) a C-scan image (b)

It can be observed that the spatial distribution of the defects fits very well with the original positions in the model. However, the reconstructed absolute amplitudes possess some arbitrary values not related to the attenuation determined in the model. In order to overcome this problem, an additional step in the reconstruction algorithm was proposed. It is based on the hypothesis that the original projection should coincide with the projections from the reconstructed attenuation field. It means that a correction scheme should exist, which would enable to modify the reconstructed attenuation field in a such way that the projection obtained from the reconstructed image fit with each other. The original projection $A_{\mathrm{M}}(n,m)$ and projection from the reconstructed image $A_{\mathrm{M,Rec}}(n,m)$ were fitted following these steps:

1. Linear correction was assumed. It means that coefficients k_1 and k_2 exist for each projection:

$$A_{\mathrm{M}}(n,m) = A_{\mathrm{M,Rec}}(n,m)\cdot k_1 + L(n,m_k)\cdot k_2\,, \tag{4.3.1}$$

where $L(n,m_k)$ is the path between the transmitter and the receiver, m_k is the projection selected for optimisation.

2. Coefficients k_1 and k_2 are determined using optimisation. The target function is:

$$F(k_1,k_2) = \arg\min_{k_1,k_2}\left\{\left[A_{\mathrm{M}}(n,m) - A_{\mathrm{M,Rec}}(n,m)\cdot k_1 + L(n,m_k)\cdot k_2\right]^2\right\}. \tag{4.3.2}$$

3. The optimisation was performed separately for each projection and the mean value of the correction coefficients were used. The investigation demonstrated that the fitting can be performed using only several, better perpendicular projections and the obtained coefficients give sufficiently good results. Finally, the image after tomographic reconstruction was corrected according to:

$$\alpha_{\mathrm{tf,cor}}(n_x,n_y) = \alpha_{\mathrm{tf}}(n_x,n_y)\cdot k_1 + k_2\,. \tag{4.3.3}$$

By using the proposed correction in the tomographic reconstruction algorithm, the reconstructed attenuation distribution in the storage tank floor model in the form of 3D and C-scan images are presented in the Fig. 4.3.3.

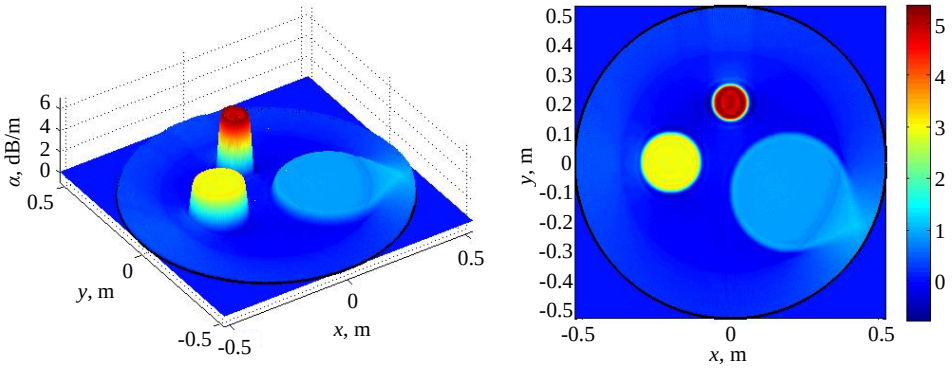

a) b)

Fig. 4.3.3. The reconstructed corrected distribution of attenuation in the storage tank floor when there is no attenuation in weld in the form of a 3D image (a) and a C-scan image (b)

It can be noticed that the positions of all introduced zones are reconstructed correctly. The shape reconstruction is different. The shape of two zones was reconstructed well, however the biggest one has some distortions on the side oriented to the edge of the storage tank floor. It is related to the fact that the middle zones are covered completely by all projections and beam paths. In contrary, the part of the biggest (Ø0.4 m diameter) zone is not covered at least by some of the projections. It is related to the fact that by using fan-beam data acquisition geometry, the best reconstruction quality is obtained within the sub-volume that is probed by all of the projections. This sub-volume is probed by the two outermost rays as the fan formed by single transmitting transducer. In the case of circular storage tank floor, this sub-volume would lie within a circle that is concentric with the circle of tank floor radius R but having a reduced radius $R\sin\theta$, where θ is the marginal receiver angle with respect to the central ray [171].

Another question is how accurately the value of attenuation is reconstructed. The reconstruction accuracy was estimated by calculating these parameters:

1. Mean value of the reconstructed attenuation:

$$\overline{\alpha}_{\text{cd,rec}} = \frac{1}{K}\sum_{k=1}^{K}\alpha_{\text{cd,rec}}^{k}\,, \tag{4.3.4}$$

where $\alpha_{\text{cd,rec}}$ is the reconstructed attenuation value of the circular defect; $k = 1 \div K$, K is the number of points in virtual tank floor enclosed by a defect.

2. Standard deviation of the reconstructed attenuation:

$$\sigma_{\alpha_{\text{cd,rec}}} = \sqrt{\frac{\sum_{k=1}^{K}\left(\alpha_{\text{cd}}^{k} - \alpha_{\text{cd,rec}}^{k}\right)^{2}}{K-1}}\,, \tag{4.3.5}$$

where α_{cd} is the assigned attenuation value in the corroded area of the storage tank model.

3. Mean absolute error of the reconstructed attenuation in the corroded area:

$$\overline{\Delta}_{\alpha_{\text{cd,rec}}} = \frac{1}{K}\sum_{k=1}^{K}\left(\alpha_{\text{cd}}^{k} - \alpha_{\text{cd,rec}}^{k}\right). \tag{4.3.6}$$

4. Mean relative error of the reconstructed attenuation in the corroded area:

$$\delta_{\alpha_{\text{cd,rec}}} = \frac{1}{K}\sum_{k=1}^{K}\frac{\alpha_{\text{cd}}^{k} - \alpha_{\text{cd,rec}}^{k}}{\alpha_{\text{cd,rec}}^{\text{k}}}\cdot 100\%\,. \tag{4.3.7}$$

The average value of the reconstructed attenuation, standard deviation, mean absolute and relative error values are presented in Table 4.3.1.

Table 4.3.1. A comparison of defect reconstruction accuracy when there is no attenuation in weld in a tank floor model

Zone	α_{cd}, dB/m	$\overline{\alpha}_{\text{cd,rec}}$, dB/m	$\sigma_{\alpha_{\text{cd,rec}}}$, dB/m	$\overline{\Delta}_{\alpha_{\text{cd,rec}}}$, dB/m	$\delta_{\alpha_{\text{cd,rec}}}$, %
1	5.05	4.98	0.264	-0.067	1.35
2	3.05	2.99	0.104	-0.061	2.04
3	1.05	0.96	0.052	-0.094	9.77

The modelling results listed in the Table 4.3.1 show that the overall true value of attenuation enclosed by circular defects was reconstructed with the relative error of up to 2%. However, the attenuation distribution for the largest Ø0.4 m diameter defect (zone 3) was reconstructed with the relative error of 9.77%, which was conditioned by the fact that the defect is not covered completely by all projections and beam paths. Hence, the distribution of the reconstructed attenuation in non-corroded areas of the storage tank floor and the distribution of absolute error in dB/m in reconstruction of attenuation distribution are presented in Fig. 4.3.4 and Fig. 4.3.5, respectively. The figures present that the highest reconstruction errors occur outside the sub-volume of radius $R\sin\theta$ because of incomplete area coverage of fan-beam data acquisition geometry. At the same time, the errors in the zones enclosed by circular defects are conditioned because of the difference between real and reconstructed values in attenuation profile which mainly is conditioned by the tomographic filter function.

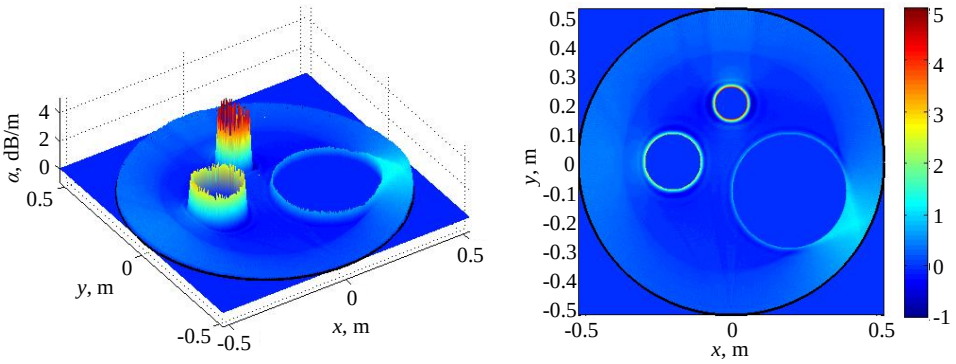

a) b)

Fig. 4.3.4. The distribution of reconstructed attenuation in the non-corroded part of the storage tank floor when there is no attenuation in weld in the form of a 3D image (a) and a C-scan image (b)

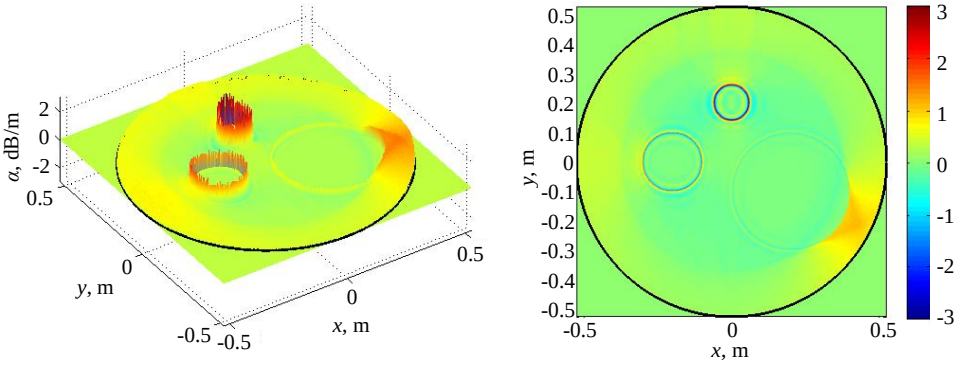

Fig. 4.3.5. The distribution of the absolute error in the reconstructed attenuation of the tank floor when there is no attenuation in weld in the form of a 3D image (a) and a C-scan image (b)

However, the storage tank floor is a much more complicated object than it was presented in Fig. 4.3.1a and the overall profile of attenuation distribution would be distorted by multiple welds in the tank floor. Therefore, in order to test the accuracy of the proposed tomographic reconstruction algorithm, the modelling of a storage tank floor with attenuation in welds and in the areas with increased attenuation value was performed by using the model presented in Fig. 4.3.1b, as well. The images of the storage tank floor reconstructed by using the proposed tomographic reconstruction method in the form of 3D and C-scan images are presented in Fig. 4.3.6. Furthermore, the average value of the reconstructed attenuation, standard deviation, mean absolute error and mean relative error values in the case of the storage tank floor model with attenuation in the weld are presented in Table 4.3.2. The distribution of the reconstructed attenuation in non-corroded areas of the storage tank floor and the distribution of the absolute error in dB/m of the corroded areas reconstruction are presented in Fig. 4.3.7 and Fig. 4.3.8, respectively.

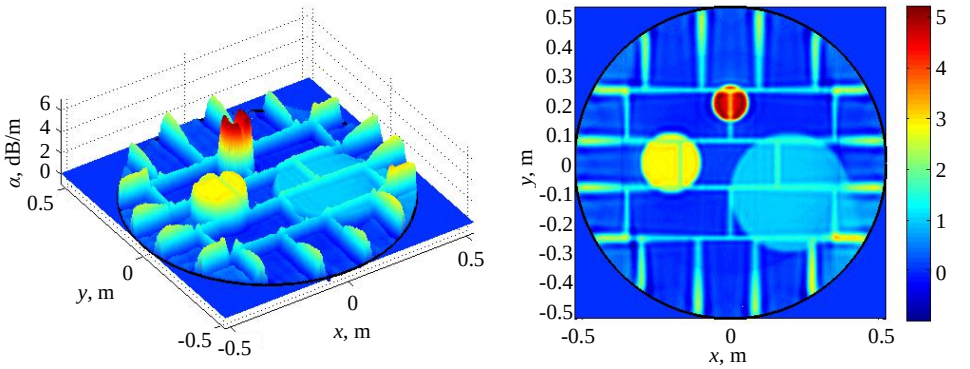

Fig. 4.3.6. The reconstructed corrected distribution of attenuation in the storage tank floor when there is attenuation in weld in the form of a 3D image (a) and a C-scan image (b)

Table 4.3.2. A comparison of defect reconstruction accuracy when there is attenuation in the weld in a tank floor model

Zone	α_{cd} , dB/m	$\overline{\alpha}_{cd,rec}$, dB/m	$\sigma_{\alpha_{cd,rec}}$, dB/m	$\overline{\Delta}_{\alpha_{cd,rec}}$, dB/m	$\delta_{\alpha_{cd,rec}}$, %
1	4.62	4.3	0.661	-0.32	7.43
2	2.92	2.73	0.232	-0.192	7.04
3	1.14	1.03	0.212	-0.114	11.05

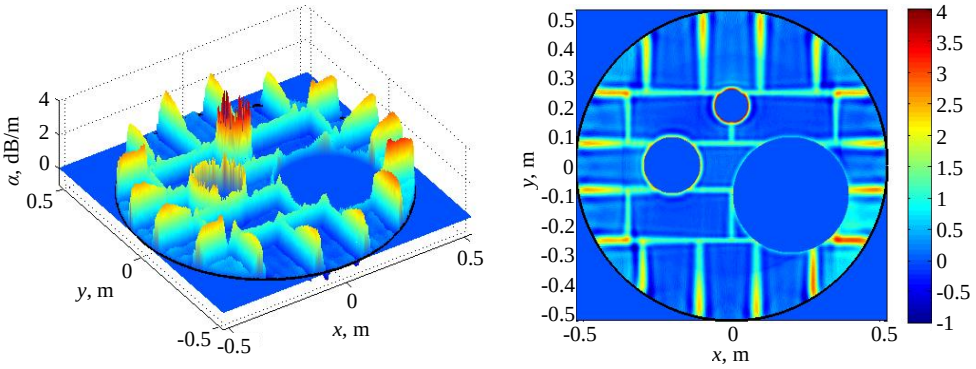

Fig. 4.3.7. The distribution of the reconstructed attenuation in the non-corroded part of the storage tank floor when there is attenuation in the weld in the form of the 3D image (a) and the C-scan image (b)

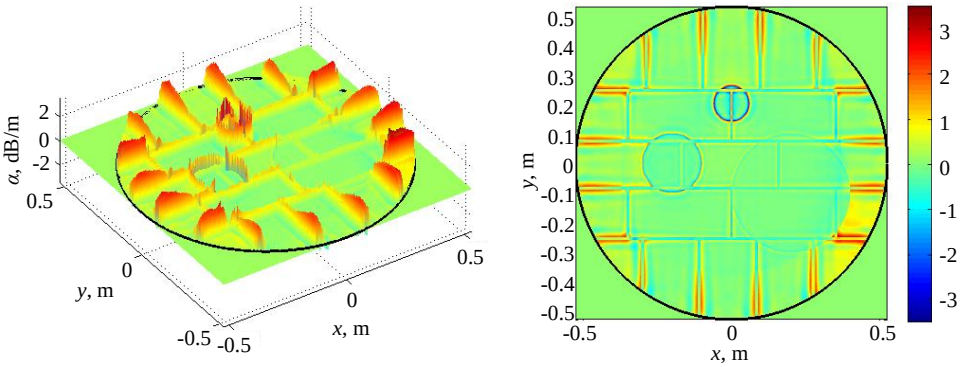

Fig. 4.3.8. The distribution of absolute error in the reconstructed attenuation of the storage tank floor when there is attenuation in the weld in the form of the 3D image (a) and the C-scan image (b)

The results indicate that the introduced losses in welds in the storage tank floor model distort the profile of spatial attenuation distribution in the areas enclosed by circular defects. At the same time, the modelling demonstrates that the true value of attenuation in the areas of circular defects were reconstructed with higher relative error, which for the presented cases varied in ranges of 7%–11%. Such increase in the reconstruction error for the presented tank floor is mainly conditioned by the sharp

change of attenuation and error at the reconstructed attenuation profile at the finite width weld.

An analysis of performance of the proposed tomographic reconstruction algorithm demonstrated that, in general, the reconstruction of the spatial distribution of attenuation observing the true values of attenuation can be performed. The presented models reveal that the spatial attenuation distribution in the storage tank floor model could be reconstructed with the relative error of 1%–2%. However, if the defect is located outside of the sub-volume of radius $R\sin\theta$ and there are sharp changes in the attenuation distribution profile due to introduced welds, the mean relative reconstruction error might reach 7%–11%.

4.4 An analysis of the systematic error in attenuation distribution reconstruction

In general, the accuracy and quality of the ray tracing-based tomographic reconstruction method is mainly conditioned by the density of the rays passing through the defect and the function of the used tomographic filter. Therefore, to compare the measurement results with the theoretical values of attenuation distribution in the defective zones of the storage tank floor, an analysis was carried out by using the models presented in Fig. 4.3.1. The density of the rays or angular sampling of the object in the tomographic reconstruction is mainly caused by the number of acquired projections and the number of receivers allocated on the opposite circumferential edge of the storage tank floor for each transmitter position. Therefore, the investigation of reconstruction accuracy was performed by changing the angular sampling of the transmitters along all the circumferential edge of the tank floor in a such way that the angle between separate transmitter positions varies from 1° to 4°, thus resulting in a number of totally acquired projections. At the same time, the number of receivers at each transmitter position in the 180° section of the storage tank floor was changed in a such way that the angle between separate receiver positions varies from 1° to 2°. Herewith, the accuracy of the tomographic reconstruction of attenuation distribution is strongly dependent not only on the angular sampling of the object but also on the corrected tomographic filter $H_{\mathrm{Tc}}(f_{\mathrm{x}})$ function, which in general is used to reduce high frequency reverberations (noise) in reconstructed images. In this case, the investigation was performed by using a corrected tomographic filter $H_{\mathrm{Tc}}(f_{\mathrm{x}})$ at different cut-off frequencies f_{sf0} of a smoothing (low-pass) filter (equations 4.1.3 and 4.1.4), thus removing all spatial frequency components in the reconstructed image above a certain value of spatial frequency f_{x}. A graphical representation of frequency responses of the corrected tomographic filter $H_{\mathrm{Tc}}(f_{\mathrm{x}})$ at different cut-off frequencies f_{sf0} of a smoothing filter are presented in Fig. 4.4.1.

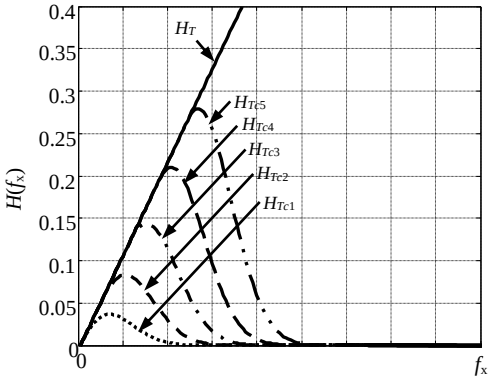

Fig. 4.4.1. The frequency responses of tomographic filters where H_T – ramp filter, corrected tomographic filters: $H_{Tc1}(f_{sf0} = 1/15f_x)$, $H_{Tc2}(f_{sf0} = 2/15f_x)$, $H_{Tc3}(f_{sf0} = 1/5f_x)$, $H_{Tc4}(f_{sf0} = 4/15f_x)$, $H_{Tc5}(f_{sf0} = 1/3f_x)$,

The accuracy of attenuation distribution reconstruction in the tank floor zones with increased attenuation was evaluated by calculating the mean absolute error of the reconstructed attenuation in corroded areas according to equation 4.3.6. The results of the mean absolute error distribution in dependence on the angular sampling of tank floor (number of acquired projections and number of receivers in the receiving subset) and the bandwidth of the corrected tomographic filter $H_{Tc}(f_x)$, in the case of tank floor model without attenuation in the welds (Fig. 4.3.1a) and in case of attenuation in the welds (Fig. 4.3.1b) are presented in Fig. 4.4.2 and Fig. 4.4.3, respectively.

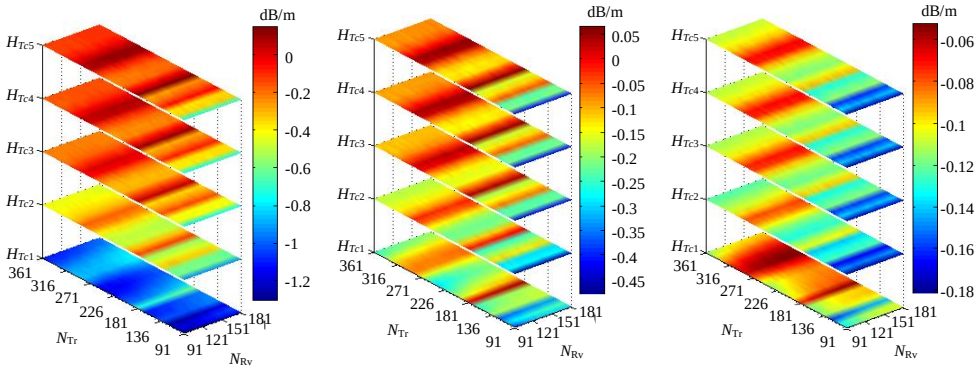

a) b) c)

Fig. 4.4.2. The distribution of absolute error in the tank floor model without attenuation in the welds in the case of different angular model sampling and different tomographic filter bandwidth for the: Ø0.1 m 5 dB/m (a), Ø0.2 m 3 dB/m (b), Ø0.4 m 1 dB/m defects (c)

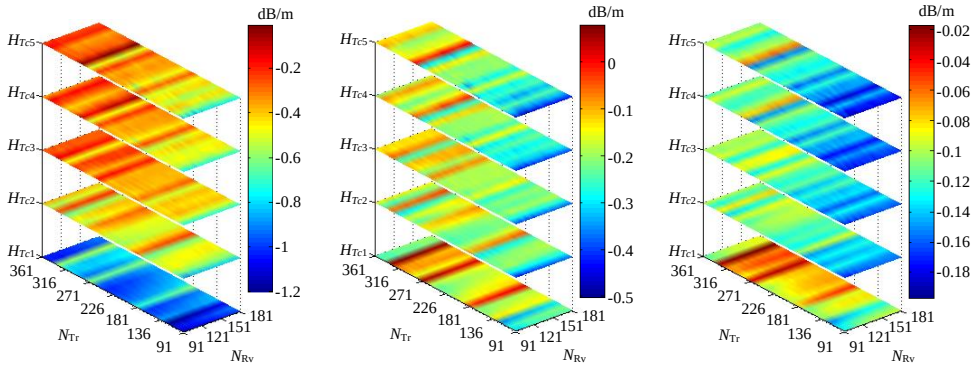

a) b) c)

Fig. 4.4.3. The distribution of absolute error in the tank floor model with introduced attenuation in the welds in the case of the different angular model sampling and different tomographic filter bandwidth for the: Ø0.1 m 5 dB/m (a), Ø0.2 m 3 dB/m (b), Ø0.4 m 1 dB/m defects (c)

Fig. 4.4.2 and Fig. 4.4.3 prove that the function of the tomographic filter used to filter the acquired projection has the most significant influence on the accuracy of reconstruction. In this instance, the mean absolute error increases with the limiting of the bandwidth of the corrected tomographic filter in both presented tank floor cases. Such dependence of absolute error on the function of the corrected tomographic filter could be clearly observed in the presented tank floor for the reconstruction of attenuation distribution for 0.1 m diameter defect which has a sharp attenuation change profile. In general, the corrected tomographic filter reduces the high frequency components under a certain value of spatial frequency and causes blurring in the reconstructed image. In this instance, the limiting of spatial frequency results in an error in the shape (attenuation profile) reconstruction and causes an increase of absolute error in attenuation value estimation.

4.5 An analysis of tomographic reconstruction in the model of calibration

The previous sections have demonstrated the applicability of the proposed ultrasonic tomographic reconstruction method for the true values of attenuation spatial distribution reconstruction in a storage tank floor. However, the performance of the proposed method was tested by assuming that there are some large zones (represented by circular defects) with increased attenuation values in the model which do not match the real status of a scaled-down storage tank mock-up in the laboratory. In this regard, it is appropriate to examine the proposed tomographic reconstruction method by using a model corresponding to the specially developed test sample with artificial defects. In general, corrosion defects are simulated in two ways. The first one is by creating large zones with reduced thickness. Such artificial defects simulate the reduction in wall thickness in the zone affected by corrosion [70–74]. The second way is when a set of flat bottom holes is created in a certain area to simulate UGW scattering due to relatively concentrated non-uniform corrosion damage [73, 75, 76]. Based on these assumptions, the model and test sample with defect distribution presented in Fig. 4.5.1

was created. In order to imitate different corrosion rates on the sample, the artificial defects were assumed to have different the depth profiles whose cross-sections are presented in Fig. 4.5.2.

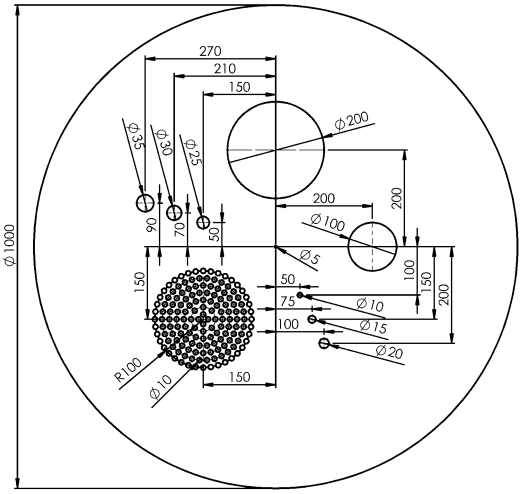

Fig. 4.5.1. A schematic layout of defect distribution in the used model

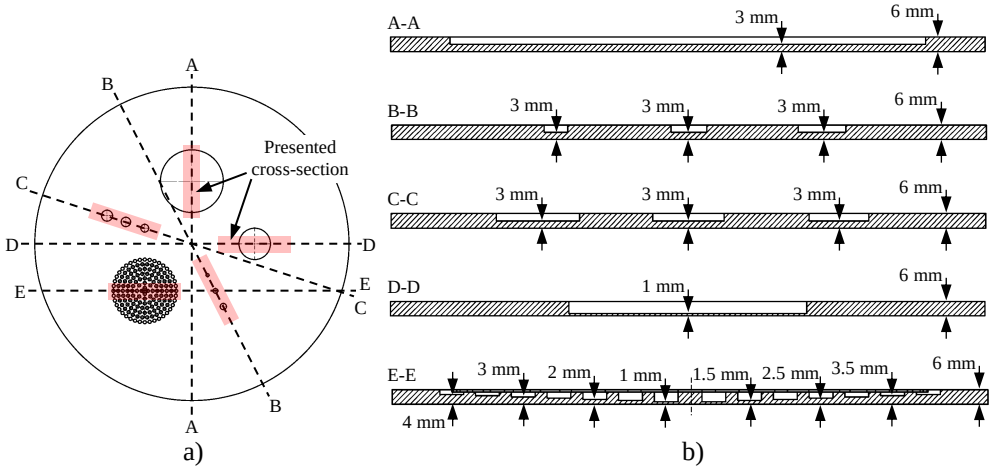

Fig. 4.5.2. The model used for investigating the performance of UGW tomographic reconstruction (a) and the cross-section through the centre of the defects to illustrate the variation of defect depth (b)

Another group of parameters that needs to be assigned (besides geometry and position of defects) are the possible losses of UGW in the model. In practice, those losses occur at the interaction of the incident wave with artificial defects. In this respect, the test sample serves as a waveguide for UGW propagation and reflection signals are generated mainly due to the mismatch of acoustical impedance at the notch (defect) of the acoustic waveguide which results in reflection and transmission of the ultrasonic waves as shown in Fig. 4.5.3 [172, 173].

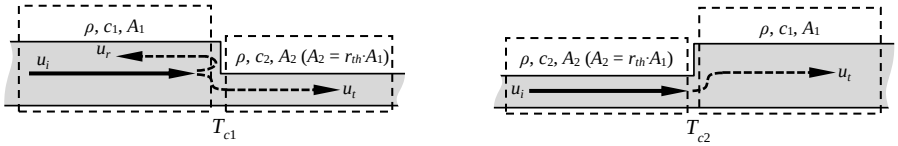

Fig. 4.5.3. Reflection (a) and transmission (b) of the wave at waveguide junction

In this regard, acoustic impedance can be calculated as follows [172, 173]:

$$Z = \frac{\rho c}{A}, \tag{4.5.1}$$

where ρ is the material density, c is the velocity in material, A is the cross-section area of the acoustic waveguide. Based on ultrasonic impedance equation, the wave transmission coefficients T_{c1} and T_{c2} at waveguide junction (Fig. 4.5.3) can be expressed as follows:

$$T_{c1} = \frac{2Z_2}{Z_1 + Z_2} = \frac{2\rho c_2}{r_{th}\rho c_1 + \rho c_2}, \tag{4.5.2}$$

$$T_{c2} = \frac{2Z_1}{Z_1 + Z_2} = \frac{2\rho c_1}{\rho c_1 + \rho c_2 / r_{th}}, \tag{4.5.3}$$

where Z_1 is the impedance of the cross-section area A_1, Z_2 is the impedance of the cross-section area A_2, ρ is the material density, r_{th} is the thickness ratio in cross-section of the waveguide, c_1 and c_2 are UGW velocity in the cross-section areas A_1 and A_2 under constant frequency value, respectively. It assumed that the losses on the defect depend on the overall product of $T_{c1} \cdot T_{c2}$:

$$\alpha = -20\lg\left(T_{c1} \cdot T_{c2}\right). \tag{4.5.4}$$

However, such assumption in the model would postulate that different diameter but equally deep defects would be assigned with the same attenuation value for small and large diameter defects which is not completely true, as the low frequency waves are diffracted around the obstacle. To overcome it, the value of attenuation for the presented circular defects was assumed to be dependent on the diameter of defect:

$$\alpha_{cd} = \alpha \cdot d_{cd}, \tag{4.5.5}$$

where d_{cd} is the diameter of the artificial defect. In the case of the pit cluster-type defect, the values of attenuation were acquired by multiplying the assigned attenuation value for the current depth pit by the equivalent diameter defect enclosed by pits at specific depth:

$$\alpha_{cd} = \alpha \cdot \left(d_{cd} + d_{cd,p}\right), \tag{4.5.6}$$

where $d_{cd,p}$ is the equivalent circular defect diameter enclosed by pits at particular depth. In this instance, the observed attenuation value on the defect would be mainly conditioned by the velocity of the symmetric S_0 UGW mode propagating through cross-sections A_1 and A_2. Therefore, the possible losses were examined at different

frequency points of the UGW. The analysis was performed by using the attenuation map predicted at frequencies f_1 = 110 kHz, f_2 = 200 kHz, f_3 = 240 kHz. The dispersion curves of the UGW in a 6 mm thick stainless steel plate and frequencies at which possible losses due to the reduction of thickness were predicted are presented in Fig. 4.5.4.

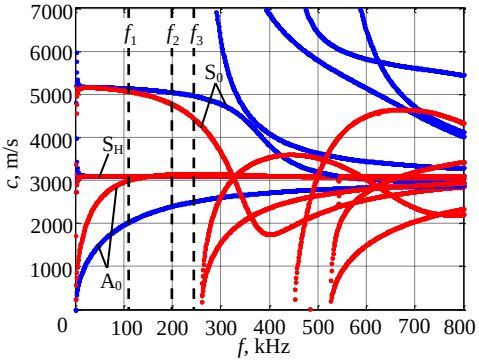

Fig. 4.5.4. The UGW phase (blue) and group (red) velocities dispersion curves for the 6 mm thick stainless steel plate

Based on the previous assumptions, the possible UGW losses on the defects were calculated to create the attenuation map and the final reconstructed images of attenuation distribution in the proposed model were calculated. As an example, the assumed attenuation distribution map in the proposed sample at 110 kHz frequency is presented in Fig. 4.5.5. The assigned attenuation values in the model at frequencies f_1 = 110 kHz, f_2 = 200 kHz, f_3 = 240 kHz are presented in Table 4.5.1. The reconstructed spatial distribution of attenuation in the model are presented in Fig. 4.5.6–Fig. 4.5.8, respectively.

Table 4.5.1. Attenuation on defects at different frequency points of the UGW

Defect diameter d_{cd}, mm	Defect depth h_{cd}, mm	Assigned attenuation value α_{cd}, dB/m		
		at 110 kHz	at 200 kHz	at 240 kHz
10	3	1.1	1.2	1.4
15	3	1.6	1.8	2.1
20	3	2.1	2.4	2.8
25	3	2.7	3.1	3.5
30	3	3.2	3.7	4.2
35	3	3.7	4.3	4.9
100	5	63.1	67	70.9
200	3	21.3	24.4	28
200 (pit cluster)	2	22.8	27.5	33.3
	2.5	33.9	39.8	46.8
	3	45.7	52.5	60.1
	3.5	56.7	63.7	71.4
	4	64.3	70.7	77.6
	4.5	55.5	60	64.6
	5	44.2	46.9	49.6

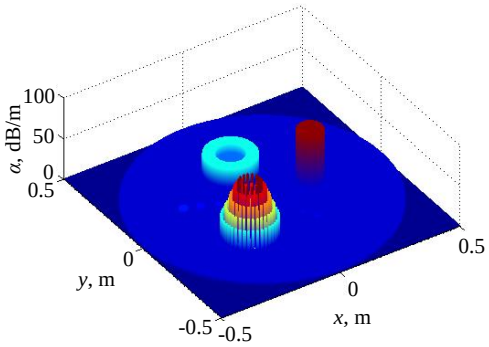

Fig. 4.5.5. The distribution of attenuation in the model of calibration when f_1 = 110 kHz

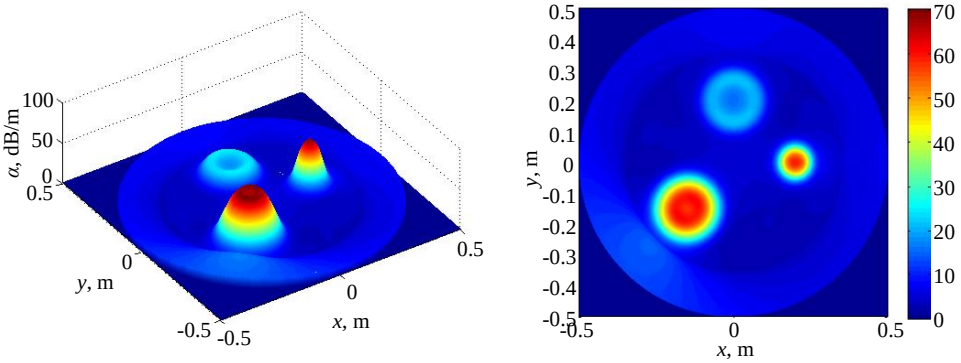

a) b)

Fig. 4.5.6. The reconstructed distribution of attenuation in the proposed model when f_1 = 110 kHz in the form of a 3D image (a) and a C-scan image (b)

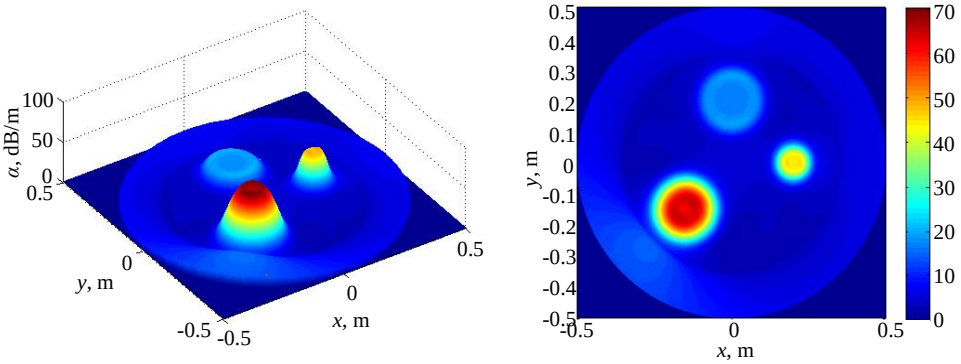

a) b)

Fig. 4.5.7. The reconstructed distribution of attenuation in the proposed model when f_2 = 200 kHz in the form of a 3D image (a) and a C-scan image (b)

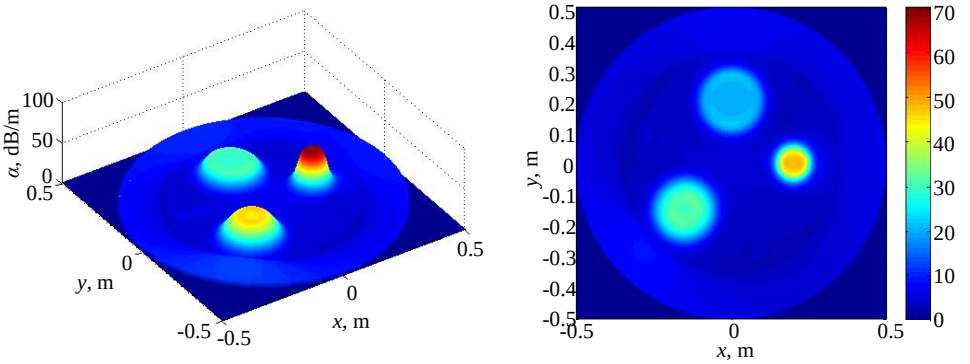

a) b)

Fig. 4.5.8. The reconstructed distribution of attenuation in the proposed model when f_3 = 240 kHz in the form of a 3D image (a) and a C-scan image (b)

In general, the results presented in Fig. 4.5.6–Fig. 4.5.8 demonstrate that the overall value of attenuation caused by defects varies due to the change of acoustic impedance at the defective region with the frequency of UGW. The simulation by using the developed model of calibration imply that only large areas of defects could be reconstructed with a high spatial resolution. Meanwhile, only some weak indications of small diameter defects could be observed in the reconstructed attenuation map. In this instance, the modelling demonstrated that attenuation in larger (Ø100 mm, Ø200 mm and Ø200 mm pit cluster) defective areas increases with the frequency of the UGW. It was observed that the mean value of attenuation in the region enclosed by Ø100 mm defect is 32.3 dB/m, by Ø200 mm defect – 13.6 dB/m, by Ø200 mm pit cluster defect – 15.5 dB/m at 110 kHz frequency. Meanwhile, at 200 kHz frequency those values were: by Ø100 mm defect – 36.2 dB/m, by Ø200 mm defect – 15.5 dB/m, by Ø200 mm pit cluster defect – 17.4 dB/m. And at 240 kHz frequency: by Ø100 mm defect – 35 dB/m, by Ø200 mm defect – 16.1 dB/m, by Ø200 mm pit cluster defect – 19.4 dB/m.

4.6 Conclusions of the Chapter 4

1) A modified UGW transmission tomography algorithm was developed enabling to reconstruct the true values of attenuation and their spatial distribution in a storage tank floor. The reconstruction of true values of attenuation was achieved by introducing an additional stage into the algorithm based on optimization.
2) The proposed ultrasonic transmission tomography algorithm was verified using the developed tank floor model which enables to consider the average attenuation in plate, attenuation in the corroded zones and losses on the weld. The results demonstrate that using the tank floor model developed with no losses in the welds, a 2% relative error of true value of attenuation spatial distribution reconstruction is achievable. Meanwhile, the results of the reconstruction of spatial attenuation distribution in the tank floor model with welds demonstrated an increase of relative error to 7% in the reconstruction

of true values. Such increase in relative reconstruction error could be explained by the sharp attenuation profile change at the intersection of corroded areas and welds.

3) The test on the developed model of the calibration sample demonstrated that defects larger than the wavelength are detected and indicated.

5. EXPERIMENTAL INVESTIGATION OF TOMOGRAPHIC RECONSTRUCTION OF ULTRASONIC GUIDED WAVES

The objective of this chapter is the experimental verification of the proposed ultrasonic tomographic reconstruction method for the reconstruction of true values of attenuation spatial distribution. To achieve this, the experimental investigation of the UGW propagation was carried out by using a specially developed circular test sample with artificial defects of known parameters to represent the reduction of object thickness as the primary effect of corrosion. Additionally, the experimental research on UGW propagation in the specially developed scaled-down storage tank mock-up, corresponding to the 3D model presented in Section 2.5, was carried out and the measurement results are presented.

5.1 An investigation of the developed tomographic reconstruction algorithm on a calibrated sample

The purpose of the research is the experimental investigation and verification of the proposed UGW tomographic reconstruction method for detecting defects and reconstructing the spatial attenuation distribution. As it was mentioned in Section 1.1, in most cases the applicability of the UGW testing techniques is verified on the samples with known defect parameters. From this point, the discontinuities in the test objects for UGW inspection are represented by simple-shaped defects, which are assumed to have generic application for the propagation of guided waves and the representation of defects, such as corrosion. For this purpose, the special Ø1 m test sample, corresponding to the model presented in Section 4.5, made from 6 mm thick stainless steel alloy with a set of artificial defects was manufactured. The geometry of the developed and investigated sample is presented in Fig. 5.1.1a. Based on the schematic layout presented in Fig. 4.5.1, the artificial defects were made by milling circular flat-bottomed part-thickness holes: Ø100 mm and 83% thickness reduction, Ø200 mm and 50% thickness reduction, and Ø10 mm, Ø15 mm, Ø20 mm, Ø25 mm, Ø30 mm, Ø35 mm with 50% thickness reduction, respectively. However, realistic corrosion can be far more complex and irregular in both the shape and depth profile. In this study, a non-uniform Ø200 mm diameter defective area with artificial thickness reduction varying from 17% to 83% to represent a closer match to the shape of corrosion and add considerable complexity to UGW propagation was made. The presented pit cluster consists of multiple part-thickness flat-bottomed Ø10 mm holes whose depth gradually increases (from 2 mm to 5 mm) approaching the centre of the defective area. The cross-section of the area with varying-depth pit cluster is presented in Fig. 5.1.1b.

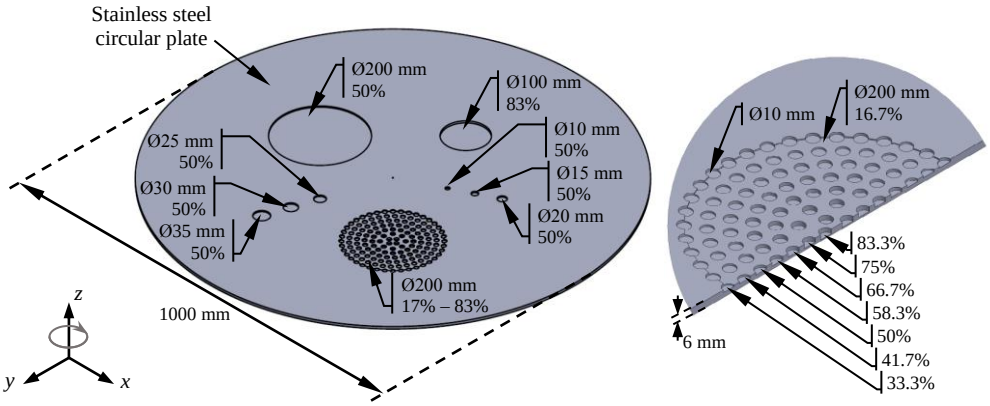

Fig. 5.1.1. Circular Ø1 m and 6 mm thick stainless steel sample used for the experimental investigation of UGW tomography (a) and the cross-section of the varying depth defects representing the pit cluster (b)

The experimental investigation on UGW propagation and its interaction with artificial defects in the presented circular stainless steel sample was performed using the experimental set-up presented in Fig. 5.1.2. The TecScan Systems Inc. TCIS-3000 11-axis large industrial scanner was used as a control instrument for measurements. The investigated stainless steel sample with artificial defects and the measurement instrumentation are presented in Fig. 5.1.3.

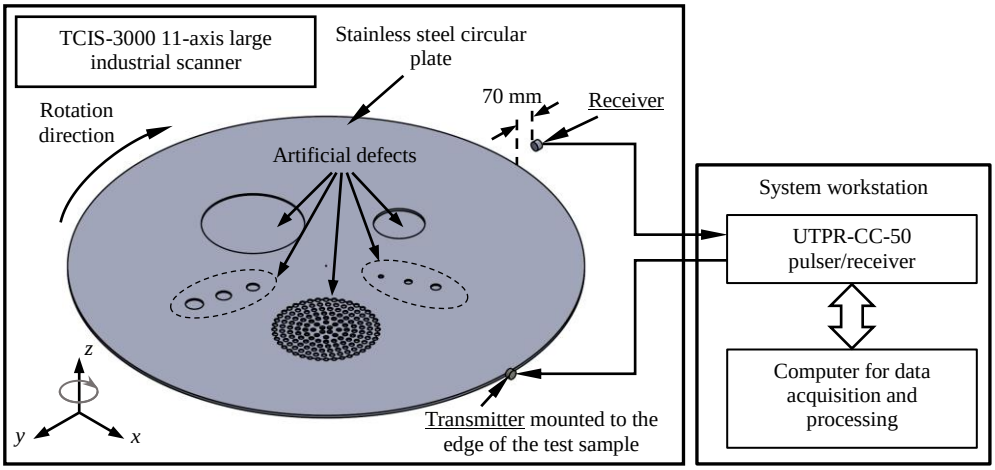

Fig. 5.1.2. The experimental set-up used for the investigation of the proposed tomographic reconstruction method

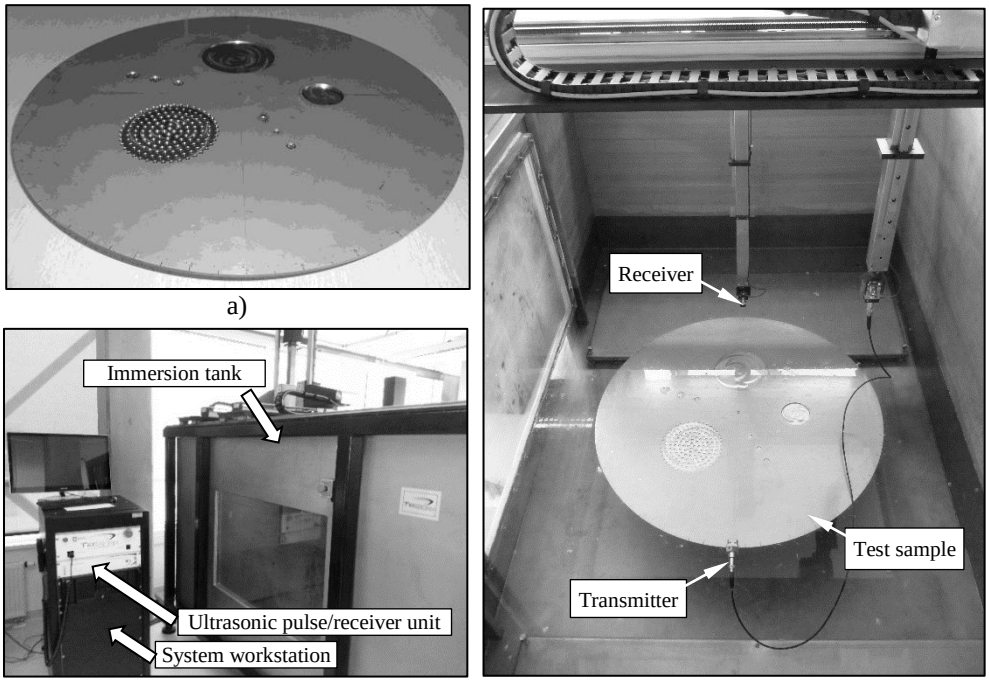

a) b) c)

Fig. 5.1.3. The investigated 6 mm thick stainless steel sample with artificial defects (a), TCIS-3000 11-axis large industrial scanner (b), the experimental stand (c)

During the experimental measurements, the investigated stainless steel sample was placed into the immersion tank filled with water and fixed on the turn table. The sample was fixed via Ø5 mm through-thickness hole to the mounting base of Ø115 mm. Thus, it can be assumed that an additional defect is situated at the centre of the sample. The measurements through water minimise the acoustical contact variation which is essential in the amplitude measurements. At the same time, water acoustical coupling of the object ensures that practically only symmetric S_0 UGW mode is excited in the presented stainless steel sample. Meanwhile, asymmetric A_0 wave mode possess essentially higher leakage losses into the surrounding environment and is suppressed. The excitation and reception of the UGW was performed using the Panametrics-NDT ultrasonic immersion-type V318-SU transducers with the central frequency of 450 kHz. The excitation of the transmitter was performed by 400 V negative spike pulse and the gain of the receiving amplifier was 65 dB. In order to acquire signals for tomographic projections, the transmitter was manually attached to the edge of the sample using a specially developed holder. The acquisition of UGW signals was performed by a receiver placed 70 mm away from the investigated stainless steel sample at a fixed position. The measurement of UGW propagation was performed by rotating a stainless steel sample around the *z*-axis by 1° thus imitating receiver movement along the arc of the stainless steel sample. 181 signals were recorded at each transmitter position corresponding to the opposite 180° section of the investigated sample. Afterwards, the position of the transmitter was changed by 5° and the scanning of the opposite 180° section of the investigated

test sample was repeated. This procedure was repeated until all circumferential of the test sample was covered by the position of transmitter. This way, the signals for 73 projections needed for tomographic reconstruction were acquired.

As an example of the signals acquired for one projection, the B-scan image is presented in Fig. 5.1.4a. The signals were recorded at transmitter position of 0°. An example of waveforms of the acquired UGW signals for different receiver positions are presented in Fig. 5.1.4b. In order to determine the bandwidth in which UGW were excited, the frequency spectra for acquired projection was calculated (Fig.5.1.5a). It was estimated that UGW in the presented stainless steel sample were excited in the frequency bandwidths of 90–300 kHz and 520–720 kHz. Additionally, the gap in the presented frequency spectra at the 300–520 kHz bandwidth is observed, which corresponds to the strong dispersion zone of the symmetric S_0 UGW mode (Fig. 5.1.5b).

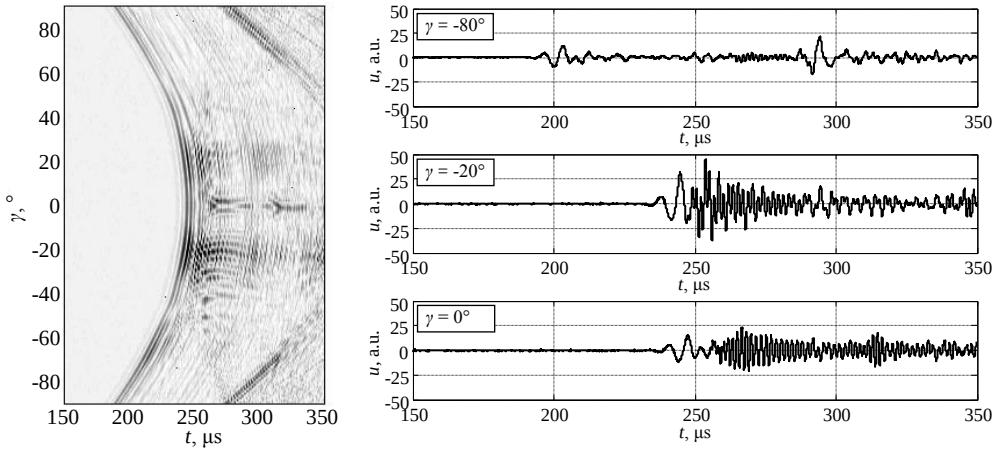

a) b)

Fig. 5.1.4. The B-scan image of UGW signals measured on the opposite side of the test sample when the transmitter is located at $\varphi_{Tr,1} = 0°$ (a) and the waveforms of the acquired signals for the different receiver positions γ (b)

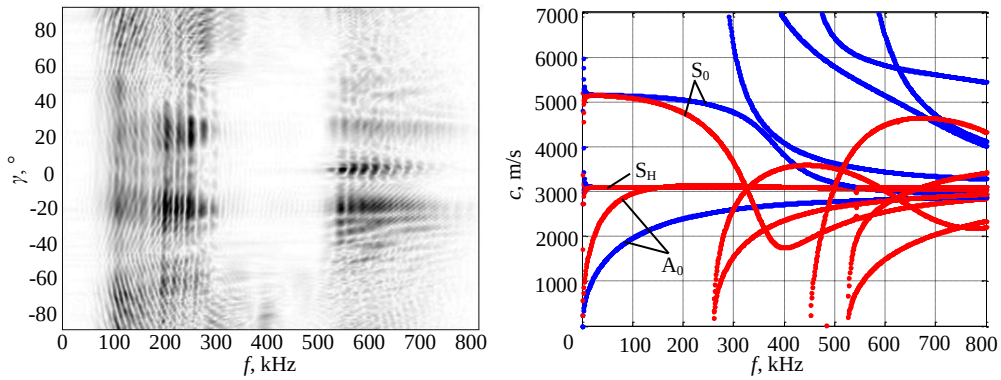

a) b)

Fig. 5.1.5. Frequency spectra of the acquired signals (a) and the UGW phase (blue) and group (red) velocity dispersion curves for a 6 mm thick stainless steel plate (b)

Based on the previous analysis of literature and the experimental study, it can be stated that only the front part of the acquired waveforms corresponds to the propagating and the symmetric S_0 UGW mode transmitted through the stainless steel sample with artificial defects, because it possesses a higher propagation velocity and should pass the test sample first; this part of the signal should be used for the calculation of tomographic projections. Since the measurements were carried out along the circumferential 180° section of the sample, the signal arrival time changes with respect to the position of the receiver because of different paths of wave propagation. Moreover, additional signal arrival time variation is conditioned by the thickness reduction at the positions of defects, since the velocity of UGW is dependent on the overall frequency-thickness product $f \cdot d$. Therefore, to correctly select the signal corresponding to the propagating symmetric S_0 UGW mode, time variable window was used. In order to set the boundaries of the time variable window, the signal arrival time was extracted from the time series to set the starting position of the time window boundaries. The algorithm proposed for time window calculation can be described as follows:

1. Frequency spectra of the acquired measurement signal is calculated by using the Fourier transform for each receiver position:

$$U_k^n(f) = \mathrm{FT}\left[u_k^n(t)\right], \tag{5.1.1}$$

where $n = 1 \div N_{\mathrm{Tr}}$, N_{Tr} – is the total number of transmitter positions; $k = 1 \div N_{\mathrm{Rc}}$, N_{Rc} – is the total number of the receiver positions at which signals were recorded.

2. The frequency spectrum is filtered with a special Gaussian filter with predefined parameters:

$$U_{k,\mathrm{F}}^n(f) = U_k^n(f) \cdot H(f - f_b), \tag{5.1.2}$$

where $H(f) = e^{-K(f-f_b)^2}$, $K = \dfrac{4\ln 0.5}{\Delta f^2}$, Δf is the bandwidth of the filter (Δf = 100 kHz), f_b is the centre frequency of the filter (f_b = 120 kHz). Filtering was used to eliminate the component of high frequency signal from the time series occurring before the component of lower frequency signal at some positions of transmitter and receiver, which could result in incorrect setting of front boundary of the time variable window.

3. The filtered signals were reconstructed using the inverse Fourier transform:

$$u_{k,\mathrm{F}}^n(t) = \mathrm{FT}^{-1}\left[U_{k,\mathrm{F}}^n(f)\right]. \tag{5.1.3}$$

4. The front boundary of the time variable window was determined by measuring time-of-flight using the zero-crossing technique [174, 175] of the filtered ultrasonic signals $u_{k,\mathrm{F}}^n(t)$. According to this method, the first point is detected where the received signal $u_{k,\mathrm{F}}^n(t)$ exceeds the threshold level U_{L}:

$$t_{\mathrm{L},k}^n = \min\left\{\arg\left[u_{k,\mathrm{F}}^n(t) > U_{\mathrm{L}}\right]\right\}, \tag{5.1.4}$$

$$t_{1\mathrm{w},k}^{n} = \max\left\{\arg\left[u_{k,\mathrm{F}}^{n}(t) = 0\right]\right\},\ t_{1\mathrm{w},k}^{n} < t_{\mathrm{L},k}^{n}\,, \tag{5.1.5}$$

where $t_{\mathrm{L},k}^{n}$ is the time instance at which signal $u_{k,\mathrm{F}}^{n}(t)$ exceeds the threshold level U_L, $t_{1\mathrm{w},k}^{n}$ is the estimated zero-crossing time moment of the signal $u_{k,\mathrm{F}}^{n}(t)$.

5. The second boundary of the variable time window was set by adding a fixed value Δt_w of the window width to the t_{1w}:

$$t_{2\mathrm{w},k}^{n} = t_{1\mathrm{w},k}^{n} + \Delta t_{\mathrm{w}}\,. \tag{5.1.6}$$

During the analysis of the experimentally measured signals, the width of the time window Δt_w was set to 55 μs, which corresponds to the time interval it takes for the symmetric S_0 UGW mode to pass twice the distance in water between the receiver and the stainless steel plate. Such width of the time window was set in order to eliminate the occurring multiple reflections in the gap between the test sample and the receiver. The example of the experimentally acquired B-scan image with denoted time variable window boundaries is presented in Fig. 5.1.6a and the frequency spectra of the acquired UGW signals within the boundaries of time variable window are presented in Fig. 5.1.6b. The frequency spectra show that during the experimental research, the UGW in the investigated 6 mm thick stainless steel sample were basically generated at two frequency ranges – 100–275 kHz and 550–750 kHz. A generic characteristic of the frequency spectra was similar to all measured projections. The figure indicates that the higher frequency signal components were acquired at the narrower 100–120° opposite section of the sample. It follows that by performing tomographic reconstruction at higher frequencies, reliable reconstruction results are only possible at the reduced size sub-volume limited by two outermost rays as the fan formed by single transmitting transducer. On the basis of the results, it was decided to perform tomographic reconstruction in the frequency range of 100–275 kHz.

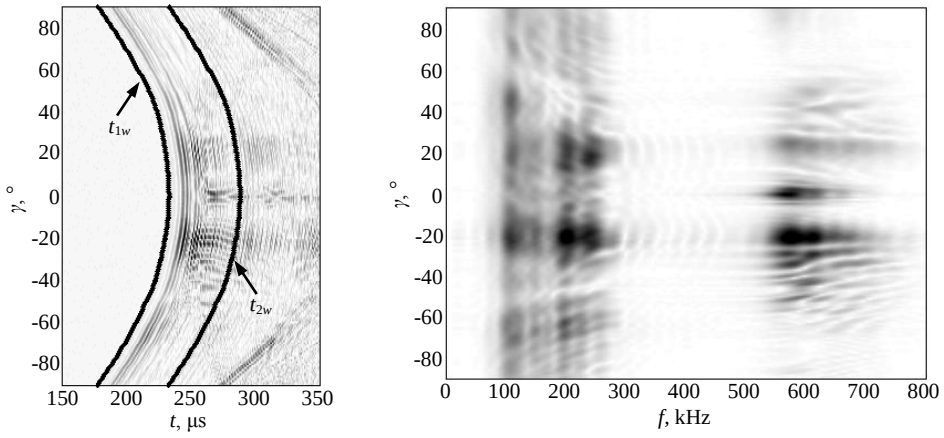

Fig. 5.1.6. The B-scan image of the experimentally acquired UGW signals with denoted boundaries of time variable window (a) and the frequency spectra of the acquired signals within the boundaries of time variable window (b)

Since the spatial resolution and sensitivity of the ultrasonic measurements depend on the wavelength of incident wave frequency, a filtering method was applied to the experimental data taken within the boundaries of time variable window to distinguish the signal components with the highest amplitude. The filtering was performed according to the equations 5.1.1–5.1.3. The centre frequency f_b of the applied Gaussian filter was set to 110 kHz, 200 kHz and 240 kHz, respectively. The bandwidth Δf of the filter was 50 kHz in all cases. The example of the calculated projections at different centre frequency of Gaussian filter f_b and different transmitter positions are presented in Fig. 5.1.7.

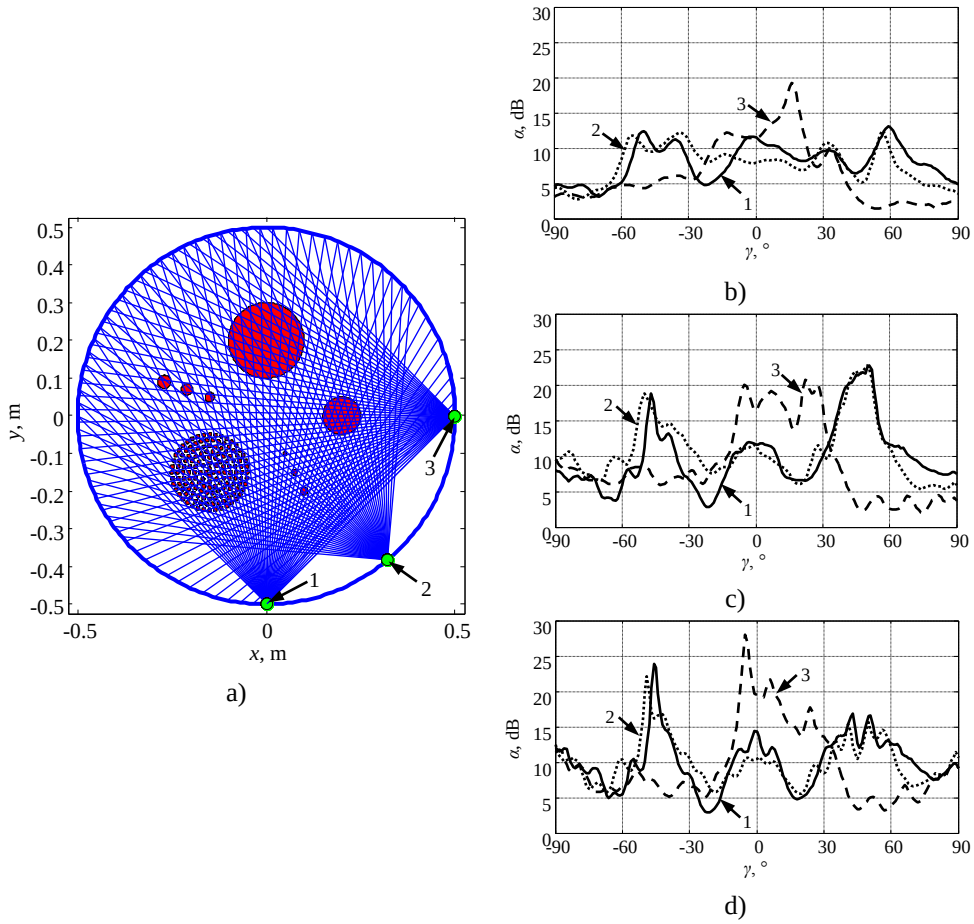

Fig. 5.1.7. The distribution of the transmitters and receivers when the transmitter is located at $\varphi_{Tr,1}$ – 0°, $\varphi_{Tr,2}$ – 45°, $\varphi_{Tr,3}$ – 90° (a), the variation of the measured projections when the centre frequency of the applied Gaussian filter is 110 kHz (b), 200 kHz (c), 240 kHz (d) and the transmitter is located at 1 – 0°, 2 – 45°, 3 – 90°

The reconstruction of the special distribution of UGW attenuation in the investigated stainless steel sample with artificial part-thickness depth defects was carried out by applying the tomographic reconstruction method presented in the previous chapter. To reduce the high frequency noise in the filtered projection which

directly influences the quality of the reconstructed image, the projections were filtered using a corrected tomographic filter H_{Tc}. During the processing of experimental data, the cut-off frequency of the smoothing (low-pass) filter f_{fs0} was set to $1/15 f_{x,max}$. The frequency response of such corrected tomographic filter can be found in Fig. 4.4.1 (corresponds to the function defined as H_{Tc1}). The reconstructed distribution of the symmetric S_0 UGW mode attenuation at different (110 kHz, 200 kHz and 240 kHz) central frequency of the applied Gaussian filter are presented in Fig. 5.1.8–Fig. 5.1.10, respectively.

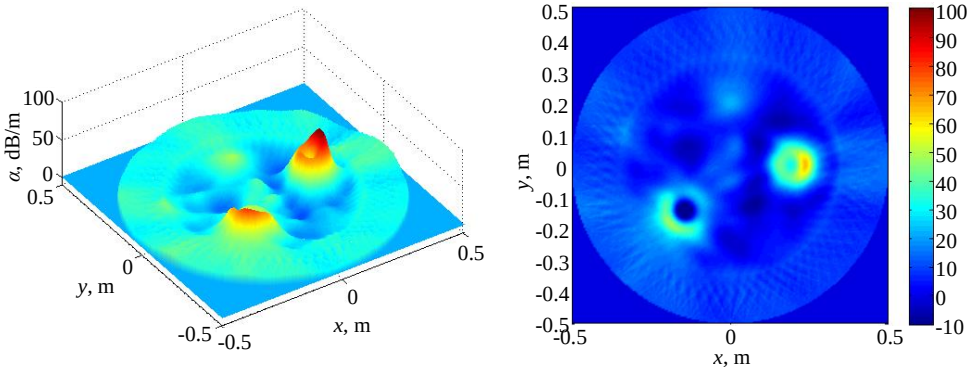

a) b)

Fig. 5.1.8. The reconstructed distribution of the S_0 UGW mode attenuation in the investigated stainless steel sample with artificial defects when f_b = 110 kHz in the form of a 3D image (a) and a C-scan image (b)

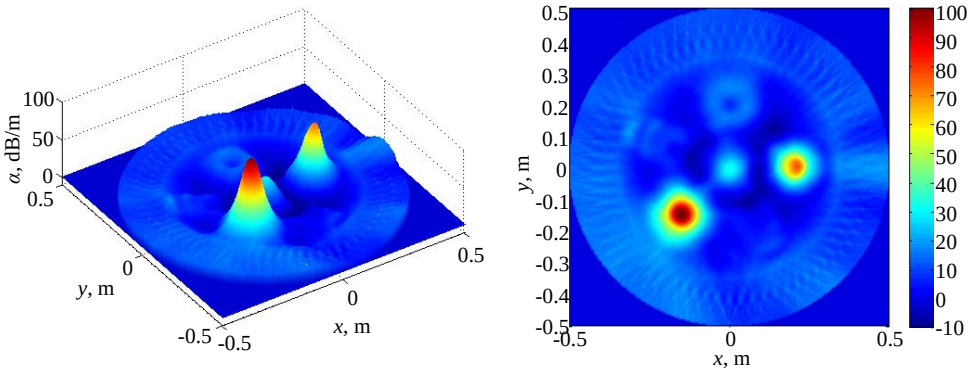

a) b)

Fig. 5.1.9. The reconstructed distribution of the S_0 UGW mode attenuation in the investigated stainless steel sample with artificial defects when f_b = 200 kHz in the form of a 3D image (a) and a C-scan image (b)

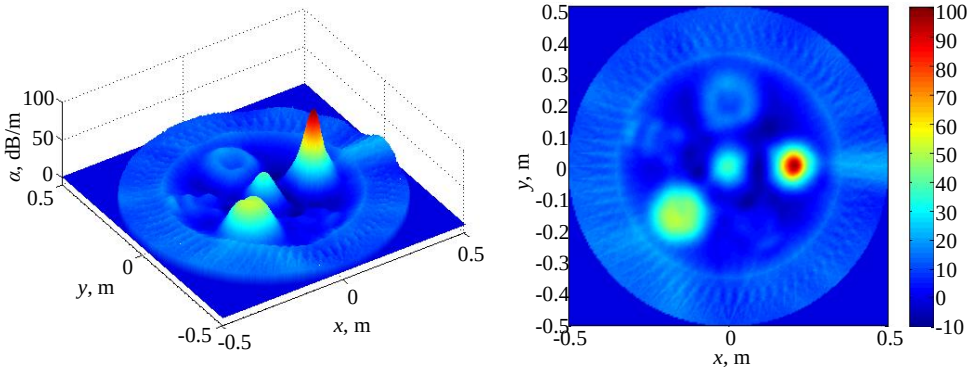

Fig. 5.1.10. The reconstructed distribution of the S_0 UGW mode attenuation in the investigated stainless steel sample with artificial defects when f_b = 240 kHz in the form of a 3D image (a) and a C-scan image (b)

In general, the experimental investigation demonstrates that different UGW frequencies show different sensitivity to the artificially made defects because of the dependency of direct spatial resolution on the wavelength. Furthermore, Fig. 5.1.8–Fig. 5.1.10 present the increase of the attenuation in the middle of the stainless steel sample. This increase is conditioned by the mounting base of Ø115 mm diameter on which the sample is placed. The presented images imply that only weak traces of diffracted waves around the small-diameter (Ø10 ÷ Ø35 mm diameter) single circular defects could be observed in the reconstructed S_0 UGW mode attenuation map. Meanwhile, the reconstructed attenuation distribution of the larger Ø100 mm, Ø200 mm and overall Ø200 mm diameter pit cluster defects possess the overall attenuation character close to those presented in Fig. 4.5.6–Fig. 4.5.8. In this instance, the mean value of attenuation enclosed by Ø100 mm defect is 42.7 dB/m, by Ø200 mm defect – 9.2 dB/m, by Ø200 mm pit cluster defect – 18.4 dB/m at 110 kHz frequency. Meanwhile, at 200 kHz frequency, the mean attenuation values were: by Ø100 mm defect – 41.7 dB/m, by Ø200 mm defect – 9.2 dB/m, by Ø200 mm pit cluster defect – 29.9 dB/m. And at 240 kHz frequency the values were: by Ø100 mm defect – 47.8 dB/m, by Ø200 mm defect – 9.2 dB/m, by Ø200 mm pit cluster defect – 23.2 dB/m. The dB drop method was applied in order to perform 2D sizing of the Ø100 mm, Ø200 mm and overall Ø200 mm diameter pit cluster defects. The defects were sized at -3 dB and -6 dB drop levels from the maximum indication value of attenuation from the defect. A graphical representation of the estimated defect sizes at different dB drop levels are presented in Fig. 5.1.11. The results of defect sizing at -3 dB and -6 dB attenuation drop levels are presented in Table 5.1.1 and Table 5.1.2, respectively.

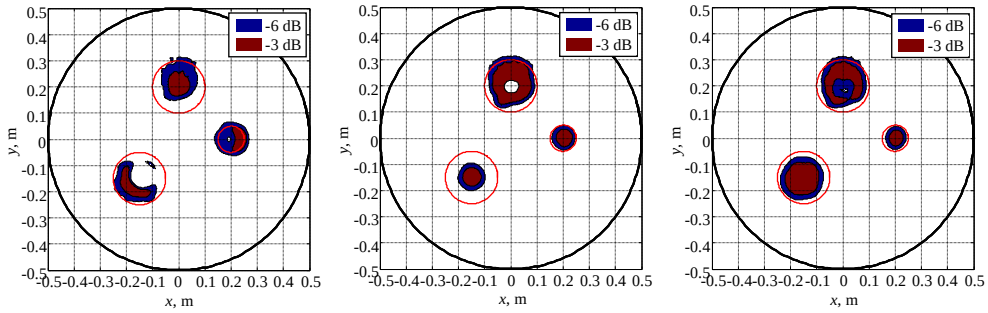

a) b) c)

Fig. 5.1.9. Sizing of defects by dB drop method when the centre frequency of the applied Gaussian filter: f_b = 110 kHz (a), f_b = 200 kHz (b), f_b = 240 kHz (c)

Table 5.1.1. Defect sizing at -3 dB attenuation drop level

Defect diameter d_{cd}, mm	Defect area A_{cd}, cm^2	Reconstructed defect area A_{cdr}, cm^2		
		at 110 kHz	at 200 kHz	at 240 kHz
200	314.16	61.78	193.12	132.05
100	78.54	38.26	32.08	25.25
200 (pit cluster)	314.16	53.87	39.53	132.23

Table 5.1.2. Defect sizing at -6 dB attenuation drop level

Defect diameter d_{cd}, mm	Defect area A_{cd}, cm^2	Reconstructed defect area A_{cdr}, cm^2		
		at 110 kHz	at 200 kHz	at 240 kHz
200	314.16	180.15	292.12	269.91
100	78.54	131.62	64.86	53.65
200 (pit cluster)	314.16	131.83	84.2	214.97

In this instance, the 2D sizing of defects shows that the overall sizing of the defects is conditioned by the wavelength of the UGW. Despite the fact that low frequency UGW can propagate longer distances in the investigated object, the use of the higher frequency UGW allows more accurate sizing of the defect. Additionally, the use of higher frequency allows to perform a reconstruction with higher spatial resolution.

5.2 An experimental investigation of the scaled-down storage tank mock-up using a limited number of projections

The purpose of this research is the experimental investigation of the symmetric S_0 UGW mode propagation in the 1:8 scaled-down storage tank mock-up and the reconstruction of the spatial view of tank floor by applying the proposed tomographic reconstruction algorithm. The experimental set-up scheme used for the investigation of UGW propagation and the view of the scaled-down storage tank mock-up are presented in Fig. 5.2.1 and Fig. 5.2.2, respectively.

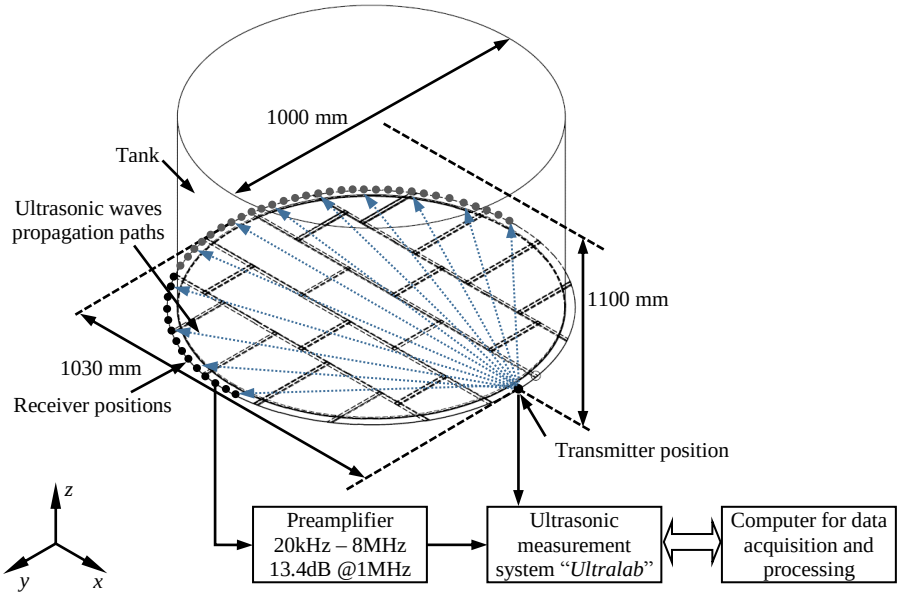

Fig. 5.2.1. The experimental set-up scheme for the investigation of UGW propagation in a scaled-down storage tank mock-up

a) b)

Fig. 5.2.2. The mock-up of the scaled-down storage tank (a) and the construction of the storage tank floor (b)

The experimental investigation of the symmetric S_0 UGW mode propagation in a scaled-down storage tank mock-up was performed by using a low-frequency ultrasonic measurement system "Ultralab", produced and manufactured in Prof. K. Baršauskas' Ultrasound Research Institute of Kaunas University of Technology. The excitation of UGW in the presented scaled-down storage tank was performed by using a low-frequency ultrasonic transducer operating in the thickness mode and attached directly to the edge of tank floor by using a spring-type adjuster. Glycerol was used as coupling material for better acoustical contact between the transducers and the scaled-down tank. In order to have a smoother surface, the edge of tank floor was prepared in advance by grinding. The excitation of UGW in the

presented scaled-down tank mock-up was performed by using 400 kHz frequency 3 periods rectangular pulse with the amplitude of 500 V. 158 receiver positions were used at each transmitter position, corresponding approximately to the opposite 180° sector of the storage tank floor. During the experimental measurements, 11 signals were recorded at each receiver position in order to increase the reliability of the measurements because the transducer used for the reception of UGW was manually pressed to the edge of the storage tank floor and it was complicated to continuously have a good and stable acoustical contact. The signals were digitised with a sampling frequency of 100 MHz. The frequency range of the amplifier filter was 0.02–2 MHz. The positions of the transmitters during the experimental measurements along the circumferential edge of the tank floor and the coverage of the scaled-down tank floor are shown in Fig. 5.2.3. During the experimental investigation, a total of 7 tomographic projections were acquired.

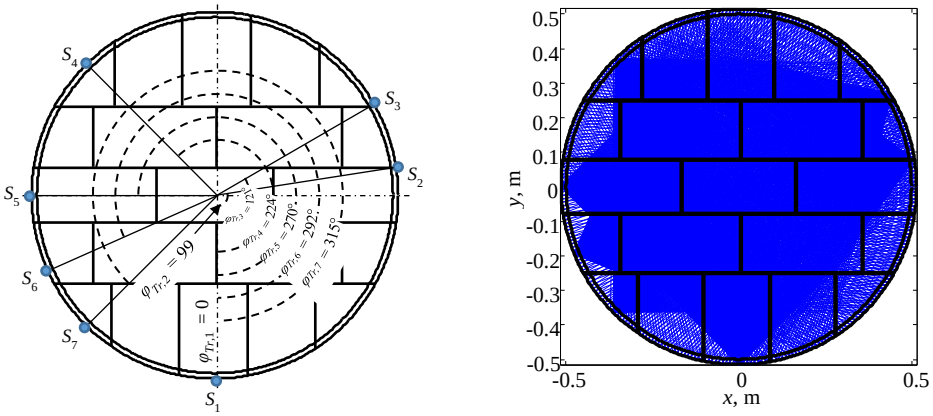

a) b)

Fig. 5.2.3. The floor of the scaled-down storage tank with denoted positions (blue dots) of the transmitters (a), all measurement directions and coverage of the tank floor (b)

The projection in the UGW transmission tomography is assumed to be the distribution of attenuation versus the transmission direction or angle for one transmitter position. At each position, the relative attenuation was measured from the acquired signals. The other projections were acquired in a similar way, only the transmitter was attached to the edge of the storage tank floor at different positions with a step from the previous one and the measurements on the opposite side of the tank in a corresponding 180° sector of the storage tank floor are performed. In general, the tomographic reconstruction requires as many different projections as possible, because the accuracy and resolution of the reconstructed images depend on the number of observed projections and rays per projection. On the other hand, the accuracy depends on the wavelength of the propagating symmetric S_0 wave mode and the optimal number of projections should be determined for each case.

In our research, it was stated that only the front part of the acquired waveforms corresponds to the propagating and transmitted through the storage tank floor symmetric S_0 UGW mode, because it has a higher propagation velocity and should pass the tank floor first, and this part of the signal should be used for the calculation

of tomographic projections. To distinguish the signal part corresponding to the propagating symmetric S_0 wave mode a time variable window, which was presented in section 2.5 and defined with equations 2.5.3 and 2.5.4 was used. The maximum amplitude of the symmetric S_0 UGW mode signal within the ranges of the time window was calculated according to equation 2.5.5, as well. An example of the experimentally obtained B-scan image with denoted time window boundaries t_{w1} and t_{w2} necessary to select the symmetric S_0 UGW mode and the amplitude distribution of the S_0 wave mode within the boundaries of time variable window for a single experimentally obtained projection are presented in Fig. 5.2.4 and Fig. 5.2.5, respectively. By comparing the experimental results with the 3D modelling (presented in Section 2.5) of UGW propagation in the scaled-down storage tank, it could be seen that the S_0 UGW mode transmitted through the scaled-down storage tank floor shows a similar manner of amplitude distribution along the circumferential edge of the tank. At the same time, it proves that the amplitude of the waves transmitted through the storage tank floor are strongly dependent on the number of welds, and the strongest signals are expected at the positions with fewer weld seams in direct wave propagation path.

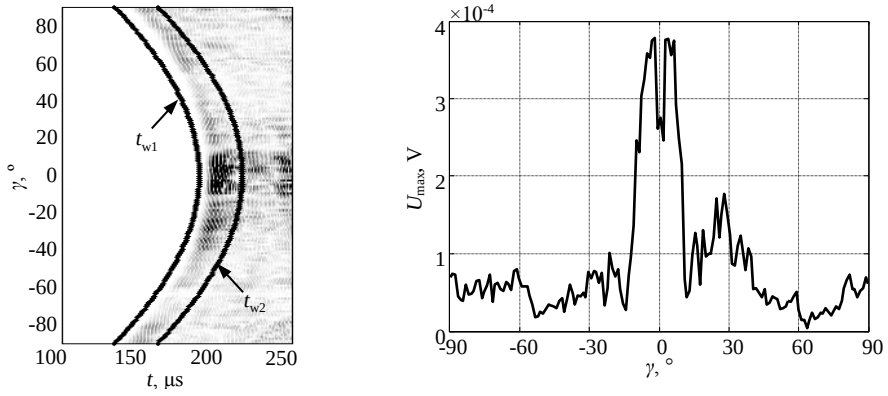

a) b)

Fig. 5.2.4. The experimental B-scan image of UGW signals measured at one position of the transmitter and receivers for a single projection (a), amplitude change of the symmetric S_0 UGW mode within the boundaries of time variable window (b)

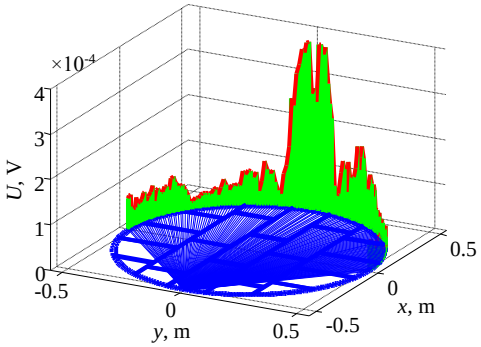

Fig. 5.2.5. The amplitude distribution of the symmetric S_0 UGW mode along the circumferential edge of the tank floor for a single projection

Before reconstruction, each of the experimentally measured projections were filtered according to the requirement of tomographic reconstruction. At the last step, back-projection of each projection was performed in the virtual storage tank floor plane and the back-projections obtained from the data acquired at different transmitter positions were integrated. As it was described in the previous section, the data acquisition was performed along the circumferential edge of the tank floor by using 158 receiver positions and a total of 7 tomographic projections were acquired. From this point, the measurement data do not create a very fine net of storage tank floor coverage. To compensate for this shortcoming and to simplify the implementation of the back-projection procedure, a parameter called virtual beam width d_{beam} was introduced. The introduced beam width in the back-projection means that the back-projection was performed not only along the line between the transmitter and receiver, but in the area limited by lines parallel to the line transmitter/receiver and situated by $\pm d_{\text{beam}}/2$ from it. A graphical interpretation of the virtual beam width is presented in Fig. 5.2.6.

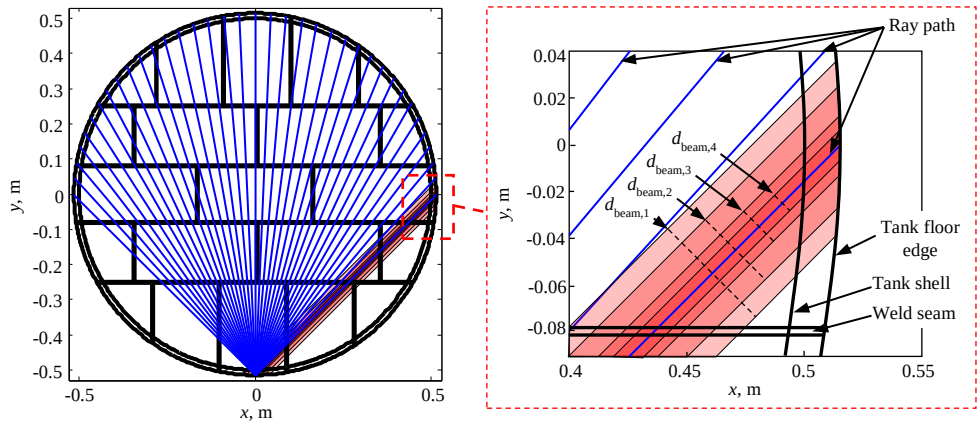

Fig. 5.2.6. A graphical interpretation of the virtual beam width d_{beam}

The weighting coefficient K_{d} depending on the distance from this line was introduced also. This coefficient can be expressed as:

$$K_{\text{d}} = \begin{cases} \dfrac{d_{\text{beam}}}{2} - d_{\text{p}} & \text{if } \dfrac{d_{\text{beam}}}{2} > d_{\text{p}} \\ 0 & \text{otherwise} \end{cases}, \tag{5.2.1}$$

where d_{p} is the distance between a point on the virtual reconstruction plane and the line transmitter/receiver under analysis. The image obtained with a relatively wide beam is presented in Fig. 5.2.7a. The large areas of higher attenuation can be observed in the reconstructed image (Fig. 5.2.7a). However, in this image overly complicated to find a relation between increase of attenuation with the weld position. The reconstructed images of the storage tank floor presented in Fig. 5.2.7b–Fig. 5.2.7d with a narrow beam width show that separate measurement lines could be seen, but analysis is very complicated. However, some correlation with the welds in the storage tank floor could be observed. The mismatch in the position can be explained by the

errors in the measurement of the transducer positions around the circumferential edge of tank floor.

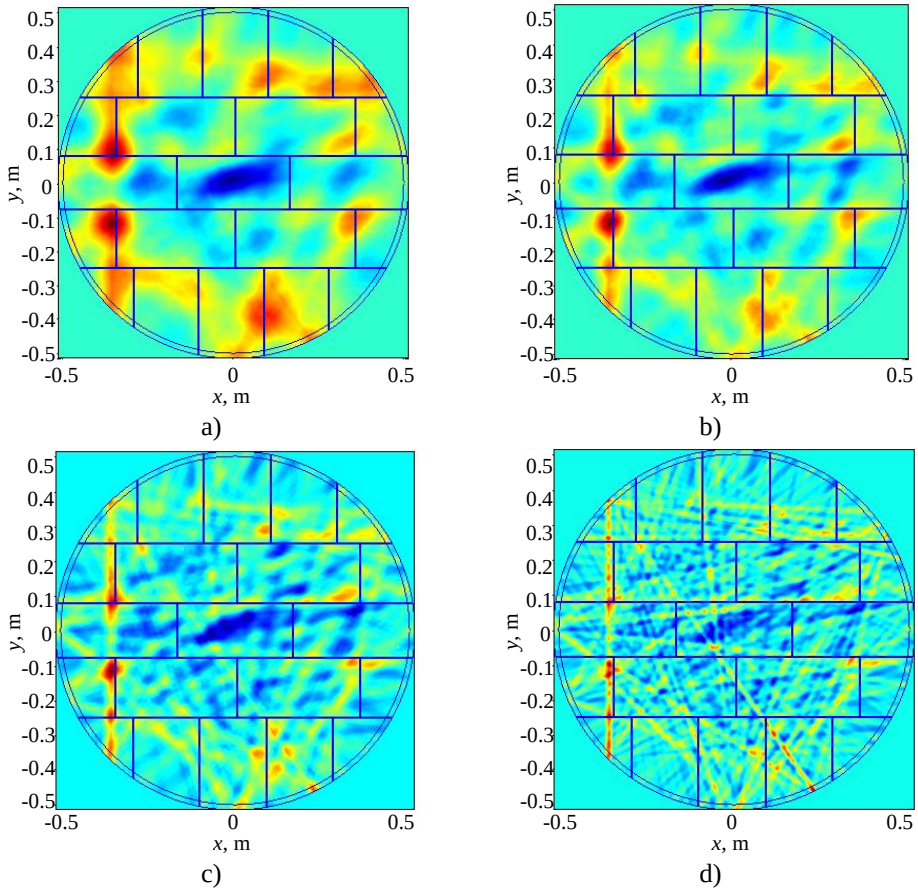

Fig. 5.1.7. The reconstructed relative distribution of the attenuation of the S_0 UGW mode propagating in the tank floor from the experimental data when: $d_{beam,1}$ = 0.075 m (a), $d_{beam,2}$ = 0.05 m (b), $d_{beam,3}$ = 0.025 m (c), $d_{beam,4}$ = 0.0125 m (d). The red areas correspond to the areas with an essentially higher attenuation. The blue lines represent the positions of welds.

The experimental investigation of UGW propagation through a scaled-down storage tank mock-up demonstrates that the proposed tomographic reconstruction technique enables to reconstruct the spatial distribution of the attenuation of symmetric S_0 guided wave mode. However, the relatively small number of experimentally acquired projections needed for tomographic reconstruction and a relatively big step between the adjacent receiver positions lead to insufficient resolution and inaccuracy to recognize the exact positions of all welds and enable to reconstruct only large areas with higher attenuation. Nevertheless, the correlation of higher attenuation areas with the expected positions of welds can be observed.

5.3 Metrological evaluation of the measurement method

In general, the measurement uncertainty is determined in accordance with the selected measurement process model. The measurement results of defects and their parameters, such as attenuation, measurement in the storage tanks are influenced by various sources of uncertainties where most of the following arise from [176, 177]:

- an incomplete definition of the measurand; the instability of the measured parameter in changing environmental conditions during the measuring process;
- inadequate knowledge of the effects of errors in the environmental conditions on the measurement process;
- approximations and assumptions incorporated in the measurement method and procedure;
- operator's influence due a lack of knowledge, preparation and inadequate selection of measurement conditions, etc.

In general, the mathematical model for uncertainty estimation is a function of several input quantities showing how the measurement result is obtained from the input quantities. If the input quantities are designated as x_1, x_2, …, x_n, then the functional relationship between the measurement result y and the input quantities x_i ($i = 1 \div n$) could be defined according to equation 5.3.1:

$$y = f\left(x_1, x_2, \ldots, x_n\right). \tag{5.3.1}$$

The function f determines the measurement procedure and refers how the output values y are obtained from the complex of input values x_1, x_2, …, x_n. Depending on the method used to estimate the numerical values of uncertainties, the input values of the uncertainty are grouped into two categories – type A and type B. A type A uncertainty is an estimate derived from statistical analysis of the experimental data, whose values are obtained after repeated measurements. A type B uncertainty estimate is an estimate obtained from external sources that are known or determined on the basis of long-term experimental experience, taken from a handbook, extracted from a calibration report, etc.

For this instance, the experimental investigation of attenuation distribution reconstruction in the specially developed stainless steel sample with artificial defects and in the scaled-down storage tank mock-up refers to the A type uncertainty source, for which statistical analysis is performed. Typically, in tomographic reconstruction such analysis is based on calibrated work-pieces by a series of repetitive measurements under the same or similar conditions. However, in practice, such procedure is time-consuming, since the presented experimental acquisition of projections needed for tomographic reconstruction was performed manually changing the position of the transmitter. For this instance, the numerical modelling results on the tomographic reconstruction based on the tank floor model developed in the case of different angular object sampling (the number of receiver and transmitter positions) and used filter function were presented in Section 4.4.

In measurement systems based on the use of UGW, the main type B standard uncertainty sources which have an impact on the measurement results are:

- variations of alignment between transducers and the plate (acoustical contact variation);
- amplitude variation due to transducer directivity;
- spatial variations of acoustical properties of the object (longitudinal velocity c_L, shear velocity c_S, density ρ);
- the UGW frequency variations resulted from wave dispersive properties;
- object thickness *dz* changes, which directly influence the dispersive properties of ultrasonic waves;
- diffraction, reverberation and attenuation of UGW;
- influence of the conditions in the surrounding air: temperature *T*, humidity *H* and pressure *P*;
- object temperature *T* influence;
- signal quantification *Q* and discretisation steps ΔT;
- electrical noises N_{el}, influenced by the amplification cascades and lead connections.

The next assumption for the estimation of measurement uncertainty was that there are no correlations between different uncertainty sources and the sensitivity coefficient $W_i = 1$ is valid for all cases. The sensitivity coefficient W_i shows what influence each uncertainty source has on a standard combined uncertainty and the assumption $W_i = 1$ gives the worst case of uncertainty. In this regard, the estimated uncertainty is the largest.

Since UGW are propagating long distances in a noisy environment, some of the uncertainty sources in the measurements could be neglected because they have a negligible effect on the measurement results. Those components are:

- Quantification step *Q*, in the case of 10-bit ADC converter and 1 V reference voltage is Q = 976 μV, so the quantization error was equal to half of the quantum ($Q/2$ = ±488 μV). However, if the measurement signal is averaged (in experiment 8 times), the number of quantum could be obtained by using equation 5.3.2 [178]:

$$Q = b_{\mathrm{ADC}} - b_{\mathrm{N}} + \frac{1}{2}\log_2(N), \tag{5.3.2}$$

where b_{ADC} – ADC converter bit number, b_{N} – noise level in bits (1 bit at least), N – number of the quantization levels. This ensures that in a 10-bit ADC converter and signal averaging, the number of quantum becomes equivalent to a 14-bit converter. In this case, the quantization step becomes Q = 61 μV and by considering rectangular distribution law, the lowest error value is equal to $Q/2\sqrt{3}$, or approximately 17.6 μV. In the case of signal discretisation, at the sampling frequency of 100 MHz, the discretisation of the signals is performed in the time periods of 10 ns. By taking into account the rectangular distribution law, the lowest error value is equal to $T/2\sqrt{3}$, or approximately 2.9 ns.

- The influence of the electrical noise in the amplifier and the overall circuit N_{el} is random and, in most cases, can be reduced by averaging the ultrasonic signals. In our case, the averaging of the 16 signals at each position of the receiving transducer was used. This reduces random noise roughly by 4 times.
- The experimental measurements of UGW propagation were performed at room temperature (20ºC ± 2ºC). Using the immersion measurement method at sufficiently short interval of time, the uncertainty of temperature change is quite small and may be neglected. The influence of humidity and pressure was not studied, because the experiments were carried out in a controlled laboratory environment and the influence of those parameters on the measurement results may be neglected as well.

The mechanical parameters of the plate give the effects on the variations of the guided waves velocities. Additionally, standard uncertainties caused by the changes in the object mechanical parameters (such as density, Young modulus, Poisson's ratio) can be calculated by making certain assumptions. For this purpose, the S_0 wave mode velocity was calculated by changing the particular parameters of the plate.

5.4 Conclusions of the Chapter 5

1) The experimental investigation on the scaled-down storage tank mock-up demonstrated that the projections estimated from the acquired signals coincide with the losses presented in the previous section of the work. It was observed that the overall losses of the signals transmitted through tank floor are strongly influenced by the number of welds in the wave propagation path, thus allowing signals with the higher amplitude to be observed in sections with less number of welds.
2) The reconstruction of the attenuation distribution in the storage tank mock-up using the developed method reveal some areas with higher attenuation, even in the case of limited number of projections, which coincide with the cross-section of the welds in the tank floor.
3) It was also shown that in large areas with reduced wall thickness the losses are mainly caused on the boundaries of the zones and this can be observed in the reconstructed images and the losses can be estimated from the reconstructed data.

GENERAL CONCLUSIONS

1. The analysis of literature has shown that all previous methods for detecting defects and measuring their parameters inside a storage tank allows to detect the defects only locally and are time-consuming procedures, since they require the tank to be emptied and cleaned before inspection could be performed. The only technique which enables to inspect or at least assess the corrosion level of a tank is the technique based on the application of UGW together with ultrasonic transmission tomography. The analysis has shown that this technique has a potential to obtain the 2D map of general corrosion.
2. The technique based on UGW transmission tomography was developed, enabling to measure the attenuation of guided waves in the storage tank floor and their spatial distribution. The reconstruction of the true values of attenuation was achieved by introducing an additional stage into the reconstruction algorithm based on optimization.
3. The proposed ultrasonic transmission tomography algorithm was verified using the developed tank floor model, which enables to consider the average attenuation in plate, attenuation in the corroded areas and losses on the weld. The results obtained using the developed model demonstrate that the 2% mean relative error of true value of attenuation spatial distribution reconstruction is achievable in plates with no weld. Meanwhile, in the tank floor with welds, the mean relative error increases to 7% in the reconstruction of true value of attenuation. Such increase of relative reconstruction error could be explained by the sharp attenuation profile change at the intersection of corroded areas and welds.
4. The investigation using a 3D model of the scaled-down storage tank has demonstrated that there is no essential increase of losses in the case of UGW propagating under an angle with respect to the weld. However, the angle of the opposite side of the tank at which the guided waves can be received is limited approximately to 180° due to the arrival of stronger waves directly through the tank wall. The simulation results prove that the main propagation losses occur on the welds of tank floor and because of the wave diffraction. In this regard, by considering the real size of the storage tank, the probable propagation distance of UGW is limited to 20–30 m.
5. The finite elements modelling has demonstrated that the transmission losses of the symmetric S_0 wave mode on lap weld vary in the ranges from 1 dB to 8 dB per weld depending on the ratio between the width of the lap joint Δl and wavelength λ. It is very important for practical application that additional bonding caused by corrosion can essentially reduce transmission losses. This explains the difference between the assessed attenuation by modelling and measurements on a real tank carried out during the earlier investigations.
6. The developed ultrasonic transmission tomography technique for measuring the attenuation was verified experimentally. Two types of experimental investigation have been carried out and have shown that:

a) the experiments on a specially developed stainless steel circular sample with different artificial defects have demonstrated that in large areas with reduced wall thickness the losses mainly are caused on the boundaries of the zones and this can be observed and estimated in the reconstructed images. The resolution and sensitivity investigation has demonstrated that the defects comparable to the wavelength of incident wave could be observed and their values reconstructed by the proposed method.
b) the experiments carried out on the scaled-down storage tank mock-up floor have proven the modelling results and demonstrated similar regularities of wave propagation under the angle with respect to the weld and 180° angular limit for acquisition of tomographic projections. Herewith, the limited number of acquired projections enabled to reconstruct only large areas with higher attenuation which coincide with the cross-section of the welds in the tank floor.

REFERENCES

1. BRITTON, C.F. Shreir's Corrosion B. COTTIS, et al ed., Oxford: Elsevier, 2010 *4.36 - Corrosion Monitoring and Inspection*, pp. 3117-3166. ISBN 9780444527875.
2. TSUKADA, K., YOSHIOKA, M., KAWASAKI, Y. and KIWA, T. Detection of Back-Side Pit on a Ferrous Plate by Magnetic Flux Leakage Method with Analyzing Magnetic Field Vector. *NDT & E International*, 6, 2010, vol. 43, no. 4. pp. 323-328. ISSN 0963-8695.
3. KASAI, N., SEKINE, K. and MARUYAMA, H. Non-Destructive Evaluation Method for Far-Side Corrosion Type Flaws in Oil Storage Tank Bottom Floors using the Magnetic Flux Leakage Technique. *Journal of the Japan Petroleum Institute*, 2008, vol. 46, no. 2. pp. 126-132 ISSN 13468804.
4. KASAI, N., SEKINE, K. and MARUYAMA, H. Influence of Corrosion Products on Magnetic Flux Leakage Signals in Inspection of Far-Side Metal-Loss Defects in Oil Storage Tank Bottom Floors. *Journal of the Japan Petroleum Institute*, 2004, vol. 47, no. 1. pp. 19-26 ISSN 13468804.
5. KASAI, N., FUJIWARA, Y., SEKINE, K. and SAKAMOTO, T. Evaluation of Back-Side Flaws of the Bottom Plates of an Oil-Storage Tank by the RFECT. *NDT & E International*, 10, 2008, vol. 41, no. 7. pp. 525-529. ISSN 0963-8695.
6. KASAI, N., MATSUZAKI, S. and SAKAMOTO, T. Experimental and Analytical Study for Detectability of the Back-Side Flaws of Flat Ferromagnetic Plates by RFECT. *NDT & E International*, 12, 2011, vol. 44, no. 8. pp. 703-707. ISSN 0963-8695.
7. BAGAVATHIAPPAN, S., et al. Infrared Thermography for Condition Monitoring – A Review. *Infrared Physics & Technology*, 9, 2013, vol. 60, no. 0. pp. 35-55. ISSN 1350-4495.
8. MARINETTI, S. and VAVILOV, V. IR Thermographic Detection and Characterization of Hidden Corrosion in Metals: General Analysis. *Corrosion Science*, 3, 2010, vol. 52, no. 3. pp. 865-872. ISSN 0010-938X.
9. EDALATI, K., et al. The use of Radiography for Thickness Measurement and Corrosion Monitoring in Pipes. *International Journal of Pressure Vessels and Piping*, 10, 2006, vol. 83, no. 10. pp. 736-741. ISSN 0308-0161.
10. KOMAROV, K.L., et al. Acoustic Emission Method for Testing Oil and Gas Tanks. *Russian Journal of Nondestructive Testing*, 2001, vol. 37, no. 3. pp. 232-237 ISSN 1061-8309.
11. KWON, J., LYU, G., LEE, T. and KIM, J. Acoustic Emission Testing of Repaired Storage Tank. *International Journal of Pressure Vessels and Piping*, 5, 2001, vol. 78, no. 5. pp. 373-378. ISSN 0308-0161.
12. NOWAK, M., BARAN, I., SCHMIDT, J. and ONO, K. Acoustic Emission Method for Solving Problems in Double Bottom Storage Tanks. *Journal of Acoustic Emission*, 2009, vol. 27. pp. 272-280 ISSN 0730-0050.
13. ROSE, J.L. Ultrasonic Guided Waves in Structural Health Monitoring. *Key Engineering Materials*, 2004, vol. 270-273. pp. 14-21.
14. ZHAO, X., ROYER, R.L., OWENS, S.E. and ROSE, J.L. Ultrasonic Lamb Wave Tomography in Structural Health Monitoring. *Smart Materials and Structures*, 2011, vol. 20, no. 10. pp. 105002 ISSN 0964-1726.

15. LACKNER, G. and TSCHELIESNIG, P. Field Testing of Flat Bottomed Storage Tanks with Acoustic Emission - A Review on the Gained Experience. *Journal of Acoustic Emission*, 2004, vol. 22. pp. 201-207 ISSN 0730-0050.
16. LONG, F. and XU, H. *Validity Identification and Classification Technique of Tank Acoustic Emission Testing Signals Based on Clustering Analysis.* , 2011 DOI 10.1109/FSKD.2011.6019805.
17. LOWE, M.J.S., ALLEYNE, D.N. and CAWLEY, P. Defect Detection in Pipes using Guided Waves. *Ultrasonics*, 2, 1998, vol. 36, no. 1–5. pp. 147-154. ISSN 0041-624X.
18. ALLEYNE, D.N., PAVLAKOVIC, B., LOWE, M.J.S. and CAWLEY, P. Rapid, Long Range Inspection of Chemical Plant Pipework using Guided Waves. *AIP Conference Proceedings*, 2001, vol. 557, no. 1. pp. 180-187.
19. DEMMA, A., et al. The Reflection of Guided Waves from Notches in Pipes: A Guide for Interpreting Corrosion Measurements. *NDT & E International*, 4, 2004, vol. 37, no. 3. pp. 167-180. ISSN 0963-8695.
20. LEINOV, E., LOWE, M.J.S. and CAWLEY, P. Investigation of Guided Wave Propagation and Attenuation in Pipe Buried in Sand. *Journal of Sound and Vibration*, 7/7, 2015, vol. 347, no. 0. pp. 96-114. ISSN 0022-460X.
21. ROSE, J.L., AVIOLI, M.J., MUDGE, P. and SANDERSON, R. Guided Wave Inspection Potential of Defects in Rail. *NDT & E International*, 3, 2004, vol. 37, no. 2. pp. 153-161. ISSN 0963-8695.
22. MOUSTAKIDIS, S., et al. An Intelligent Methodology for Railways Monitoring using Ultrasonic Guided Waves. *Journal of Nondestructive Evaluation*, 12/01, 2014, vol. 33, no. 4. pp. 694-710 ISSN 0195-9298.
23. RAIŠUTIS, R., et al. Ultrasonic Guided Wave-Based Testing Technique for Inspection of Multi-Wire Rope Structures. *NDT & E International*, 3, 2014, vol. 62. pp. 40-49. ISSN 0963-8695.
24. LEGG, M., et al. Increased Range of Ultrasonic Guided Wave Testing of Overhead Transmission Line Cables using Dispersion Compensation. *Ultrasonics*, 9, 2015, vol. 62. pp. 35-45. ISSN 0041-624X.
25. KAŽYS, R., et al. 3D Analysis of Interaction of Lamb Waves with Defects in Loaded Steel Plates. *Ultrasonics*, 12/22, 2006, vol. 44, Supplement. pp. e1127-e1130. ISSN 0041-624X.
26. MAŽEIKA, L., KAŽYS, R., RAIŠUTIS, R., DEMČENKO, A. and ŠLITERIS, R. Long-Range Ultrasonic Non-Destructive Testing of Fuel Tanks. *DGZfP Proceedings BB 103-CD of ECNDT 2006*, 2006. pp. 1-8.
27. MAŽEIKA, L., KAŽYS, R., RAIŠUTIS, R. and ŠLITERIS, R. *Ultrasonic Guided Wave Tomography for the Inspection of the Fuel Tanks Floor.* Chania, Crete, Greece ed. 4th International Conference on NDT, 11–14 October 2007, 2007.
28. RAIŠUTIS, R., KAŽYS, R., MAŽEIKA, L. and ŠLITERIS, R. Aplication of the Ultrasonic Transmission Tomography for Inspection of the Petroleum Tank Floor. *Ultragarsas (Ultrasound)*, 2007, vol. 62, no. 3. pp. 26-32 ISSN 1392-2114.
29. MAŽEIKA, L., KAŽYS, R., RAIŠUTIS, R. and ŠLITERIS, R. Ultrasonic Guided Wave Tomography for the Inspection of the Fuel Tanks Floor. *International Journal of Materials and Product Technology*, 01/01; 2016/08, 2011, vol. 41, no. 1-4. pp. 128-139 ISSN 0268-1900.

30. CHEN, F. and WILCOX, P.D. The Effect of Load on Guided Wave Propagation. *Ultrasonics*, 12, 2007, vol. 47, no. 1–4. pp. 111-122. ISSN 0041-624X.
31. WILCOX, P., LOWE, M. and CAWLEY, P. The Effect of Dispersion on Long-Range Inspection using Ultrasonic Guided Waves. *NDT & E International*, 1, 2001, vol. 34, no. 1. pp. 1-9. ISSN 0963-8695.
32. XU, K., TA, D., SU, Z. and WANG, W. Transmission Analysis of Ultrasonic Lamb Mode Conversion in a Plate with Partial-Thickness Notch. *Ultrasonics*, 1, 2014, vol. 54, no. 1. pp. 395-401. ISSN 0041-624X.
33. GROYSMAN, A. *Corrosion in Systems for Storage and Transportation of Petroleum Products and Biofuels.* Springer, 2014 ISBN 940077883X.
34. CHEN, T., TIAN, G.Y., SOPHIAN, A. and QUE, P.W. Feature Extraction and Selection for Defect Classification of Pulsed Eddy Current NDT. *NDT & E International*, 9, 2008, vol. 41, no. 6. pp. 467-476. ISSN 0963-8695.
35. LI, J., WU, X., ZHANG, Q. and SUN, P. Pulsed Eddy Current Testing of Ferromagnetic Specimen Based on Variable Pulse Width Excitation. *NDT & E International*, 1, 2015, vol. 69, no. 0. pp. 28-34. ISSN 0963-8695.
36. KIM, D., UDPA, L. and UDPA, S. Remote Field Eddy Current Testing for Detection of Stress Corrosion Cracks in Gas Transmission Pipelines. *Materials Letters*, 6, 2004, vol. 58, no. 15. pp. 2102-2104. ISSN 0167-577X.
37. HOSSEINI, S. and LAKIS, A.A. Application of Time–frequency Analysis for Automatic Hidden Corrosion Detection in a Multilayer Aluminum Structure using Pulsed Eddy Current. *NDT & E International*, 4, 2012, vol. 47, no. 0. pp. 70-79. ISSN 0963-8695.
38. LANG, Z.Q., AGURTO, A., TIAN, G.Y. and SOPHIAN, A. A System Identification Based Approach for Pulsed Eddy Current Non-Destructive Evaluation. *Measurement Science and Technology*, 2007, vol. 18, no. 7. pp. 2083 ISSN 0957-0233.
39. TIAN, G.Y., HE, Y., ADEWALE, I. and SIMM, A. Research on Spectral Response of Pulsed Eddy Current and NDE Applications. *Sensors and Actuators A: Physical*, 1/15, 2013, vol. 189, no. 0. pp. 313-320. ISSN 0924-4247.
40. ALAMIN, M., GUI, Y.T., ANDREWS, A. and JACKSON, P. Principal Component Analysis of Pulsed Eddy Current Response from Corrosion in Mild Steel. *Sensors Journal, IEEE*, 2012, vol. 12, no. 8. pp. 2548-2553 ISSN 1530-437X.
41. ABIDIN, I.Z., MANDACHE, C., TIAN, G.Y. and MOROZOV, M. Pulsed Eddy Current Testing with Variable Duty Cycle on Rivet Joints. *NDT & E International*, 10, 2009, vol. 42, no. 7. pp. 599-605. ISSN 0963-8695.
42. TIAN, G.Y., SOPHIAN, A., TAYLOR, D. and RUDLIN, J. Wavelet-Based PCA Defect Classification and Quantification for Pulsed Eddy Current NDT. *Science, Measurement and Technology, IEE Proceedings* -, 2005, vol. 152, no. 4. pp. 141-148 ISSN 1350-2344. DOI 10.1049/ip-smt:20045011.
43. ATHERTON, D.L. Remote Field Eddy Current Inspection. *IEEE Transactions on Magnetics*, 1995, vol. 31, no. 6. pp. 4142-4147 ISSN 0018-9464.
44. FUKUTOMI, H., TAKAGI, T. and NISHIKAWA, M. Remote Field Eddy Current Technique Applied to Non-Magnetic Steam Generator Tubes. *NDT & E International*, 1, 2001, vol. 34, no. 1. pp. 17-23. ISSN 0963-8695.
45. YANG, B., ZHANG, H., ZHANG, C. and ZHANG, Z. Pulsed Remote Field Eddy Current Technique Applied to Non-Magnetic Flat Conductive Plates. *Nondestructive Testing and Evaluation*, 2013, vol. 28, no. 4. pp. 354-366 ISSN 1058-9759.

46. VASIĆ, D., BILAS, V. and AMBRUS, D. Pulsed Eddy-Current Nondestructive Testing of Ferromagnetic Tubes. *Instrumentation and Measurement, IEEE Transactions On*, 2004, vol. 53, no. 4. pp. 1289-1294 ISSN 0018-9456.
47. MUKHOPADHYAY, S. and SRIVASTAVA, G.P. Characterisation of Metal Loss Defects from Magnetic Flux Leakage Signals with Discrete Wavelet Transform. *NDT & E International*, 1, 2000, vol. 33, no. 1. pp. 57-65. ISSN 0963-8695.
48. ROMERO RAMÍREZ, A., MASON, J.S.D. and PEARSON, N. Experimental Study to Differentiate between Top and Bottom Defects for MFL Tank Floor Inspections. *NDT & E International*, 1, 2009, vol. 42, no. 1. pp. 16-21. ISSN 0963-8695.
49. SHARATCHANDRA SINGH, W., RAO, B.P.C., VAIDYANATHAN, S., JAYAKUMAR, T. and RAJ B. Detection of Leakage Magnetic Flux from Near-Side and Far-Side Defects in Carbon Steel Plates using a Giant Magneto-Resistive Sensor. *Measurement Science and Technology*, 2008, vol. 19, no. 1. pp. 015702 ISSN 0957-0233.
50. SONG, X., HUANG, S. and ZHAO, W. Optimization of the Magnetic Circuit in the MFL Inspection System for Storage-Tank Floors. *Russian Journal of Nondestructive Testing*, 05/01, 2007, vol. 43, no. 5. pp. 326-331 ISSN 1061-8309.
51. WANG, P., GAO, Y., TIAN, G. and WANG, H. Velocity Effect Analysis of Dynamic Magnetization in High Speed Magnetic Flux Leakage Inspection. *NDT & E International*, 6, 2014, vol. 64, no. 0. pp. 7-12. ISSN 0963-8695.
52. WANG, W.K., LI, Y.B., LI, Y.N., and ZHANG, Y. *An Acoustic Emission Event Determination Method for Acoustic Emission Testing of Tank Bottom Based on Cluster Analysis.* , 2013 ISBN 2159-6247.
53. LIYING, S. and YIBO, L. *Large Vertical Storage Tank Bottom Evaluation Via Acoustic Emission Signal Analysis.* , 2011 DOI 10.1109/CCDC.2011.5968734.
54. JOMDECHA, C., PRATEEPASEN, A. and KAEWTRAKULPONG, P. Study on Source Location using an Acoustic Emission System for various Corrosion Types. *NDT & E International*, 12, 2007, vol. 40, no. 8. pp. 584-593. ISSN 0963-8695.
55. HODAEI E., JAVADI M., BROUMANDNIA A. and SADEGHI H. Evaluation of Acoustic Emission Inspection of Oil Tank Floor Via Tank Bottom Plates Thickness Measurement. *Journal of Mechanical Research and Application*, 2012, vol. 4, no. 3. pp. 37-44 ISSN ISSN: 2251-7383.
56. LACKNER G. and TSCHELIESNIG P. Acoustic Emission Testing on Flat-Bottomed Storage Tanks: How to Condence Acquired Data to Reliable Statement regarding Floor Condition. *Journal of Acoustic Emission*, 2002, vol. 20. pp. 179-187 ISSN 0730-0050.
57. ZHANG T. FENG H. and ZENG Z.M. Acoustic Emission Based Tank Bottom Floor Corrosion Detection. *International Journal of Automation Technology*, 2013, vol. 7, no. 2. pp. 205-210 ISSN 1881-7629.
58. VIKTOROV, A.I. *Rayleigh and Lamb Waves: Physical Theory and Applications.* Springer; Softcover reprint of the original 1st ed. 1967 edition (December 7, 2013), 2013 ISBN 1489956832.
59. ROSE, J.L. A Baseline and Vision of Ultrasonic Guided Wave Inspection Potential. *Journal of Pressure Vessel Technology*, 2002, vol. 124, no. 3. pp. 273-282 ISSN 0094-9930.
60. CROXFORD, A.J., WILCOX, P.D., DRINKWATER, B.W. and KONSTANTINIDIS, G. Strategies for Guided-Wave Structural Health Monitoring. *Proceedings of the Royal*

Society of London A: Mathematical, Physical and Engineering Sciences, 11/08, 2007, vol. 463, no. 2087. pp. 2961-2981.

61. F JENOT, F., OUAFTOUH, M., DUQUENNOY M. and OURAK, M. Corrosion Thickness Gauging in Plates using Lamb Wave Group Velocity Measurements. *Measurement Science and Technology*, 2001, vol. 12, no. 8. pp. 1287 ISSN 0957-0233.
62. ALLEYNE, D., CAWLEY, P., THOMPSON, D. and CHIMENTI, D., eds., Springer US, 01/01, 1995 *The Long Range Detection of Corrosion in Pipes using Lamb Waves*, pp. 2073-2080 ISBN 978-1-4613-5819-0.
63. NAGY, P.B., SIMONETTI, F. and INSTANES, G. Corrosion and Erosion Monitoring in Plates and Pipes using Constant Group Velocity Lamb Wave Inspection. *Ultrasonics*, 9, 2014, vol. 54, no. 7. pp. 1832-1841. ISSN 0041-624X.
64. AMJAD, U., YADAV, S.K. and KUNDU, T. Detection and Quantification of Pipe Damage from Change in Time of Flight and Phase. *Ultrasonics*, 9, 2015, vol. 62. pp. 223-236. ISSN 0041-624X.
65. KWUN, H., KIM, S.Y., CHOI, M.S. and WALKER, S.M. Torsional Guided-Wave Attenuation in Coal-Tar-Enamel-Coated, Buried Piping. *NDT & E International*, 12, 2004, vol. 37, no. 8. pp. 663-665. ISSN 0963-8695.
66. ROSE, J.L. Guided Wave Nuances for Ultrasonic Nondestructive Evaluation. *Ultrasonics, Ferroelectrics, and Frequency Control, IEEE Transactions On*, 2000, vol. 47, no. 3. pp. 575-583 ISSN 0885-3010.
67. MOUSTAFA, A. and SALAMONE, S. Fractal Dimension–based Lamb Wave Tomography Algorithm for Damage Detection in Plate-Like Structures. *Journal of Intelligent Material Systems and Structures*, July 01, 2012, vol. 23, no. 11. pp. 1269-1276.
68. WILLEY, C.L., SIMONETTI, F., NAGY, P.B. and INSTANES, G. Guided Wave Tomography of Pipes with High-Order Helical Modes. *NDT & E International*, 7, 2014, vol. 65. pp. 8-21. ISSN 0963-8695.
69. DILIGENT, O., et al. The Low-Frequency Reflection and Scattering of the S0 Lamb Mode from a Circular through-Thickness Hole in a Plate: Finite Element, Analytical and Experimental Studies. *The Journal of the Acoustical Society of America*, 2002, vol. 112, no. 6. pp. 2589-2601.
70. DEMMA, A., CAWLEY, P. and LOWE, M. Scattering of the Fundamental Shear Horizontal Mode from Steps and Notches in Plates. *The Journal of the Acoustical Society of America*, 2003, vol. 113, no. 4. pp. 1880-1891.
71. DILIGENT, O. and LOWE, M.J.S. Reflection of the S0 Lamb Mode from a Flat Bottom Circular Hole. *The Journal of the Acoustical Society of America*, 2005, vol. 118, no. 5. pp. 2869-2879.
72. MA, J. and CAWLEY, P. Low-Frequency Pulse Echo Reflection of the Fundamental Shear Horizontal Mode from Part-Thickness Elliptical Defects in Plates. *The Journal of the Acoustical Society of America*, 2010, vol. 127, no. 6. pp. 3485-3493.
73. CARANDENTE, R., MA, J. and CAWLEY, P. The Scattering of the Fundamental Torsional Mode from Axi-Symmetric Defects with Varying Depth Profile in Pipes. *The Journal of the Acoustical Society of America*, 2010, vol. 127, no. 6. pp. 3440-3448.
74. LØVSTAD, A. and CAWLEY, P. The Reflection of the Fundamental Torsional Guided Wave from Multiple Circular Holes in Pipes. *NDT & E International*, 11, 2011, vol. 44, no. 7. pp. 553-562. ISSN 0963-8695.

75. LØVSTAD, A. and CAWLEY, P. The Reflection of the Fundamental Torsional Mode from Pit Clusters in Pipes. *NDT & E International*, 3, 2012, vol. 46. pp. 83-93. ISSN 0963-8695.
76. COBB, A.C., KWUN, H., CASERES, L. and JANEGA, G. Torsional Guided Wave Attenuation in Piping from Coating, Temperature, and Large-Area Corrosion. *NDT & E International*, 4, 2012, vol. 47. pp. 163-170. ISSN 0963-8695.
77. CARANDENTE, R., LOVSTAD, A. and CAWLEY, P. The Influence of Sharp Edges in Corrosion Profiles on the Reflection of Guided Waves. *NDT & E International*, 11, 2012, vol. 52. pp. 57-68. ISSN 0963-8695.
78. VELICHKO, A. and WILCOX, P.D. Scattering of Guided Waves from Complex Defects in Plates in Pipes. *AIP Conference Proceedings*, 2013, vol. 1511, no. 1. pp. 129-136.
79. LEONARD, K.R. and HINDERS, M.K. Lamb Wave Tomography of Pipe-Like Structures. *Ultrasonics*, 6, 2005, vol. 43, no. 7. pp. 574-583. ISSN 0041-624X.
80. KODURU, J.P. and ROSE, J.L. Mode Controlled Guided Wave Tomography using Annular Array Transducers for SHM of Water Loaded Plate Like Structures. *Smart Materials and Structures*, 2013, vol. 22, no. 12. pp. 125021 ISSN 0964-1726.
81. HUTHWAITE, P., RIBICHINI, R., CAWLEY, P. and LOWE, M.J.S. Mode Selection for Corrosion Detection in Pipes and Vessels Via Guided Wave Tomography. *Ultrasonics, Ferroelectrics, and Frequency Control, IEEE Transactions On*, 2013, vol. 60, no. 6. pp. 1165-1177 ISSN 0885-3010.
82. SU, Z. and YE, L.Springer London, 01/01, 2009 *Fundamentals and Analysis of Lamb Waves*, pp. 15-58 ISBN 978-1-84882-783-7.
83. SU, Z., YE, L. and LU, Y. Guided Lamb Waves for Identification of Damage in Composite Structures: A Review. *Journal of Sound and Vibration*, 8/22, 2006, vol. 295, no. 3–5. pp. 753-780. ISSN 0022-460X.
84. STASZEWSKI, W.J., LEE, B.C. and TRAYNOR, R. Fatigue Crack Detection in Metallic Structures with Lamb Waves and 3D Laser Vibrometry. *Measurement Science and Technology*, 2007, vol. 18, no. 3. pp. 727 ISSN 0957-0233.
85. ROSE, J.L. *Ultrasonic Waves in Solid Media.* Cambridge University Press, 2004 ISBN 978-0521548892.
86. HAYASHI, T., SONG, W. and ROSE, J.L. Guided Wave Dispersion Curves for a Bar with an Arbitrary Cross-Section, a Rod and Rail Example. *Ultrasonics*, 5, 2003, vol. 41, no. 3. pp. 175-183. ISSN 0041-624X.
87. HAYASHI, T., KAWASHIMA, K. and ROSE, J.L. Calculation for Guided Waves in Pipes and Rails. *Key Engineering Materials*, 2004, vol. 270-273. pp. 410-415 ISSN 1662-9795.
88. SICARD, R., GOYETTE, J. and ZELLOUF, D. A Numerical Dispersion Compensation Technique for Time Recompression of Lamb Wave Signals. *Ultrasonics*, 5, 2002, vol. 40, no. 1–8. pp. 727-732. ISSN 0041-624X.
89. ALLEUNE, D.N. and CAWLEY, P. The Interaction of Lamb Waves with Defects. *IEEE Transactions on Ultrasonics, Ferroelectrics, and Frequency Control*, 1992, vol. 39, no. 3. pp. 381-397 ISSN 0885-3010.
90. ROSE, J.L. Dispersion Curves in Guided Wave Testing. *Materials Evaluation*, 2003, vol. 61. pp. 20-22.

91. WILCOX, P.D. A Rapid Signal Processing Technique to Remove the Effect of Dispersion from Guided Wave Signals. *Ultrasonics, Ferroelectrics, and Frequency Control, IEEE Transactions On*, 2003, vol. 50, no. 4. pp. 419-427 ISSN 0885-3010.
92. SONG, W., ROSE, J.L., GALAN, J.M. and ABASCAL, R. Ultrasonic Guided Wave Scattering in a Plate Overlap. *Ultrasonics, Ferroelectrics, and Frequency Control, IEEE Transactions On*, 2005, vol. 52, no. 5. pp. 892-903 ISSN 0885-3010.
93. REUSSER, R.S., CHIMENTI, D.E., ROBERTS, R.A. and HOLLAND, S.D. Guided Plate Wave Scattering at Vertical Stiffeners and its Effect on Source Location. *Ultrasonics*, 8, 2012, vol. 52, no. 6. pp. 687-693. ISSN 0041-624X.
94. DENG, Q. and YANG, Z. Scattering of S0 Lamb Mode in Plate with Multiple Damage. *Applied Mathematical Modelling*, 1, 2011, vol. 35, no. 1. pp. 550-562. ISSN 0307-904X.
95. LU, Y., YE, L., SU, Z. and YANG, C. Quantitative Assessment of through-Thickness Crack Size Based on Lamb Wave Scattering in Aluminium Plates. *NDT & E International*, 1, 2008, vol. 41, no. 1. pp. 59-68. ISSN 0963-8695.
96. BARSHINGER, J.N. and ROSE, J.L. Guided Wave Propagation in an Elastic Hollow Cylinder Coated with a Viscoelastic Material. *Ultrasonics, Ferroelectrics, and Frequency Control, IEEE Transactions On*, 2004, vol. 51, no. 11. pp. 1547-1556 ISSN 0885-3010.
97. GRESIL, M. and GIURGIUTIU, V. Guided Wave Propagation in Carbon Composite Laminate using Piezoelectric Wafer Active Sensors. *Proc. SPIE 8695, Health Monitoring of Structural and Biological Systems 2013, 869525 (17 April 2013)*, 2013.
98. GRESIL, M. and GIURGIUTIU, V. Prediction of Attenuated Guided Waves Propagation in Carbon Fiber Composites using Rayleigh Damping Model. *Journal of Intelligent Material Systems and Structures*, September 08, 2014.
99. WILKIE-CHANCELLIER, N., DUFLO, H., TINEL, A. and DUCLOS, J. Experimental Study and Signal Analysis in the Lamb Wave Conversion at a Bevelled Edge. *Ultrasonics*, 4, 2004, vol. 42, no. 1–9. pp. 377-381. ISSN 0041-624X.
100. RAMADAS, C., et al. Transmission and Reflection of the Fundamental Lamb Modes in a Metallic Plate with a Semi-Infinite Horizontal Crack. *Ultrasonics*, 3, 2013, vol. 53, no. 3. pp. 773-781. ISSN 0041-624X.
101. PAVLAKOVIC, B., LOWE, M., ALLEYNE, D. and CAWLEY, P. Review of Progress in Quantitative Nondestructive Evaluation: Volume 16A D.O. THOMPSON and D.E. CHIMENTI eds., Boston, MA: Springer US, 1997 *Disperse: A General Purpose Program for Creating Dispersion Curves*, pp. 185-192 ISBN 978-1-4615-5947-4.
102. KAZYS, R., MAZEIKA, L., SLITERIS, R. and RAISUTIS, R. Measurement of Viscosity of Highly Viscous Non-Newtonian Fluids by Means of Ultrasonic Guided Waves. *Ultrasonics*, 4, 2014, vol. 54, no. 4. pp. 1104-1112. ISSN 0041-624X.
103. NAGATA, Y., HUANG, J., ACHENBACH, J.D. and KRISHNASWAMY, S. D. THOMPSON and D. CHIMENTI eds., Springer US, 01/01, 1995 *Lamb Wave Tomography using Laser-Based Ultrasonics*, pp. 561-568 ISBN 978-1-4613-5819-0.
104. HINDERS, M., MALYARENKO, E. and MCKEON, J. Contact Scanning Lamb Wave Tomography. *The Journal of the Acoustical Society of America*, 1998, vol. 104, no. 3. pp. 1790-1791.
105. MCKEON, J.C.P. and HINDERS, M.K. Parallel Projection and Crosshole Lamb Wave Contact Scanning Tomography. *The Journal of the Acoustical Society of America*, 1999, vol. 106, no. 5. pp. 2568-2577.

106. LEONARD, K.R. and HINDERS, M.K. Guided Wave Helical Ultrasonic Tomography of Pipes. *The Journal of the Acoustical Society of America*, 2003, vol. 114, no. 2. pp. 767-774.

107. HOU J., LEONARD, K.R. and HINDERS M.K. Automatic Multi-Mode Lamb Wave Arrival Time Extraction for Improved Tomographic Reconstruction. *Inverse Problems*, 2004, vol. 20, no. 6. pp. 1873 ISSN 0266-5611.

108. PRASAD, S.M., BALASUBRAMANIAM, K. and KRISHNAMURTHY, C.V. Structural Health Monitoring of Composite Structures using Lamb Wave Tomography. *Smart Materials and Structures*, 2004, vol. 13, no. 5. pp. N73 ISSN 0964-1726.

109. HINDERS, M.K. and LEONARD, K.R. Lamb Wave Tomography of Pipes and Tanks using Frequency Compounding. *AIP Conference Proceedings*, 2005, vol. 760, no. 1. pp. 867-874.

110. HAY, T.R., R L ROYER, R.L., GAO, H., ZHAO, X. and L.ROSE, J.L. A Comparison of Embedded Sensor Lamb Wave Ultrasonic Tomography Approaches for Material Loss Detection. *Smart Materials and Structures*, 2006, vol. 15, no. 4. pp. 946 ISSN 0964-1726.

111. ALBIRUNI, F., CHO, Y., LEE, J. and AHN, B. Non-Contact Guided Waves Tomographic Imaging of Plate-Like Structures using a Probabilistic Algorithm. *Materials Transactions*, 2012, vol. 53, no. 2. pp. 330-336 DOI 10.2320/matertrans.I-M2011853.

112. HU, B., et al. Tomographic Reconstruction of Damage Images in Hollow Cylinders using Lamb Waves. *Ultrasonics*, 9, 2014, vol. 54, no. 7. pp. 2015-2023. ISSN 0041-624X.

113. LASAYGUES, P., LEFEBVRE, J.P. and BOUVAT-MERLIN, M. H. LEE ed., Springer US, 01/01, 2002 *High-Resolution Process in Ultrasonic Reflection Tomography*, pp. 35-41 ISBN 978-0-306-46518-5. DOI 10.1007/0-306-47108-6_5.

114. STEINER, G. AND, D.W. A Bayesian Filtering Approach for Inclusion Detection with Ultrasound Reflection Tomography. *Journal of Physics: Conference Series*, 2008, vol. 124, no. 1. pp. 012049 ISSN 1742-6596.

115. BELANGER, P. and CAWLEY, P. Feasibility of Low Frequency Straight-Ray Guided Wave Tomography. *NDT & E International*, 3, 2009, vol. 42, no. 2. pp. 113-119. ISSN 0963-8695.

116. BELANGER, P., CAWLEY, P. and SIMONETTI, F. Guided Wave Diffraction Tomography within the Born Approximation. *Ultrasonics, Ferroelectrics, and Frequency Control, IEEE Transactions On*, 2010, vol. 57, no. 6. pp. 1405-1418 ISSN 0885-3010.

117. CHAN, E., ROSE, L.R.F. and WANG, C.H. An Extended Diffraction Tomography Method for Quantifying Structural Damage using Numerical Green's Functions. *Ultrasonics*, 5, 2015, vol. 59. pp. 1-13. ISSN 0041-624X.

118. HUTHWAITE, P. and SIMONETTI, F. High-Resolution Guided Wave Tomography. *Wave Motion*, 7, 2013, vol. 50, no. 5. pp. 979-993. ISSN 0165-2125.

119. SPETZLER, J., SIVAJI, C., NISHIZAWA, O. and FUKUSHIMA, Y. A Test of Ray Theory and Scattering Theory Based on a Laboratory Experiment using Ultrasonic Waves and Numerical Simulation by Finite-Difference Method. *Geophysical Journal International*, February 01, 2002, vol. 148, no. 2. pp. 165-178.

120. HUTHWAITE, P. Evaluation of Inversion Approaches for Guided Wave Thickness Mapping. *Proceedings of the Royal Society of London A: Mathematical, Physical and Engineering Sciences*, The Royal Society, 2014, vol. 470, no. 2166.

121. SIMONETTI, F. and HUANG, L. From Beamforming to Diffraction Tomography. *Journal of Applied Physics*, 2008, vol. 103, no. 10. pp. 103110.

122. MALYARENKO, E.V. and HINDERS, M.K. Ultrasonic Lamb Wave Diffraction Tomography. *Ultrasonics*, 6, 2001, vol. 39, no. 4. pp. 269-281. ISSN 0041-624X.

123. LASAYGUES, P., GUILLERMIN, R. and LEFEBVRE, J. Distorted Born Diffraction Tomography Applied to Inverting Ultrasonic Field Scattered by Noncircular Infinite Elastic Tube. *Ultrasonic Imaging*, October 01, 2006, vol. 28, no. 4. pp. 211-229.

124. PIPERAKIS, G.S., SKARSOULIS, E.K. and MAKRAKIS, G.N. Rytov Approximation of Tomographic Receptions in Weakly Range-Dependent Ocean Environments. *The Journal of the Acoustical Society of America*, 2006, vol. 120, no. 1. pp. 120-134.

125. SIMONETTI, F., HUANG, L. and DURIC, N. On the Spatial Sampling of Wave Fields with Circular Ring Apertures. *Journal of Applied Physics*, 2007, vol. 101, no. 8. pp. 083103..

126. MALYARENKO, E.V. and HINDERS, M.K. Fan Beam and Double Crosshole Lamb Wave Tomography for Mapping Flaws in Aging Aircraft Structures. *The Journal of the Acoustical Society of America*, 2000, vol. 108, no. 4. pp. 1631-1639.

127. XIANG, Z., ROSE, J.L. and HUIDONG, G. Determination of Density Distribution in Powder Compacts using Ultrasonic Tomography. *Ultrasonics, Ferroelectrics, and Frequency Control, IEEE Transactions On*, 2006, vol. 53, no. 2. pp. 360-369 ISSN 0885-3010.

128. DENISIUK, A. R. BURDUK, et al ed., Springer International Publishing, 01/01, 2013 *Interpolation Procedure in Filtered Backprojection Algorithm for the Limited-Angle Tomography*, pp. 551-558 ISBN 978-3-319-00968-1.

129. PETERLÍK, I., JIŘÍK, R. and RUITER, N. *Algebraic Reconstruction Technique for Ultrasound Transmission Tomography*. Ioannina (Greece) ed. Ioannina (Greece): , 2006.

130. LEONARD, K.R., MALYARENKO, E.V. and HINDERS, M.K. Ultrasonic Lamb Wave Tomography. *Inverse Problems*, 2002, vol. 18, no. 6. pp. 1795 ISSN 0266-5611.

131. KEULEN C. J., YILDIZ M., SULEMAN A. Damage Detection of Composite Plates by Lamb Wave Tomography with a Sparse Hexagonal Network using Damage Progression Trends. *Shock and Vibration*, 2014, vol. 2014. pp. 8 pages.

132. SHEEN, B. and CHO, Y. A Study on Quantitative Lamb Wave Tomogram Via Modified RAPID Algorithm with Shape Factor Optimization. *International Journal of Precision Engineering and Manufacturing*, 05/01, 2012, vol. 13, no. 5. pp. 671-677 ISSN 2234-7593.

133. LEE, J., SHEEN, B. and CHO, Y. Quantitative Tomographic Visualization for Irregular Shape Defects by Guided Wave Long Range Inspection. *International Journal of Precision Engineering and Manufacturing*, 08/01, 2015, vol. 16, no. 9. pp. 1949-1954 ISSN 2234-7593.

134. LI, W. and CHO, Y. Quantification and Imaging of Corrosion Wall Thinning using Shear Horizontal Guided Waves Generated by Magnetostrictive Sensors. *Sensors and Actuators A: Physical*, 8/1, 2015, vol. 232. pp. 251-258. ISSN 0924-4247.

135. LI, W. and CHO, Y. Combination of Nonlinear Ultrasonics and Guided Wave Tomography for Imaging the Micro-Defects. *Ultrasonics*, 2, 2016, vol. 65. pp. 87-95. ISSN 0041-624X.

136. British Standards Institution. *Specification for the Design and Manufacture of Site Built, Vertical, Cylindrical, Flat-Bottomed, Above Ground, Welded, Steel Tanks for the Storage of Liquids at Ambient Temperature and Above.* , BS EN 14015:2004.

137. MOSER, F., JACOBS, L., QU, J., THOMPSON, D.and CHIMENTI, D., eds., Springer US, 01/01, 1998 *Application of Finite Element Methods to Study Transient Wave Propagation in Elastic Wave Guides*, pp. 161-167 ISBN 978-1-4613-7436-7.

138. MOSER, F., JACOBS, L.J. and QU, J. Modeling Elastic Wave Propagation in Waveguides with the Finite Element Method. *NDT & E International*, 6, 1999, vol. 32, no. 4. pp. 225-234. ISSN 0963-8695.

139. LIU, G.R. and QUEK JERRY, S.S. A Non-Reflecting Boundary for Analyzing Wave Propagation using the Finite Element Method. *Finite Elements in Analysis and Design*, 3, 2003, vol. 39, no. 5–6. pp. 403-417. ISSN 0168-874X.

140. CERNIGLIA, D., PANTANO, A. and MONTINARO, N. 3D Simulations and Experiments of Guided Wave Propagation in Adhesively Bonded Multi-Layered Structures. *NDT & E International*, 9, 2010, vol. 43, no. 6. pp. 527-535. ISSN 0963-8695.

141. SOROHAN, Ş, CONSTANTIN, N., GĂVAN, M. and ANGHEL, V. Extraction of Dispersion Curves for Waves Propagating in Free Complex Waveguides by Standard Finite Element Codes. *Ultrasonics*, 5, 2011, vol. 51, no. 4. pp. 503-515. ISSN 0041-624X.

142. NOH, G. and BATHE, K. An Explicit Time Integration Scheme for the Analysis of Wave Propagations. *Computers & Structures*, 12, 2013, vol. 129, no. 0. pp. 178-193. ISSN 0045-7949.

143. ASMUS, A. and LAMMERING, R. Actual Time Integration Methods for Elastic Wave Propagation Analysis. *Pamm*, 2014, vol. 14, no. 1. pp. 857-858. ISSN 1617-7061.

144. DUCZEK, S., JOULAIAN, M., DÜSTER, A. and GABBERT, U. Numerical Analysis of Lamb Waves using the Finite and Spectral Cell Methods. *International Journal for Numerical Methods in Engineering*, 2014, vol. 99, no. 1. pp. 26-53. ISSN 1097-0207.

145. MIRBAGHERI, Y., NAHVI, H., PARVIZIAN, J. and DÜSTER, A. Reducing Spurious Oscillations in Discontinuous Wave Propagation Simulation using High-Order Finite Elements. *Computers & Mathematics with Applications*. ISSN 0898-1221.

146. TERRIEN, N., et al. A Combined Finite Element and Modal Decomposition Method to Study the Interaction of Lamb Modes with Micro-Defects. *Ultrasonics*, 3, 2007, vol. 46, no. 1. pp. 74-88. ISSN 0041-624X.

147. MAL, A., LIH, S. and GUO, D. D. THOMPSON and D. CHIMENTI eds., Springer US, 01/01, 1995 *Ultrasonic Characterization of Defects in Lap Joints*, pp. 2059-2064 ISBN 978-1-4613-5819-0.

148. CHANG, Z., GUO, D. and MAL, A. D. THOMPSON and D. CHIMENTI eds., Springer US, 01/01, 1996 *Lamb Wave Propagation Across a Lap Joint*, pp. 185-192 ISBN 978-1-4613-8027-6.

149. DALTON, R.P., CAWLEY, P. and LOWE, M.J.S. The Potential of Guided Waves for Monitoring Large Areas of Metallic Aircraft Fuselage Structure. *Journal of Nondestructive Evaluation*, 03/01, 2001, vol. 20, no. 1. pp. 29-46 ISSN 0195-9298.

150. LANZA DI SCALEA, F., RIZZO, P. and MARZANI, A. Propagation of Ultrasonic Guided Waves in Lap-Shear Adhesive Joints: Case of Incident A0 Lamb Wave. *The Journal of the Acoustical Society of America*, 2004, vol. 115, no. 1. pp. 146-156.
151. CHOI, M.S. and KIM, S.J. Reflection and Transmission of Normal Incidence SH0 Waves at a Lap Joint of Two Plates of the Same Material and Thickness. *J. Korean Phys.Soc.*, 2006, vol. 49, no. 5. pp. 1955-1960.
152. CASTAINGS, M. SH Ultrasonic Guided Waves for the Evaluation of Interfacial Adhesion. *Ultrasonics*, 9, 2014, vol. 54, no. 7. pp. 1760-1775. ISSN 0041-624X.
153. SIRYABE, E., RENIER, M., MEZIANE, A. and CASTAINGS, M. The Transmission of Lamb Waves Across Adhesively Bonded Lap Joints to Evaluate Interfacial Adhesive Properties. *Physics Procedia*, 2015, vol. 70. pp. 541-544. ISSN 1875-3892.
154. SANTOS, M.J. and FAIA, P. Propagation of Ultrasonic Lamb Waves in Aluminium Adhesively Bonded LAP Joints and in Single Plates. *Research in Nondestructive Evaluation*, 07/14; 2015/05, 2009, vol. 20, no. 3. pp. 178-191 ISSN 0934-9847.
155. ARISTÉGUI, C., LOWE, M.J.S. and CAWLEY, P. Guided Waves in Fluid-Filled Pipes Surrounded by Different Fluids. *Ultrasonics*, 8, 2001, vol. 39, no. 5. pp. 367-375. ISSN 0041-624X.
156. KAŽYS, R., RAIŠUTIS, R., and VLADIŠAUSKAS, A. Estimation of the Acoustic Properties of Moist Sand. *Ultragarsas (Ultrasound)*, 2004, vol. 2, no. 51. pp. 17-20 ISSN 1392-2114.
157. *Bulk Modulus and Fluid Elasticity.* Available from:http://www.engineeringtoolbox.com/bulk-modulus-elasticity-d_585.html.
158. *Bulk Modulus of Elasticity of Liquids.* Available from:https://neutrium.net/properties/bulk-modulus-of-elasticity-of-liquids/.
159. HULBERT, G.M. and CHUNG, J. Explicit Time Integration Algorithms for Structural Dynamics with Optimal Numerical Dissipation. *Computer Methods in Applied Mechanics and Engineering*, 10/15, 1996, vol. 137, no. 2. pp. 175-188. ISSN 0045-7825.
160. BARTOLI, I., LANZA DI SCALEA, F., FATEH, M. and VIOLA, E. Modeling Guided Wave Propagation with Application to the Long-Range Defect Detection in Railroad Tracks. *NDT & E International*, 7, 2005, vol. 38, no. 5. pp. 325-334. ISSN 0963-8695.
161. JEFFREY, L., CIPOLLA, R.G., and RAM, D. *Efficient Finite-Element Modeling with Equivalent-Fluid Porous Materials.* Dearborn, Michigan, USA, ed. ASME 2008 Noise Control and Acoustics Division Conference: , July 28–30, 2008 ISBN 0-7918-4839-6.
162. VLADIŠAUSKAS, A., ŠLITERIS, R., RAIŠUTIS, R., and SENIŪNAS, G. Contact Ultrasonic Trasnducers for Mechanical Scanning Systems. *Ultragarsas (Ultrasound)*, 2010, vol. 65, no. 2. pp. 30-35 ISSN 1392-2114.
163. VLADIŠAUSKAS, A., RAIŠUTIS, R., ŠLITERIS, R., SENIŪNAS, G., and JANKAUSKAS A. Investigation of the Characteristics of the Low Frequency Broadband Contact Transducers. *Ultragarsas (Ultrasound)*, 2010, vol. 65, no. 3. pp. 41-44 ISSN 1392-2114.
164. VLADIŠAUSKAS, A., MAŽEIKA, L., ŠLITERIS, R., RAIŠUTIS, R., and JANKAUSKAS, A. Pulse and Frequency Responses of Broadband Low Frequency Ultrasonic Transducers. *Ultragarsas (Ultrasound)*, 2011, vol. 66, no. 1. pp. 32-39 ISSN 1392-2114.

165. ALLEYNE, D.N. and CAWLEY, P. *A 2-Dimensional Fourier Transform Method for the Quantitative Measurement of Lamb Modes.* , 1990 DOI 10.1109/ULTSYM.1990.171541.

166. DUFLO, H., MORVAN, B. and IZBICKI, J.-. Interaction of Lamb Waves on Bonded Composite Plates with Defects. *Composite Structures*, 7, 2007, vol. 79, no. 2. pp. 229-233. ISSN 0263-8223.

167. RUZZENE, M. Frequency-Wavenumber Domain Filtering for Improved Damage Visualization. *Smart Materials and Structures*, 2007, vol. 16, no. 6. pp. 2116 ISSN 0964-1726.

168. MICHAELS, T.E., MICHAELS, J.E. and RUZZENE, M. Frequency–wavenumber Domain Analysis of Guided Wavefields. *Ultrasonics*, 5, 2011, vol. 51, no. 4. pp. 452-466. ISSN 0041-624X.

169. TIAN, Z. and YU, L. Lamb Wave Frequency–wavenumber Analysis and Decomposition. *Journal of Intelligent Material Systems and Structures*, February 17, 2014.

170. YU, L. and TIAN, Z. Case Study of Guided Wave Propagation in a One-Side Water-Immersed Steel Plate. *Case Studies in Nondestructive Testing and Evaluation*, 4, 2015, vol. 3. pp. 1-8. ISSN 2214-6571.

171. MALYARENKO, E.V., HEYMAN, J.S., CHEN-MAYER, H.H. and TOSH, R.E. Time-Resolved Radiation Beam Profiles in Water obtained by Ultrasonic Tomography. *Metrologia*, 2010, vol. 47, no. 3. pp. 208 ISSN 0026-1394.

172. WEI, Y., et al. Ultrasonic Al2O3 Ceramic Thermometry in High-Temperature Oxidation Environment. *Sensors*, 11 November 2016, vol. 16, no. 11. pp. 1905.

173. DAW, J., et al. *NEET in-Pile Ultrasonic Sensor Enablement-Final Report; Sponsor Org.: DOE - NE.* United States: -09-01, 2014 DOI 10.2172/1166037.

174. RAGAUSKAS A., et al. Ultrasonic Time-of-Flight Method for Non-Invasive Physiological Monitoring of the Human Brain. *Ultragarsas (Ultrasound)*, 2008, vol. 63, no. 2. pp. 49-52 ISSN 1392-2114.

175. MAŽEIKA, L., and DRAUDVILIENĖ, L. Analysis of the Zero-Crossing Technique in Relation to Measurements of Phase Velocities of the Lamb Waves. *Ultragarsas (Ultrasound)*, 2010, vol. 65, no. 2. pp. 7-12 ISSN 1392-2114.

176. ADAMS, T.M. G104 - A2LA Guide for Estimation of Measurement Uncertainty in Testing, 2002. pp. 1-42.

177. BIRCH, K. Estimating Uncertainties in Testing. an Intermediate Guide to Estimating and Reporting Uncertainty of Measurement in Testing. *British Measurement and Testing Association*, 2003. pp. 1-44.

178. MAICHEN W,. *Digital Timing Measurements: From Scopes and Probes to Timing and Jitter.* Springer, 2006 ISBN 978-0387314181.

LIST OF SCIENTIFIC PUBLICATIONS ON THE TOPIC OF DISSERTATION

ARTICLES
In the publications of the main list of the Institute of Scientific Information (ISI)

1. **Jankauskas**, **Audrius**; Mažeika, Liudas. Ultrasonic guided wave propagation through welded lap joints // Metals. Basel: MDPI AG. ISSN 2075-4701. 2016, vol. 6, iss. 12, p. [1-15]. [Science Citation Index Expanded (Web of Science)]. [IF: 1,574; AIF: 2,950; IF/AIF: 0,534; Q1; 2015 Journal Citation Reports® Science Edition (Thomson Reuters, 2016)]. [Contribution: 0,500]
2. **Jankauskas, Audrius**; Mažeika, Liudas; Draudvilienė, Lina; Genutis, Gediminas. Investigation of the lamb waves generation in isotropic plates using ultrasonic broadband transducers // Elektronika ir elektrotechnika = Electronics and Electrical Engineering. Kaunas: KTU. ISSN 1392-1215. 2013, Vol. 19, no. 8, p. 33-36. [Science Citation Index Expanded (Web of Science); INSPEC; Computers & Applied Sciences Complete; Central & Eastern European Academic Source]. [IF: 0,445; AIF: 1,812; IF/AIF: 0,246; Q4; 2013 Journal Citation Reports® Science Edition (Thomson Reuters, 2016)]. [Contribution: 0,250]

REPORTS IN SCIENTIFIC CONFERENCES

1. **A. Jankauskas**, L. Mažeika, R. Kažys. Application of the ultrasonic guided wave for the inspection of the fuel tank // 19th World Conference on Non-Destructive Testing: 2016 06 13-17, Munich, Germany.
2. **A. Jankauskas**, L. Mažeika. Investigation of the guided waves propagation through the lap joint // 11th European Conference on Non-Destructive Testing: 2014 10 06-10, Prague, Czech Republic.
3. **A. Jankauskas**, L. Mažeika. Investigation of the guided waves propagation through the "T" type and lap joints of the welded storage tank plates // International workshop: Nonlinear and Multiscale Dynamics of Smart Materials in Energy Harvesting: 2014 02 17-18, Lublin, Poland.
4. **A. Jankauskas**, L. Mažeika, L. Draudvilienė. Investigation of the Lamb waves generation in isotropic plates using broadband ultrasonic transducers // 17th international conference Electronics 2013: 2013 06 17-19, Palanga, Lithuania.

SL344. 2017-06-28, 17,75 leidyb. apsk. l. Tiražas 12 egz. Užsakymas 218.
Išleido Kauno technologijos universitetas, K. Donelaičio g. 73, 44249 Kaunas
Spausdino leidyklos „Technologija“ spaustuvė, Studentų g. 54, 51424 Kaunas